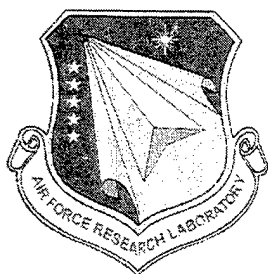# DUAL SURFACE ELECTRIC FIELD INTEGRAL EQUATION

ROBERT A. SHORE/AFRL/SNHA
80 Scott Drive
Hanscom AFB MA 01731

ARTHUR D. YAGHJIAN
A.J. Devaney

IN-HOUSE REPORT: October 1999 – January 2001

AIR FORCE RESEARCH LABORATORY
Sensors Directorate
80 Scott Drive
AIR FORCE MATERIEL COMMAND
Hanscom AFB MA 01731-2909

20020225 060

TITLE OF REPORT: DUAL SURFACE ELECTRIC FIELD INTEGRAL
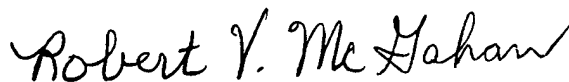EQUATION

PUBLICATION REVIEW

This report has been reviewed and is approved for publication.

APPROVED:

ROBERT A. SHORE
Antenna Technology Branch
Electromagnetics Technology Division

FOR THE DIRECTOR

ROBERT V. McGAHAN
Division Technical Advisor
Electromagnetics Technology Division

REPORT DOCUMENTATION PAGE

1. REPORT DATE (DD-MM-YYYY)	2. REPORT TYPE	3. DATES COVERED (From - To)
	In-House	October 1999 - January 2001

4. TITLE AND SUBTITLE
DUAL SURFACE ELECTRIC FIELD INTEGRAL EQUATION

5a. CONTRACT NUMBER

5b. GRANT NUMBER

5c. PROGRAM ELEMENT NUMBER

6. AUTHOR(S)

Robert A. Shore and Arthur D. Yaghjian

5d. PROJECT NUMBER
2304

5e. TASK NUMBER
IN

5f. WORK UNIT NUMBER
00

7. PERFORMING ORGANIZATION NAME(S) AND ADDRESS(ES)

AFRL/SNHA
80 Scott Drive
Hanscom AFB MA 01731-2909

8. PERFORMING ORGANIZATION REPORT NUMBER

9. SPONSORING/MONITORING AGENCY NAME(S) AND ADDRESS(ES)

10. SPONSOR/MONITOR'S ACRONYM(S)

11. SPONSOR/MONITOR'S REPORT NUMBER(S)

12. DISTRIBUTION/AVAILABILITY STATEMENT
"A"

13. SUPPLEMENTARY NOTES

14. ABSTRACT
A detailed analysis and solution of the problem of scattering by a perfectly electrically conducting body of revolution using the dual surface electric field integral equation (DSEFIE) is given for the first time. Scattering calculations using the DSEFIE are free from the spurious resonances that can seriously degrade the accuracy of calculations made using the conventional electric field integral equation or magnetic field integral equation. The Galerkin form of the method of moments is used to solve the DSEFIE, and the solution is given by detailed expressions suitable for computer programming. Calculations performed with a computer program of the DSEFIE solution demonstrate the removal of spurious resonances from radar cross section patterns of spheres, spheroids, and finite cylinders obtained with the conventional electric field integral equation. Cone-sphere scattering calculations show the importance of careful placement of the dual surface when the DSEFIE is applied to scatterers with narrow tips.

15. SUBJECT TERMS

Electromagnetic Scattering, Electric Field Integral Equation, Body of Revolution, Dual Surface, Perfect Conductor

16. SECURITY CLASSIFICATION OF:			17. LIMITATION OF ABSTRACT	18. NUMBER OF PAGES	19a. NAME OF RESPONSIBLE PERSON
a. REPORT	b. ABSTRACT	c. THIS PAGE			Robert A. Shore
U	U	U	UL	95	19b. TELEPHONE NUMBER (Include area code) (781) 377-2058

ACKNOWLEDGEMENT

Contents

List of Figures

1 INTRODUCTION

Computational electromagnetics continues to rely heavily on surface integral equations for the efficient numerical solution to scattering from perfectly electrically conducting (PEC) bodies [1], [2], [3]. Both the magnetic-field integral equation (MFIE), which was derived by Murray [4] in 1931, and the electric-field integral equation (EFIE), which was derived along with the MFIE in the definitive 1949 paper by Maue [5], are applied only to the surface current of the scatterer and thus require a number of unknowns proportional to the surface area in square wavelengths of a three-dimensional (3-D) scatterer.[1] The MFIE is an absolutely convergent integral equation of the second kind whose associated discrete matrix has a bounded condition number as the number of discretizations (grid points) on the surface of the scatterer approaches an infinite value. The EFIE is a conditionally convergent integro-differential equation of the first kind whose associated discrete matrix has an unbounded condition number as the number of discretizations on the surface of the scatterer approaches an infinite value [5], [6], [7], [8]. Therefore, the determination of surface current (and subsequently the scattered fields) for a scatterer using the EFIE generally requires a more sophisticated numerical scheme with more unknowns per square wavelength than the MFIE. However, the matrix solution to the MFIE degenerates to an underdetermined set of equations for the surface current on an open scatterer (infinitesimally thin conductor) [9, pp. 168–172] and approaches degeneracy if parts of the conducting surface become much closer to each other than a wavelength as in the case of a thin plate, thin wire, or tip of a

---

[1]Although we often refer to "the" MFIE or "the" EFIE, these equations can be written in many different forms.

1

small-angle cone. Consequently, to determine the scattering from many different kinds of PEC bodies using surface integral equations, the EFIE must be employed.

Both the EFIE and the MFIE have a serious limitation. As Murray [4] and Maue [5] pointed out, the EFIE and the MFIE fail to produce a unique solution for the current on a PEC scatterer at frequencies equal to the resonant frequencies of the interior cavity formed by the surface of the scatterer. Since the density of the cavity resonant frequencies increases rapidly with frequency beyond the first resonance, which for many cavities occurs when the maximum linear dimension is approximately one wavelength, the numerical solution of 3-D multiwavelength bodies is severely hampered by these spurious resonances. In principle, the spurious resonances in the solution for the surface current occur only at discrete frequencies, and for the EFIE they should not contribute to the scattered field [6]. In numerical practice, however, they contaminate the surface current and scattered fields of both the EFIE and MFIE over finite bandwidths about the cavity resonant frequencies. Within these bandwidths the determinants of the solution matrices of the integral equations become too small, and the condition numbers become too large, to produce an accurate numerical solution.

Among the several ways to eliminate the spurious resonances from the original integral equations, the combined-field integral equation (CFIE) and the dual-surface magnetic-field integral equations (DSMFIE) have distinguished themselves in numerical practice as effective, efficient, and convenient alternative integral equations for eliminating the spurious resonances [9, pp. 222-225], [10], [11], [12], [13], [7], [14], [2, ch. 6].

The CFIE [15], [9], [10], [11] is formed by combining the MFIE

$$\hat{n} \times H^{inc}(r) = J(r)/2 - \hat{n} \times \int_S J(r') \times \nabla' G(r, r') dS' \qquad (1)$$

2

with the EFIE

$$\hat{\mathbf{n}} \times \mathbf{E}^{inc}(\mathbf{r}) = \frac{j}{\omega \epsilon_0} \hat{\mathbf{n}} \times \int\limits_S [k^2 \mathbf{J}(\mathbf{r}')G(\mathbf{r},\mathbf{r}') - \nabla'_S \cdot \mathbf{J}(\mathbf{r}')\nabla'G(\mathbf{r},\mathbf{r}')]dS' \tag{2}$$

to get

$$\hat{\mathbf{n}} \times \left[(1-\alpha_0)\mathbf{H}^{inc}(\mathbf{r}) - \frac{\alpha_0}{Z_0}\hat{\mathbf{n}} \times \mathbf{E}^{inc}(\mathbf{r}) \right]$$

$$= (1-\alpha_0) \left[\mathbf{J}(\mathbf{r})/2 - \hat{\mathbf{n}} \times \int\limits_S \mathbf{J}(\mathbf{r}') \times \nabla'G(\mathbf{r},\mathbf{r}')dS' \right]$$

$$- \frac{j\alpha_0}{k}\hat{\mathbf{n}} \times \hat{\mathbf{n}} \times \int\limits_S [k^2 \mathbf{J}(\mathbf{r}')G(\mathbf{r},\mathbf{r}') - \nabla'_S \cdot \mathbf{J}(\mathbf{r}')\nabla'G(\mathbf{r},\mathbf{r}')]dS' \tag{3}$$

where $\mathbf{J}(\mathbf{r})$ is the surface current density on the surface S of the scatterer ($\mathbf{r} \in S$), $\nabla_S \cdot$ is the surface divergence [16, Appendix 2, 18.], $\hat{\mathbf{n}}$ is the outward unit normal from the surface S, ϵ_0, μ_0, and $Z_0 = \sqrt{\mu_0/\epsilon_0}$ are the permittivity, permeability, and impedance of free space, and ($\mathbf{E}^{inc}, \mathbf{H}^{inc}$) are the electric and magnetic fields incident upon the scatterer. Harmonic time dependence of the form $\exp(j\omega t)$ has been suppressed, $k = \omega\sqrt{\mu_0 \epsilon_0}$, and the free-space Green's function is given by

$$G(\mathbf{r},\mathbf{r}') = \frac{\exp(-jk|\mathbf{r}-\mathbf{r}'|)}{4\pi|\mathbf{r}-\mathbf{r}'|}. \tag{4}$$

The combination parameter α_0 is a real constant that can assume values between 0 and 1, with $\alpha_0 = .2$ as a typical choice [17]. Mautz and Harrington [10], [11] give a straightforward proof that the CFIE has a unique solution at all frequencies and therefore eliminates the spurious resonances from the original MFIE and EFIE.

The DSMFIE and dual surface electric-field integral equation (DSEFIE) can be written as [13], [7]

$$\hat{\mathbf{n}} \times \mathbf{H}^d(\mathbf{r}) = \mathbf{J}(\mathbf{r})/2 - \hat{\mathbf{n}} \times \int\limits_S \mathbf{J}(\mathbf{r}') \times \nabla'G^d(\mathbf{r},\mathbf{r}')dS' \tag{5}$$

$$\hat{\mathbf{n}} \times \mathbf{E}^d(\mathbf{r}) = \frac{j}{\omega \epsilon_0} \hat{\mathbf{n}} \times \int_S [k^2 \mathbf{J}(\mathbf{r}') G^d(\mathbf{r}, \mathbf{r}') - \nabla'_S \cdot \mathbf{J}(\mathbf{r}') \nabla' G^d(\mathbf{r}, \mathbf{r}')] dS' \qquad (6)$$

where $\mathbf{H}^d(\mathbf{r})$, $\mathbf{E}^d(\mathbf{r})$, and $G^d(\mathbf{r}, \mathbf{r}')$ are defined as

$$\mathbf{H}^d(\mathbf{r}) = \mathbf{H}^{inc}(\mathbf{r}) + \alpha \mathbf{H}^{inc}(\mathbf{r}^d) \qquad (7)$$

$$\mathbf{E}^d(\mathbf{r}) = \mathbf{E}^{inc}(\mathbf{r}) + \alpha \mathbf{E}^{inc}(\mathbf{r}^d) \qquad (8)$$

$$G^d(\mathbf{r}, \mathbf{r}') = G(\mathbf{r}, \mathbf{r}') + \alpha G(\mathbf{r}^d, \mathbf{r}') \qquad (9)$$

with $\mathbf{r} \in S$ and $\mathbf{r}^d$ lying on a surface S^d a normal distance δ inside S as shown in Fig. 1.

The DSMFIE and DSEFIE in (5) and (6), although identical in form and comparable in complexity to the original MFIE and EFIE, each provide a unique solution for $\mathbf{J}(\mathbf{r})$ at all real frequencies as long as the combination constant α has an imaginary part and the positive real separation constant δ is less than half a wavelength ($\lambda/2$) [13]. In recent numerical practice, we usually choose α equal to $.25j$ and δ between $\lambda/32$ and $\lambda/4$.

It is not necessary for uniqueness of solution to keep the inner surface at a fixed distance δ from the scattering surface as long as δ is less than $\lambda/2$ and large enough to numerically maintain uniqueness of solution. In practice it is not always necessary to include the inner surface for every observation point or to make the inner surface a continuous surface. This means that one can often avoid difficulties in defining the inner surface for scatterers with complicated shapes by simply leaving out the inner surface if it gets closer than a minimum distance δ from any part of the surface S.

The dual-surface integral equations were introduced a number of years ago [18] and the DSMFIE (5) has been successfully applied to multiwavelength rectangular boxes [13], [7] and to bodies of revolution [14], [19]. To date, a numerical solution to the DSEFIE (6) for 3-D

4
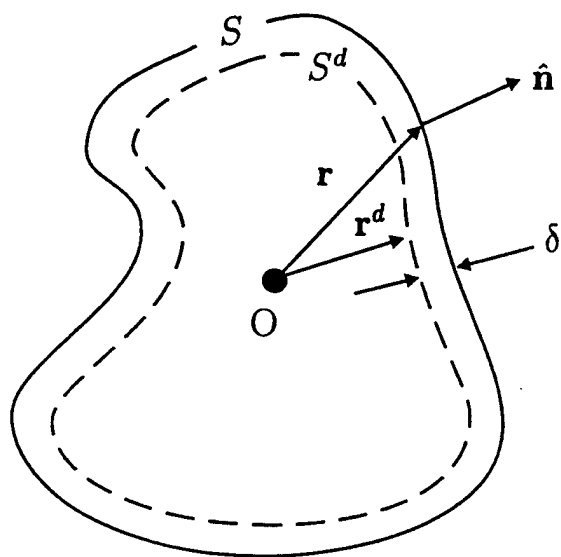
Figure 1. Geometry of a perfectly conducting scatterer with surface S and a fictitious "dual surface" S^d at a normal distance δ inside S. (The value of δ can vary over S.)

scatterers has not been successfully formulated and programmed[2], and thus it is the primary

aim of this report to formulate, test, and document the DSEFIE (6) for bodies of revolution

(BOR's).

What is the utility of a dual-surface integral equation computer program for BOR's

when CFIE computer programs for BOR's are available [21]? We can answer this ques-

tion by reviewing some of our recent work with surface integral equations in connection

with incremental length diffraction coefficients (ILDC's). In order to test the accuracy of

shadow-boundary ILDC's developed to improve upon the accuracy of physical optics (PO)

for calculating high-frequency scattering, we applied them to multiwavelength perfectly con-

ducting BOR's and, in particular, to prolate spheroids [19]. To determine the accuracy of

the calculated PO+ILDC solution, we needed a highly accurate ($< \pm.1$ dB error in the

far-field patterns) numerical solution to the exact field equations for scattering from prolate

spheroids. (No eigenfunction solution exists for electromagnetic scattering from spheroids.)

We used our in-house DSMFIE BOR program to compute the scattering from the prolate

spheroids. (As explained above, the dual surface is required to eliminate the spurious reso-

nances from the solution to the MFIE.) Although we gained some confidence in the DSMFIE

solution by noting convergence of the solution as the surfaces of the spheroids were divided

into smaller and smaller increments, and by comparing the computed and exact Mie series

solutions for the sphere, we could only be sure that the DSMFIE numerical solution was con-

---

[2]A method of moments solution for the DSEFIE applied to BOR's was considered in [20]. Although

the details of the method of moments formulation are not given in [20], they can be determined from the

computer program written in conjunction with [20]. An analysis of this method of moments formulation

revealed that it was invalid for the dual surface part of the DSEFIE.

verging accurately enough to the correct solution for eccentric spheroids if we could compare it to another independent numerical solution.

To obtain a second independent numerical solution for scattering from the prolate spheroids, we used a CFIE computer program called CICERO [21] . The CFIE and the DSMFIE agreed over the entire far-field pattern to within the thickness of the lines used to plot the far-field patterns. Even though the CFIE and DSMFIE are each integral equations, the CFIE combines both the electric and magnetic field operators to form a surface integral equation that is very different from the DSMFIE, which involves only the operator of the magnetic field integral equation. Therefore, the close agreement of the two very different integral equation solutions gave us the confidence to designate these solutions as the "highly accurate reference solution" to which we could compare our approximate high-frequency ILDC solution.

This experience not only confirmed in us an appreciation for surface integral equations, but it also clearly demonstrated the importance of having available two independent surface integral equation formulations that can be applied and solved straightforwardly and efficiently. In the work with spheroids described above, the two surface integral equations we used were the DSMFIE and the CFIE. However, as explained above, for infinitesimally thin conductors (open surfaces), the magnetic field operator degenerates to give an underdetermined set of equations, and for conductors containing narrow-angle wedges and tips, the magnetic field operator becomes unstable. Thus, for many scattering geometries, such

7

as the small-angle cone-sphere, one must use the DSEFIE instead of the DSMFIE.[3]

Consider the following example of using the DSEFIE where the DSMFIE has difficulty producing as accurate a solution. The measured and CFIE-computed radar cross sections of a cone-sphere with a half angle of 7° were shown in [22] to disagree by several dB over a large range of incident angles, and it remained uncertain as to whether the measured data, the CFIE computations, or both contained large errors. Results for this cone-sphere computed with the DSEFIE developed in the present paper agreed very closely with the CFIE results in [22], and thus it was concluded that the large discrepancy between the computed and measured radar cross sections was due mainly to errors in the measured data.

The importance of having two independent surface integral equation formulations is also underlined by the fact that calculating scattering with surface integral equations is often far from being a simple "turn the crank" procedure. As a recent investigation of the convergence properties of the CFIE has shown [23], the value of the CFIE combination parameter α_0 can strongly influence the rate at which scattering calculations converge with increasing grid point density. Similar conclusions apply to our own experience with the influence of the combination parameter α and the separation distance δ on results obtained with the DSEFIE. Careful checking of the results of scattering calculations obtained with surface integral equations is thus very important, and can be done more easily and rigorously if two independent formulations are available.

---

[3]The difficulty with the MFIE and DSMFIE near the tip of a small-angle cone-sphere several wavelengths long has been remedied by inserting the known Bessel function dependence of the exact zeroth order longitudinal tip current of the infinite cone [20, ch. 5]. There is no guarantee, however, that this remedy will work for any shape and size of a BOR containing a narrow tip.

The organization of the report is as follows. Section 2 contains the analysis of the DSEFIE solution of the BOR scattering problem. It is divided into several subsections beginning with the statement of the problem and definition of the geometry in Section 2.1. The formulation of the DSEFIE in terms of the vector and scalar potential functions A and Φ is derived in Section 2.2. The solution of the DSEFIE by the Galerkin form of the method of moments is outlined in Section 2.3. Detailed expressions for the elements of the Z matrices that multiply the column vectors of the surface current expansion function coefficients to be determined are derived in Section 2.4. The Z matrices are treated by expressing them as the sum of four submatrices. Two of these submatrices contain the terms involving the vector potential A, one each for the observation point on the original surface and the dual surface, respectively, and two contain the terms involving the scalar potential Φ, again one each for the observation point on the original and dual surface. It is noteworthy that the procedure of Mautz and Harrington [11] we use to transfer the differential operator on Φ to the testing function when the observation point is on the original surface cannot be used when the observation point lies on the dual surface. In Section 2.5 we obtain detailed expressions for the elements of the V column vectors in the right-hand side of the Galerkin matrix equation formulation of the DSEFIE. In Section 2.6 we obtain expressions for the currents induced on the surface of a BOR by a transverse electric (TE) and transverse magnetic (TM) linearly polarized plane wave in terms of the solution to the Galerkin matrix equation, and in Section 2.7 expressions for the components of the far scattered field are derived. The analysis of Sections 2.4 - 2.7 is general in the sense that no explicit form is assumed for the expansion and testing functions other than the Fourier modes used to express their azimuthal dependence. In Section 2.8 we introduce the four-impulse approximation to a triangle function used to express the

9

dependence of the expansion and testing functions on the BOR generating curve parameter t. This allows the integrations with respect to t of the expansion and testing functions to be carried out in closed form. The expressions for the elements of the Z matrices and V vectors obtained in Sections 2.4 and 2.5, and the expressions for the far scattered field obtained in Section 2.7 are then given as summations that can be readily evaluated by computer. The efficiency of evaluating these summations can be greatly increased by using a change in indexing described in Section 2.9. Section 2.10 discusses the choice of the number of Fourier modes that need to be used in the calculations.

Section 3 contains the results of calculations performed with a DSEFIE computer program written to implement and validate the analysis of Section 2. Section 3.1 shows that the DSEFIE removes a spurious resonance that appears when the backscatter radar cross section (RCS) of a PEC sphere is calculated with the EFIE. Section 3.2 demonstrates the DSEFIE removal of a spurious resonance in the bistatic RCS pattern of a PEC prolate spheroid obtained with the EFIE. Section 3.3 shows the effectiveness of the DSEFIE in eliminating a spurious resonance in the calculation of the bistatic and monostatic patterns of a finite cylinder. Section 3.4 discusses calculations of the bistatic RCS pattern of an axially illuminated PEC cone-sphere, and the special treatment of the dual surface needed when the DSEFIE is applied to a cone-sphere with a narrow tip angle. Section 3.5 continues the discussion of scattering by a cone-sphere with a narrow tip angle by treating monostatic scattering. The monostatic case is significantly different because of the presence of the zeroth order Fourier mode, absent in axial illumination. Section 3.6 discusses the use of half-triangle basis functions at the beginning and end of the generating curve for a BOR. A report summary is given in Section 4.

2 ANALYSIS

2.1 Statement of Problem

We seek to determine the surface current and the far scattered field of a perfectly electrically conducting (PEC) closed body of revolution (BOR) excited by an incident plane wave. The geometry of the BOR is shown in Fig. 2. Circular cylinder coordinates (ρ, ϕ, z) are employed with $(\hat{\rho}, \hat{\phi}, \hat{z})$ denoting the corresponding unit vectors, and with the z axis chosen as the axis of revolution. The origin of the circular cylindrical coordinate system lies on the z axis but does not necessarily coincide with the lower pole of the BOR as in Fig. 2. The coordinates (t, ϕ), with t the pathlength along the generating curve of the BOR from the lower pole, form an orthogonal curvilinear system on the surface S of the BOR; the corresponding unit vectors are $(\hat{t}, \hat{\phi})$. Figure 3 shows the propagation vector $\mathbf{k}^{inc} = k\,\hat{\mathbf{k}}^{inc}$ of the incident plane wave. The propagation vector is assumed to lie in the xz plane ($\phi = 0$), with $-\hat{\mathbf{k}}^{inc}$ making an angle of θ^{inc} with the positive z axis and with $k_x{}^{inc} \leq 0$ so that

$$\mathbf{k}^{inc} = -k(\sin\theta^{inc}\hat{\mathbf{x}} + \cos\theta^{inc}\hat{\mathbf{z}}). \tag{10}$$

The free space propagation constant is given by $k = \omega/c$ where c is the speed of light and $\omega > 0$. Harmonic time dependence $\exp(j\omega t)$ is assumed. Also shown in Fig. 3 are the spherical polar angles of the far field observation point $\mathbf{r}^{far} = (r, \theta^{far}, \phi^{far})$ and the associated unit vectors $\hat{\theta}^{far}$ and $\hat{\phi}^{far}$. For TM illumination the incident electric field is given by

$$\mathbf{E}^{inc} = kZ_0\exp(-j\mathbf{k}^{inc} \cdot \mathbf{r})\hat{\theta}^{inc} \tag{11}$$

11
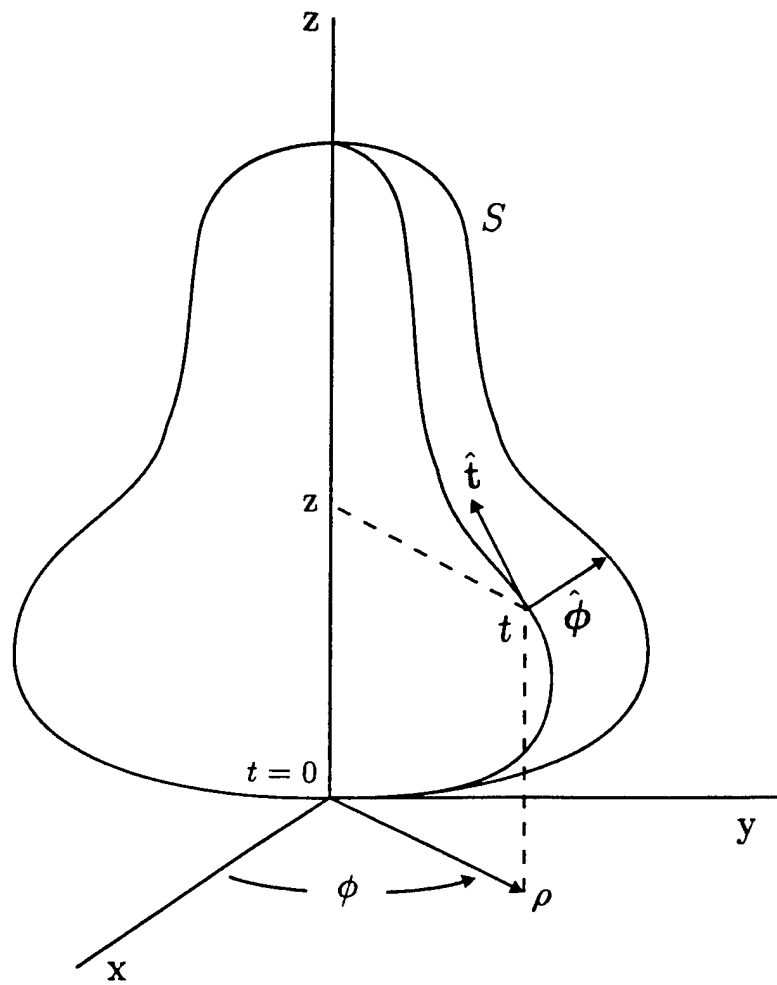
Figure 2. Body of revolution and coordinate system.
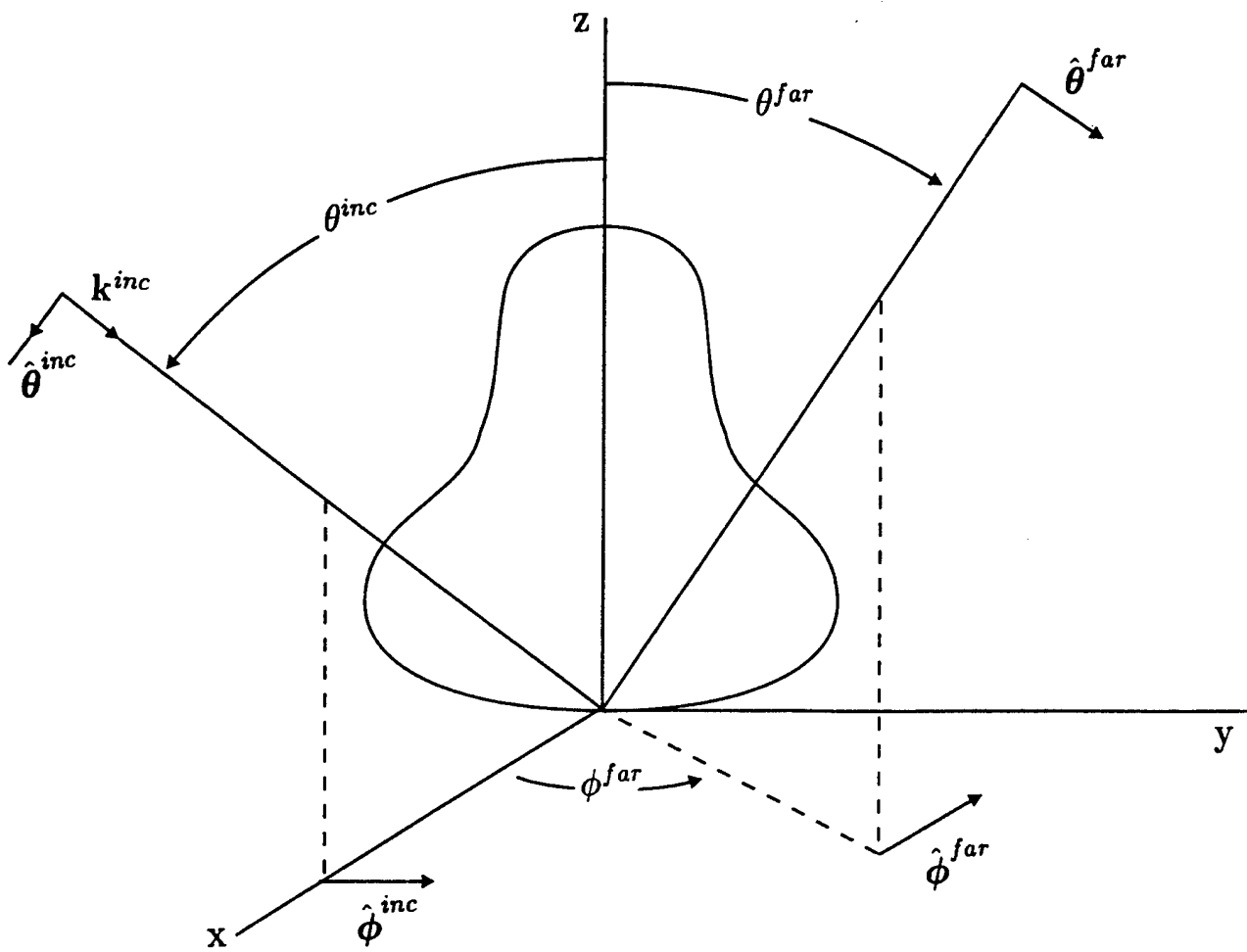
Figure 3. Plane wave scattering by a body of revolution.

while for TE illumination

$$\mathbf{E}^{inc} = kZ_0 \exp(-j\mathbf{k}^{inc} \cdot \mathbf{r})\hat{\phi}^{inc}. \tag{12}$$

In (11) and (12) $\mathbf{r}$ is the vector from the origin to any point in space and Z_0 is the intrinsic impedance of free space. The factor of kZ_0 is inserted to simplify the analysis.

2.2   Derivation of the Dual-Surface Electric-Field Integral Equation

To derive the dual-surface electric-field integral equation (DSEFIE) we first derive the ordinary electric-field integral equation (EFIE). On the surface S of the PEC BOR the total tangential electric field vanishes. The total field is expressed as the sum of the incident field and the scattered field, so that

$$\hat{n}(\mathbf{r}) \times \mathbf{E}^{tot}(\mathbf{r}) = \hat{n}(\mathbf{r}) \times [\mathbf{E}^{inc}(\mathbf{r}) + \mathbf{E}^{sc}(\mathbf{r})] = 0, \ \mathbf{r} \text{ on } S \tag{13}$$

where $\mathbf{E}^{tot}$ and $\mathbf{E}^{sc}$ are the total and scattered electric fields, respectively, and $\hat{n}$ is the unit normal vector to the surface S at $\mathbf{r}$, assumed directed outward from S. The scattered field can be expressed in terms of a vector potential $\mathbf{A}(\mathbf{r}, \mathbf{J})$ and a scalar potential $\Phi(\mathbf{r}, \mathbf{J})$ by

$$\mathbf{E}^{sc}(\mathbf{r}) = -j\omega \mathbf{A}(\mathbf{r}, \mathbf{J}) - \nabla\Phi(\mathbf{r}, \mathbf{J}) \tag{14}$$

where

$$\mathbf{A}(\mathbf{r}, \mathbf{J}) = \mu_0 \int_S \mathbf{J}(\mathbf{r}')G(\mathbf{r}, \mathbf{r}')dS' \tag{15}$$

and

$$\Phi(\mathbf{r}, \mathbf{J}) = \frac{1}{\epsilon_0} \int_S \sigma(\mathbf{r}')G(\mathbf{r}, \mathbf{r}')dS'. \tag{16}$$

14

Here $G(\mathbf{r}, \mathbf{r}')$ is the free-space Green's function

$$G(\mathbf{r}, \mathbf{r}') = \frac{\exp(-jk \mid \mathbf{r} - \mathbf{r}' \mid)}{4\pi \mid \mathbf{r} - \mathbf{r}' \mid}, \tag{17}$$

$\mathbf{r}$ and $\mathbf{r}'$ are the vectors to the field and source points respectively, $\mathbf{J}(\mathbf{r}')$ is the electric current on S to be determined, μ_0 and ϵ_0 are the permeability and permittivity of free space respectively, and σ is the surface charge density given by

$$\sigma(\mathbf{r}') = -\frac{1}{j\omega}\nabla'_S \cdot \mathbf{J}(\mathbf{r}') \tag{18}$$

where the operator $\nabla'_S\cdot$ is the surface divergence [16, Appendix 2, 18.]. Combining (13) and (14) and dividing by the free-space impedance $Z_0 = (\mu_0/\epsilon_0)^{1/2}$ we obtain

$$\frac{\hat{\mathbf{n}}(\mathbf{r})}{Z_0} \times [j\omega\mathbf{A}(\mathbf{r}, \mathbf{J}) + \nabla\Phi(\mathbf{r}, \mathbf{J})] = \frac{\hat{\mathbf{n}}(\mathbf{r})}{Z_0} \times \mathbf{E}^{inc}(\mathbf{r}), \ \mathbf{r} \text{ on } S. \tag{19}$$

Equation (19) with $\mathbf{A}$ and Φ given by (15) and (16) is the potential form of the EFIE for the current on the surface S of the BOR.

To obtain the DSEFIE we note that for points inside of S the total electric field vanishes so that

$$\mathbf{E}^{sc}(\mathbf{r}) = -\mathbf{E}^{inc}(\mathbf{r}), \ \mathbf{r} \text{ inside } S. \tag{20}$$

With (14)-(16), (20) can be written as

$$j\omega\mathbf{A}(\mathbf{r}, \mathbf{J}) + \nabla\Phi(\mathbf{r}, \mathbf{J}) = \mathbf{E}^{inc}(\mathbf{r}), \ \mathbf{r} \text{ inside } S. \tag{21}$$

In (21) we can now let $\mathbf{r}$ lie on a surface S_δ parallel to, and a small distance $\delta > 0$ inside, the actual surface of the BOR. If $\mathbf{r}^d(\mathbf{r})$ denotes the point on the dual surface corresponding

15

to a point $\mathbf{r}$ on the original surface[4] then

$$j\omega\mathbf{A}(\mathbf{r}^d(\mathbf{r}),\mathbf{J}) + \nabla_{\mathbf{r}^d}\Phi(\mathbf{r}^d(\mathbf{r}),\mathbf{J}) = \mathbf{E}^{inc}(\mathbf{r}^d(\mathbf{r})), \ \mathbf{r} \text{ on } S. \tag{22}$$

Dividing (22) by Z_0 and adding $\alpha\hat{\mathbf{n}}(\mathbf{r}) \times$ (22) to (19) yields the DSEFIE

$$\frac{\hat{\mathbf{n}}(\mathbf{r})}{Z_0} \times \left[j\omega\mathbf{A}(\mathbf{r},\mathbf{J}) + j\alpha\omega\mathbf{A}(\mathbf{r}^d(\mathbf{r}),\mathbf{J}) + \nabla_{\mathbf{r}}\Phi(\mathbf{r},\mathbf{J}) + \alpha\nabla_{\mathbf{r}^d}\Phi(\mathbf{r}^d(\mathbf{r}),\mathbf{J}) \right]$$

$$= \frac{\hat{\mathbf{n}}(\mathbf{r})}{Z_0} \times \left[\mathbf{E}^{inc}(\mathbf{r}) + \alpha\mathbf{E}^{inc}(\mathbf{r}^d(\mathbf{r})) \right], \ \mathbf{r} \text{ on } S. \tag{23}$$

If the combination constant α has an imaginary part and the separation distance δ is less than half a wavelength the DSEFIE (23) provides a unique solution for $\mathbf{J}(\mathbf{r})$ at all real frequencies [13], unlike the conventional EFIE (19). We have found that choosing $\alpha = .25j$ has worked well for the BOR's we have considered.

2.3 Solution of the DSEFIE by the Galerkin Form of the Method of Moments

To solve the DSEFIE (23) for the surface current $\mathbf{J}$ we employ the method of moments and let

$$\mathbf{J} = \sum_n \sum_j \left(I_{nj}^t \mathbf{J}_{nj}^t + I_{nj}^\phi \mathbf{J}_{nj}^\phi \right) \tag{24}$$

where $\mathbf{J}_{nj}^t$ and $\mathbf{J}_{nj}^\phi$ are the expansion (basis) functions of the BOR surface coordinates t and ϕ,

$$\mathbf{J}_{nj}^t = \hat{\mathbf{t}}f_j(t)e^{jn\phi}, n = 0,\pm1,\pm2,\cdots, \tag{25a}$$

---

[4]For smooth generating curves $\mathbf{r}^d$ can be obtained from $\mathbf{r}$ by setting $\mathbf{r}^d(\mathbf{r}) = \mathbf{r} - \delta\hat{\mathbf{n}}(\mathbf{r})$. For generating curves with corners, however, a correspondence such as shown in Fig. 4 for the generating curve of the finite cylinder may be preferable.
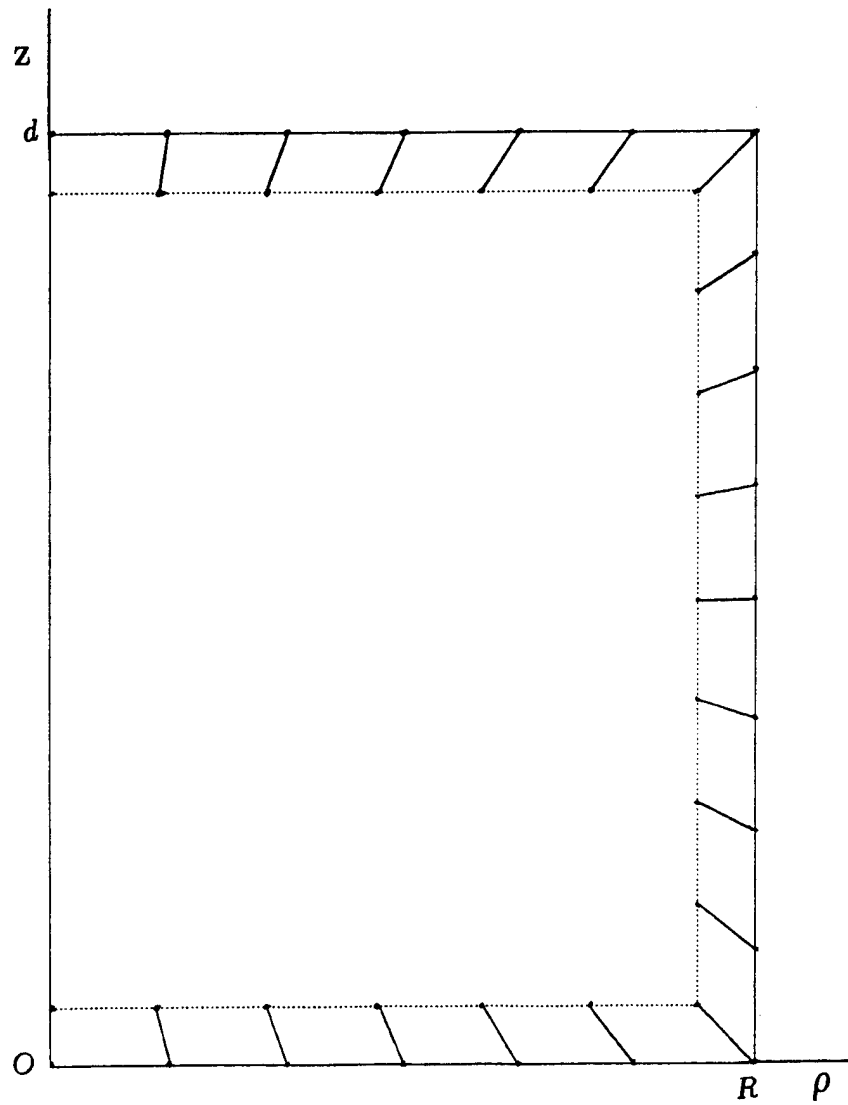
Figure 4. Correspondence between points on the body of revolution generating curve for a finite cylinder and points on the dual-surface generating curve.

$$\mathbf{J}_{nj}^{\phi} = \hat{\phi} f_j(t) e^{jn\phi}, n = 0, \pm 1, \pm 2, \cdots, \tag{25b}$$

I_{nj}^t and I_{nj}^{ϕ} are coefficients to be determined, and the summation over the Fourier modes $e^{jn\phi}$ is from $-N$ to N. The choice of the functions $f_j(t)$ is treated below in Section 2.8, and the value of N discussed in Section 2.10.

Next, using the Galerkin method, the dot product of (23) with each one of a collection of testing functions $\mathbf{W}_{mi}^t, \mathbf{W}_{mi}^{\phi}$ defined by

$$\mathbf{W}_{mi}^t = \hat{t} f_i(t) e^{-jm\phi}, m = 0, \pm 1, \pm 2, \cdots, \pm N, \tag{26a}$$

$$\mathbf{W}_{mi}^{\phi} = \hat{\phi} f_i(t) e^{-jm\phi}, m = 0, \pm 1, \pm 2, \cdots, \pm N \tag{26b}$$

is integrated over S and use is made of the fact that $\hat{n}, \hat{\phi}, \hat{t}$ form an orthogonal triad of vectors to yield the matrix equations

$$\sum_n ([Z_{mn}^{tt}] \mathbf{I}_n^t + [Z_{mn}^{t\phi}] \mathbf{I}_n^{\phi}) = \mathbf{V}_m^t \tag{27a}$$

$$\sum_n ([Z_{mn}^{\phi t}] \mathbf{I}_n^t + [Z_{mn}^{\phi\phi}] \mathbf{I}_n^{\phi}) = \mathbf{V}_m^{\phi} \tag{27b}$$

where the $Z's$ are square matrices whose ij^{th} elements are given by

$$[Z_{mn}^{pq}]_{ij} = \frac{1}{Z_0} \int\limits_S \mathbf{W}_{mi}^p \cdot \left[j\omega \mathbf{A}(\mathbf{r}, \mathbf{J}_{nj}^q) + j\alpha\omega \mathbf{A}(\mathbf{r}^d(\mathbf{r}), \mathbf{J}_{nj}^q) \right.$$
$$\left. + \nabla_{\mathbf{r}} \Phi(\mathbf{r}, \mathbf{J}_{nj}^q) + \alpha \nabla_{\mathbf{r}^d} \Phi(\mathbf{r}^d(\mathbf{r}), \mathbf{J}_{nj}^q) \right] dS, \tag{28}$$

$\mathbf{V}_m^t$ and $\mathbf{V}_m^{\phi}$ are column vectors whose i^{th} elements are

$$V_{mi}^p = \frac{1}{Z_0} \int\limits_S \mathbf{W}_{mi}^p \cdot \left[\mathbf{E}^{inc} + \alpha \mathbf{E}^{inc}(\mathbf{r}^d(\mathbf{r})) \right] dS, \tag{29}$$

and $\mathbf{I}_n^t, \mathbf{I}_n^{\phi}$ are the column vectors of the coefficients of the expansion functions in (24). In (28) and (29) p and q, which can be either t or ϕ, indicate the unit vectors of the testing and expansion functions, respectively.

18

2.4 Expressions for the Elements of the Z Matrices

Detailed expressions are now obtained for the elements of the Z matrices given by (28). We write

$$[Z_{mn}^{pq}]_{ij} = [Z_{mn}^{pq}]_{ij}^{\mathbf{A}} + \alpha[Z_{mn}^{pq}]_{ij}^{\mathbf{A}^d} + [Z_{mn}^{pq}]_{ij}^{\Phi} + \alpha[Z_{mn}^{pq}]_{ij}^{\Phi^d} \tag{30}$$

with

$$[Z_{mn}^{pq}]_{ij}^{\mathbf{A}} = \frac{1}{Z_0} \int_S \mathbf{W}_{mi}^p \cdot j\omega \mathbf{A}(\mathbf{r}, \mathbf{J}_{nj}^q) dS, \tag{31a}$$

$$[Z_{mn}^{pq}]_{ij}^{\mathbf{A}^d} = \frac{1}{Z_0} \int_S \mathbf{W}_{mi}^p \cdot j\omega \mathbf{A}(\mathbf{r}^d(\mathbf{r}), \mathbf{J}_{nj}^q) dS, \tag{31b}$$

$$[Z_{mn}^{pq}]_{ij}^{\Phi} = \frac{1}{Z_0} \int_S \mathbf{W}_{mi}^p \cdot \nabla_{\mathbf{r}} \Phi(\mathbf{r}, \mathbf{J}_{nj}^q) dS, \tag{31c}$$

$$[Z_{mn}^{pq}]_{ij}^{\Phi^d} = \frac{1}{Z_0} \int_S \mathbf{W}_{mi}^p \cdot \nabla_{\mathbf{r}^d} \Phi(\mathbf{r}^d(\mathbf{r}), \mathbf{J}_{nj}^q) dS, \tag{31d}$$

and treat each of these four terms in turn. The superscript d is used here and below to indicate dependence on the dual surface. The superscripts p and q indicate the unit vectors of the testing functions and the expansion functions, respectively.

Equation (31a) together with (15), (17), (25), and (26) becomes

$$[Z_{mn}^{pq}]_{ij}^{\mathbf{A}} = jk \int dt \int_{-\pi}^{\pi} \rho d\phi \int dt' \int_{-\pi}^{\pi} \rho' d\phi' f_i(t) f_j(t') (\hat{\mathbf{p}} \cdot \hat{\mathbf{q}}') e^{jn\phi'} e^{-jm\phi} G(\mathbf{r}, \mathbf{r}'). \tag{32}$$

In (32) and the following, quantities with primes are associated with the source point (expansion function) integration and unprimed quantities are associated with the observation point (testing function) integration. The integrations with respect to t and t' are from 0 (the lower pole of the BOR, see Fig. 2) to the length of the generating curve for the BOR, the value of t and t' at the upper pole of the BOR. It is easy to establish the unit vector

relations[5]

$$\hat{\mathbf{t}} \cdot \hat{\mathbf{t}}' = \sin v(t) \sin v'(t') \cos(\phi' - \phi) + \cos v(t) \cos v'(t'), \tag{33a}$$

$$\hat{\mathbf{t}} \cdot \hat{\boldsymbol{\phi}}' = -\sin v(t) \sin(\phi' - \phi), \tag{33b}$$

$$\hat{\boldsymbol{\phi}} \cdot \hat{\mathbf{t}}' = \sin v'(t') \sin(\phi' - \phi), \tag{33c}$$

and

$$\hat{\boldsymbol{\phi}} \cdot \hat{\boldsymbol{\phi}}' = \cos(\phi' - \phi), \tag{33d}$$

where v and v' are the angles measured positive clockwise from the positive z axis to $\hat{\mathbf{t}}$ and $\hat{\mathbf{t}}'$ respectively (see Fig. 5). It is also simple to show that

$$| \mathbf{r} - \mathbf{r}' | = \left[\rho^2 + \rho'^2 - 2\rho\rho' \cos(\phi - \phi') + (z - z')^2 \right]^{1/2}$$

$$= \left[(\rho - \rho')^2 + (z - z')^2 + 4\rho\rho' \sin^2(\frac{\phi' - \phi}{2}) \right]^{1/2}. \tag{34}$$

In view of (33) and (34) the ϕ and ϕ' integrations in (32) are of the form

$$\int_{-\pi}^{\pi} d\phi e^{-jm\phi} \int_{-\pi}^{\pi} d\phi' e^{jn\phi'} f(\phi' - \phi) = \int_{-\pi}^{\pi} d\phi e^{j(n-m)\phi} \int_{-\pi}^{\pi} d\phi' e^{jn(\phi'-\phi)} f(\phi' - \phi)$$

$$= 2\pi\delta_{nm} \int_{-\pi}^{\pi} d\phi' e^{jn\phi'} f(\phi') \tag{35}$$

where the Kronecker delta δ_{nm} equals 0 for $m \neq n$ and equals 1 for $m = n$, and we have used the 2π-periodicity of the ϕ'-integrand to set $\phi = 0$. Hence

$$[Z_{mn}^{pq}]_{ij}^{\mathbf{A}} = [Z_n^{pq}]_{ij}^{\mathbf{A}} = j2\pi k \int dt \rho f_i(t) \int dt' \rho' f_j(t') \int_{-\pi}^{\pi} d\phi' (\hat{\mathbf{p}} \cdot \hat{\mathbf{q}}') e^{jn\phi'} G(R) \tag{36}$$

---

[5]Equations (33a-d) follow directly from noting that

$$\hat{\mathbf{t}} = \cos v(t)\hat{\mathbf{z}} + \sin v(t)\hat{\boldsymbol{\rho}} = \sin v(t) \cos \phi \hat{\mathbf{x}} + \sin v(t) \sin \phi \hat{\mathbf{y}} + \cos v(t)\hat{\mathbf{z}},$$

$$\hat{\boldsymbol{\phi}} = -\sin \phi \hat{\mathbf{x}} + \cos \phi \hat{\mathbf{y}},$$

and similarly for $\hat{\mathbf{t}}'$ and $\hat{\boldsymbol{\phi}}'$.
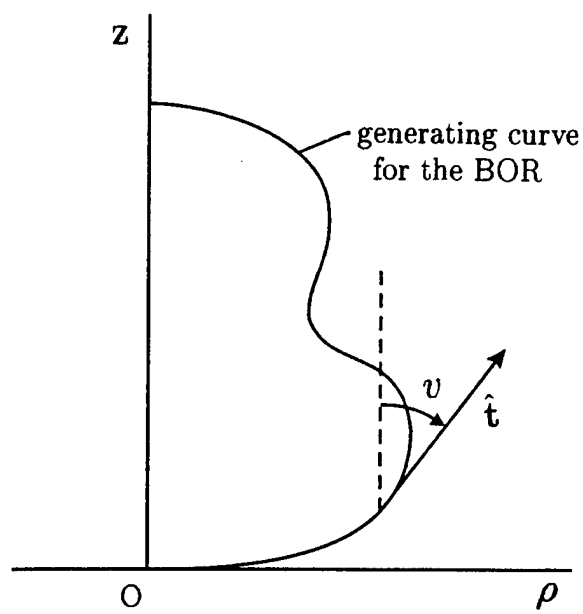
Figure 5. Defining geometry for the angle v in the ρz plane.

where, from (33) and (34) with $\phi = 0$,

$$\hat{\mathbf{t}} \cdot \hat{\mathbf{t}}' = \sin v(t) \sin v'(t') \cos \phi' + \cos v(t) \cos v'(t'), \tag{37a}$$

$$\hat{\mathbf{t}} \cdot \hat{\boldsymbol{\phi}}' = -\sin v(t) \sin \phi', \tag{37b}$$

$$\hat{\boldsymbol{\phi}} \cdot \hat{\mathbf{t}}' = \sin v'(t') \sin \phi', \tag{37c}$$

$$\hat{\boldsymbol{\phi}} \cdot \hat{\boldsymbol{\phi}}' = \cos \phi', \tag{37d}$$

and

$$R = \mid \mathbf{r} - \mathbf{r}' \mid = \left[(\rho - \rho')^2 + (z - z')^2 + 4\rho\rho' \sin^2(\frac{\phi'}{2}) \right]^{1/2}. \tag{38}$$

Then

$$[Z_n^{tt}]_{ij}^{\mathbf{A}} = j2\pi k \int dt \rho f_i(t) \int dt' \rho' f_j(t')$$

$$\cdot \int_{-\pi}^{\pi} d\phi' G(R) e^{jn\phi'} \left[\sin v(t) \sin v'(t') \cos \phi' + \cos v(t) \cos v'(t') \right], \tag{39a}$$

$$[Z_n^{\phi t}]_{ij}^{\mathbf{A}} = j2\pi k \int dt \rho f_i(t) \int dt' \rho' f_j(t') \sin v'(t') \int_{-\pi}^{\pi} d\phi' G(R) e^{jn\phi'} \sin \phi', \tag{39b}$$

$$[Z_n^{t\phi}]_{ij}^{\mathbf{A}} = -j2\pi k \int dt \rho f_i(t) \sin v(t) \int dt' \rho' f_j(t') \int_{-\pi}^{\pi} d\phi' G(R) e^{jn\phi'} \sin \phi', \tag{39c}$$

and

$$[Z_n^{\phi\phi}]_{ij}^{\mathbf{A}} = j2\pi k \int dt \rho f_i(t) \int dt' \rho' f_j(t') \int_{-\pi}^{\pi} d\phi' G(R) e^{jn\phi'} \cos \phi'. \tag{39d}$$

Making use of the symmetries in the ϕ' integrations in (39), we obtain

$$[Z_n^{tt}]_{ij}^{\mathbf{A}} = jk^2 \int dt \rho f_i(t) \int dt' \rho' f_j(t') \Big[\sin v(t) \sin v'(t') G_{2,n}(\rho, \rho', z - z')$$

$$+ \cos v(t) \cos v'(t') G_{1,n}(\rho, \rho', z - z') \Big],$$

$$\tag{40a}$$

22

$$[Z_n^{\phi t}]_{ij}^{\mathbf{A}} = -k^2 \int dt \rho f_i(t) \int dt' \rho' f_j(t') \sin v'(t') G_{3,n}(\rho, \rho', z - z'), \tag{40b}$$

$$[Z_n^{t\phi}]_{ij}^{\mathbf{A}} = k^2 \int dt \rho f_i(t) \sin v(t) \int dt' \rho' f_j(t') G_{3,n}(\rho, \rho', z - z'), \tag{40c}$$

and

$$[Z_n^{\phi\phi}]_{ij}^{\mathbf{A}} = jk^2 \int dt \rho f_i(t) \int dt' \rho' f_j(t') G_{2,n}(\rho, \rho', z - z'), \tag{40d}$$

where

$$G_{1,n}(\rho, \rho', z - z') = \int_0^\pi G_0(R) \cos(n\phi') d\phi', \tag{41a}$$

$$G_{2,n}(\rho, \rho', z - z') = \int_0^\pi G_0(R) \cos(n\phi') \cos\phi' d\phi', \tag{41b}$$

and

$$G_{3,n}(\rho, \rho', z - z') = \int_0^\pi G_0(R) \sin(n\phi') \sin\phi' d\phi', \tag{41c}$$

with

$$G_0(R) = \frac{\exp(-jkR)}{kR} \tag{41d}$$

and R given by (38). In the arguments of the $G_{k,n}, k = 1, 2, 3$, ρ and z are functions of the observation point coordinate t, and ρ' and z' are functions of the source point coordinate t'. Equations (40a-d), the detailed expressions for (31a-d), are in terms of the t dependence, $f_i(t)$, of the expansion and testing functions discussed below in Section 2.8. Referring to (38) it can be seen that $R = 0$ when $\rho' = \rho$, $z' = z$, and $\phi' = 0$, so that $G_{1,n}(\rho, \rho', z - z')$ and $G_{2,n}(\rho, \rho', z - z')$ become singular. This problem will also be treated in Section 2.8.

Turning next to (31b) it can be seen that the treatment of (31a) carries over if $\mathbf{r}^d = (\rho^d, \phi, z^d)$ is substituted for $\mathbf{r}$ in (32) and (34). (Note that the value of ϕ is the same for corresponding points $\mathbf{r}$ and $\mathbf{r}^d(\mathbf{r})$, and that the testing function integrations are performed

23

on the surface of the BOR.) Hence letting

$$R^d = \mid \mathbf{r}^d - \mathbf{r}' \mid, \tag{42}$$

$$
\begin{aligned}
{[Z_n^{tt}]_{ij}^{\mathbf{A}^d}} &= jk^2 \int dt \rho f_i(t) \int dt' \rho' f_j(t') \Big[\sin v(t) \sin v'(t') G_{2,n}(\rho^d, \rho', z^d - z') \\
&+ \cos v(t) \cos v'(t') G_{1,n}(\rho^d, \rho', z^d - z') \Big],
\end{aligned}
$$

$$\tag{43a}$$

$$[Z_n^{\phi t}]_{ij}^{\mathbf{A}^d} = -k^2 \int dt \rho f_i(t) \int dt' \rho' f_j(t') \sin v'(t') G_{3,n}(\rho^d, \rho', z^d - z'), \tag{43b}$$

$$[Z_n^{t\phi}]_{ij}^{\mathbf{A}^d} = k^2 \int dt \rho f_i(t) \sin v(t) \int dt' \rho' f_j(t') G_{3,n}(\rho^d, \rho', z^d - z'), \tag{43c}$$

and

$$[Z_n^{\phi\phi}]_{ij}^{\mathbf{A}^d} = jk^2 \int dt \rho f_i(t) \int dt' \rho' f_j(t') G_{2,n}(\rho^d, \rho', z^d - z'), \tag{43d}$$

where the $G_{k,n}, k = 1, 2, 3$, are defined as in (41a-d) with R replaced by R^d. It should be noted that unlike R defined by (38), R^d defined by (42) cannot equal zero and so there are no singularities of the integrands of $G_{1,n}(\rho^d, \rho', z^d - z')$, $G_{2,n}(\rho^d, \rho', z^d - z')$, and $G_{3,n}(\rho^d, \rho', z^d - z')$.

Next, addressing (31c), we first show that [11]

$$\int_S \mathbf{W}_{mi}^p \cdot \nabla_{\mathbf{r}} \Phi(\mathbf{r}, \mathbf{J}_{nj}^q) dS = -\int_S (\nabla_S \cdot \mathbf{W}_{mi}^p) \Phi(\mathbf{r}, \mathbf{J}_{nj}^q) dS, \tag{44}$$

where $\nabla_S \cdot$ is the surface divergence operator [16, Appendix 2, 18.]. The importance of (44) is that the integrable singularity of $\mid \mathbf{r} - \mathbf{r}' \mid^{-1}$ in the Green's function $G(\mathbf{r}, \mathbf{r}')$ given by (17) is thereby not converted to a singularity of higher order $\mid \mathbf{r} - \mathbf{r}' \mid^{-2}$ by the operator $\nabla_{\mathbf{r}}$ acting on Φ in the left-hand side of (44). To prove (44) we start with the relationship

$$\int_S \nabla_S \cdot (\Phi \mathbf{W}_{mi}^p) dS = 0 \tag{45}$$

24

which holds because S is closed and $\mathbf{W}_{mi}^p$ is tangential to S [16, Appendix 2, 42.]. Since

$$\nabla_S \cdot (\Phi \mathbf{W}_{mi}^p) = \mathbf{W}_{mi}^p \cdot \nabla_S \Phi + (\nabla_S \cdot \mathbf{W}_{mi}^p)\Phi, \tag{46}$$

we have

$$\int_S \mathbf{W}_{mi}^p \cdot \nabla_S \Phi dS = -\int_S (\nabla_S \cdot \mathbf{W}_{mi}^p)\Phi dS \tag{47}$$

and (44) follows from noting that in (47) $\nabla_S \Phi$ can be replaced by $\nabla \Phi$ because $\mathbf{W}_{mi}^p$ is tangential to S. Equation (31c) together with (44),(16),(17), and (18) then becomes

$$[Z_{mn}^{pq}]_{ij}^\Phi = -\frac{j}{k} \int_S dS \int_S dS'(\nabla_S \cdot \mathbf{W}_{mi}^p)(\nabla_S' \cdot \mathbf{J}_{nj}^q)G(\mathbf{r}, \mathbf{r}'). \tag{48}$$

Now

$$\nabla_S' \cdot \mathbf{J}_{nj}^t = \frac{1}{\rho'}\frac{d}{dt'}[\rho' f_j(t')]e^{jn\phi'}, \tag{49a}$$

$$\nabla_S' \cdot \mathbf{J}_{nj}^\phi = \frac{jn}{\rho'}f_j(t')e^{jn\phi'}, \tag{49b}$$

$$\nabla_S \cdot \mathbf{W}_{mi}^t = \frac{1}{\rho}\frac{d}{dt}[\rho f_i(t)]e^{jn\phi'}, \tag{49c}$$

and

$$\nabla_S \cdot \mathbf{W}_{mi}^\phi = -\frac{jn}{\rho}f_i(t)e^{jn\phi'}. \tag{49d}$$

Hence

$$[Z_{mn}^{tt}]_{ij}^\Phi = -\frac{j}{k}\int dt \frac{1}{\rho}\frac{d}{dt}[\rho f_i(t)] \int_{-\pi}^{\pi} d\phi \rho e^{-jm\phi} \int dt' \frac{1}{\rho'}\frac{d}{dt'}[\rho' f_j(t')] \int_{-\pi}^{\pi} d\phi' \rho' e^{jn\phi'} G(\mid \mathbf{r} - \mathbf{r}' \mid),$$

$$\tag{50a}$$

$$[Z_{mn}^{\phi t}]_{ij}^\Phi = -\frac{n}{k}\int dt \frac{f_i(t)}{\rho} \int_{-\pi}^{\pi} d\phi \rho e^{-jm\phi} \int dt' \frac{1}{\rho'}\frac{d}{dt'}[\rho' f_j(t')] \int_{-\pi}^{\pi} d\phi' \rho' e^{jn\phi'} G(\mid \mathbf{r} - \mathbf{r}' \mid), \tag{50b}$$

$$[Z_{mn}^{t\phi}]_{ij}^\Phi = \frac{n}{k}\int dt \frac{1}{\rho}\frac{d}{dt}[\rho f_i(t)] \int_{-\pi}^{\pi} d\phi \rho e^{-jm\phi} \int dt' \frac{f_j(t')}{\rho'} \int_{-\pi}^{\pi} d\phi' \rho' e^{jn\phi'} G(\mid \mathbf{r} - \mathbf{r}' \mid), \tag{50c}$$

25

and

$$[Z_{mn}^{\phi\phi}]_{ij}^{\Phi} = -\frac{jnm}{k} \int dt \frac{f_i(t)}{\rho} \int_{-\pi}^{\pi} d\phi \rho e^{-jm\phi} \int dt' \frac{f_j(t')}{\rho'} \int_{-\pi}^{\pi} d\phi' \rho' e^{jn\phi'} G(|\mathbf{r} - \mathbf{r}'|). \qquad (50d)$$

Just as for $[Z_{mn}^{pq}]_{ij}^{\mathbf{A}}$ the ϕ and ϕ' integrations in (50) are treated using (35) and the symmetries of the resulting ϕ' integrations then yield

$$[Z_n^{tt}]_{ij}^{\Phi} = -j \int dt \frac{d}{dt}[\rho f_i(t)] \int dt' \frac{d}{dt'}[\rho' f_j(t')] G_{1,n}(\rho, \rho', z - z'), \qquad (51a)$$

$$[Z_n^{\phi t}]_{ij}^{\Phi} = -n \int dt \frac{\rho f_i(t)}{\rho} \int dt' \frac{d}{dt'}[\rho' f_j(t')] G_{1,n}(\rho, \rho', z - z'), \qquad (51b)$$

$$[Z_n^{t\phi}]_{ij}^{\Phi} = n \int dt \frac{d}{dt}[\rho f_i(t)] \int dt' \frac{\rho' f_j(t')}{\rho'} G_{1,n}(\rho, \rho', z - z'), \qquad (51c)$$

and

$$[Z_n^{\phi\phi}]_{ij}^{\Phi} = -jn^2 \int dt \frac{\rho f_i(t)}{\rho} \int dt' \frac{\rho' f_j(t')}{\rho'} G_{1,n}(\rho, \rho', z - z'). \qquad (51d)$$

Finally we turn our attention to (31d). Here it is not possible to use the device of (44) to transfer the differential operator on Φ to the testing function $\mathbf{W}_{mi}^p$ because the gradient operates with respect to points on the dual surface. Hence, using (16),(17), and (18), we obtain

$$\nabla_{\mathbf{r}^d} \Phi(\mathbf{r}^d(\mathbf{r}), \mathbf{J}_{nj}^q) = \frac{1}{j\omega\epsilon_o} \int_S [\nabla'_S \cdot \mathbf{J}_{nj}^q(r')] \frac{1 + jk|\mathbf{r}^d - \mathbf{r}'|}{4\pi|\mathbf{r}^d - \mathbf{r}'|^3} e^{-jk|\mathbf{r}^d - \mathbf{r}'|}(\mathbf{r}^d - \mathbf{r}') dS' \qquad (52)$$

so that

$$[Z_{mn}^{pq}]_{ij}^{\Phi d} = -\frac{j}{k} \int_S dS \int_S dS'[\nabla'_S \cdot \mathbf{J}_{nj}^q(r')] \frac{1 + jk|\mathbf{r}^d - \mathbf{r}'|}{4\pi|\mathbf{r}^d - \mathbf{r}'|^3} e^{-jk|\mathbf{r}^d - \mathbf{r}'|} \mathbf{W}_{mi}^p \cdot (\mathbf{r}^d - \mathbf{r}'). \qquad (53)$$

It is simple to establish the relations (see the footnote regarding (33a-d))

$$\hat{\mathbf{t}} \cdot (\mathbf{r}^d - \mathbf{r}') = \rho^d \sin v(t) - \rho' \sin v(t) \cos(\phi' - \phi) + (z^d - z') \cos v(t) \qquad (54a)$$

26

and

$$\hat{\boldsymbol{\phi}} \cdot (\mathbf{r}^d - \mathbf{r}') = -\rho' \sin(\phi' - \phi). \tag{54b}$$

Hence (53) together with (54) and (49a,b) yields

$$
\begin{aligned}
[Z_{mn}^{tt}]_{ij}^{\Phi^d} \;=\; & -\frac{j}{k} \int dt f_i(t) \int\limits_{-\pi}^{\pi} d\phi \rho e^{-jm\phi} \int dt' \frac{1}{\rho'} \frac{d}{dt'}[\rho' f_j(t')] \int\limits_{-\pi}^{\pi} d\phi' \rho' e^{jn\phi'} \\
& \cdot \left[\rho^d \sin v(t) - \rho' \sin v(t) \cos(\phi' - \phi) + (z^d - z') \cos v(t)\right] H(R^d),
\end{aligned}
$$

$$\tag{55a}$$

$$[Z_{mn}^{\phi t}]_{ij}^{\Phi^d} = \frac{j}{k} \int dt f_i(t) \int\limits_{-\pi}^{\pi} d\phi \rho e^{-jm\phi} \int dt' \frac{1}{\rho'} \frac{d}{dt'}[\rho' f_j(t')] \int\limits_{-\pi}^{\pi} d\phi' \rho'^2 e^{jn\phi'} \sin(\phi' - \phi) H(R^d), \tag{55b}$$

$$
\begin{aligned}
[Z_{mn}^{t\phi}]_{ij}^{\Phi^d} \;=\; & \frac{n}{k} \int dt f_i(t) \int\limits_{-\pi}^{\pi} d\phi \rho e^{-jm\phi} \int dt' \frac{1}{\rho'} f_j(t') \int\limits_{-\pi}^{\pi} d\phi' \rho' e^{jn\phi'} \\
& \cdot \left[\rho^d \sin v(t) - \rho' \sin v(t) \cos(\phi' - \phi) + (z^d - z') \cos v(t)\right] H(R^d),
\end{aligned}
$$

$$\tag{55c}$$

and

$$[Z_{mn}^{\phi\phi}]_{ij}^{\Phi^d} = -\frac{n}{k} \int dt f_i(t) \int\limits_{-\pi}^{\pi} d\phi \rho e^{-jm\phi} \int dt' \frac{1}{\rho'} f_j(t') \int\limits_{-\pi}^{\pi} d\phi' \rho'^2 e^{jn\phi'} \sin(\phi' - \phi) H(R^d), \tag{55d}$$

where we have let

$$H(R^d) = \frac{1 + jkR^d}{4\pi R^{d3}} e^{-jkR^d} \tag{56}$$

with

$$R^d = |\, \mathbf{r}^d - \mathbf{r}' \,| \,. \tag{57}$$

Once again the ϕ and ϕ' integrations are treated using (35), and the symmetries of the resulting ϕ' integrations then yield

$$[Z_n^{tt}]_{ij}^{\Phi^d} = -jk^2 \int dt \rho f_i(t) \int dt' \frac{d}{dt'}[\rho' f_j(t')]$$

$$\cdot \left\{ \left[\rho^d \sin v(t) + (z^d - z') \cos v(t)\right] H_{1,n}(\rho^d, \rho', z^d - z') - \rho' \sin v(t) H_{2,n}(\rho^d, \rho', z^d - z') \right\},$$

$$(58a)$$

$$[Z_n^{\phi t}]_{ij}^{\Phi^d} = -k^2 \int dt \rho f_i(t) \int dt' \rho' \frac{d}{dt'}[\rho' f_j(t')] H_{3,n}(\rho^d, \rho', z^d - z'), \quad (58b)$$

$$[Z_n^{t\phi}]_{ij}^{\Phi^d} = nk^2 \int dt \rho f_i(t) \int dt' \frac{\rho' f_j(t')}{\rho'}$$

$$\cdot \left\{ \left[\rho^d \sin v(t) + (z^d - z') \cos v(t)\right] H_{1,n}(\rho^d, \rho', z^d - z') - \rho' \sin v(t) H_{2,n}(\rho^d, \rho', z^d - z') \right\},$$

$$(58c)$$

and

$$[Z_n^{\phi\phi}]_{ij}^{\Phi^d} = -jnk^2 \int dt \rho f_i(t) \int dt' \rho' f_j(t') H_{3,n}(\rho^d, \rho', z^d - z'). \quad (58d)$$

In (58)

$$H_{1,n}(\rho^d, \rho', z^d - z') = \int_0^\pi H_0(R^d) \cos(n\phi') d\phi', \quad (59a)$$

$$H_{2,n}(\rho^d, \rho', z^d - z') = \int_0^\pi H_0(R^d) \cos(n\phi') \cos\phi' d\phi', \quad (59b)$$

$$H_{3,n}(\rho^d, \rho', z^d - z') = \int_0^\pi H_0(R^d) \sin(n\phi') \sin\phi' d\phi', \quad (59c)$$

where

$$H_0(R^d) = \frac{1 + jkR^d}{(kR^d)^3} \exp(-jkR^d) \quad (59d)$$

and R^d is given by (57).

In view of the fact that we have demonstrated that

$$[Z_{mn}^{pq}]_{ij} = 0, m \neq n \quad (60)$$

28

the set of matrix equations (27) for determining the coefficient vectors $\mathbf{I}_n^t$ and $\mathbf{I}_n^\phi$ reduce to

$$
\begin{bmatrix} [Z_n^{tt}] & [Z_n^{t\phi}] \\ \\ [Z_n^{\phi t}] & [Z_n^{\phi\phi}] \end{bmatrix} \begin{bmatrix} \mathbf{I}_n^t \\ \\ \mathbf{I}_n^\phi \end{bmatrix} = \begin{bmatrix} \mathbf{V}_n^t \\ \\ \mathbf{V}_n^\phi \end{bmatrix}, n = 0, \pm 1, \pm 2, \cdots, \pm N. \tag{61}
$$

It is also easy to see from (30) and (40), (43), (51), and (58) that

$$
[Z_{-n}^{tt}] = [Z_n^{tt}], \tag{62a}
$$

$$
[Z_{-n}^{t\phi}] = -[Z_n^{t\phi}], \tag{62b}
$$

$$
[Z_{-n}^{\phi t}] = -[Z_n^{\phi t}], \tag{62c}
$$

and

$$
[Z_{-n}^{\phi\phi}] = [Z_n^{\phi\phi}]. \tag{62d}
$$

2.5   Expressions for the Elements of the V Vectors

Now that we have obtained detailed expressions for the elements of the Z matrices we turn to the elements of the column vectors $\mathbf{V}_n^t$ and $\mathbf{V}_n^\phi$ in (27) given by (29). Let

$$
V_{ni}^{pq} = \frac{1}{Z_0} \int\limits_S \mathbf{W}_{ni}^p \cdot \mathbf{E}^{inc,q}(\mathbf{r}) dS \tag{63}
$$

where p is either t or ϕ, indicating the unit vectors of the testing functions given by (26), and q is either θ or ϕ, indicating the polarization of the incident electric field given by (11) or (12). The Fourier mode index m has been replaced by n since the original distinction between the Fourier mode index n of the expansion functions for the current and the Fourier mode index m of the testing functions is no longer needed in view of the orthogonality relation (35) which has been used in deriving expressions in Section 2.4 for all the elements of the Z matrices. Since the expressions that will be obtained for V_{ni}^{pq} given by (63) will

29

carry over immediately for $\mathbf{E}^{inc,q}(\mathbf{r}^d)$ needed in (29), there is no need to treat these two cases separately. It is simple to establish the unit vector relations (see the footnote to (33a-d))

$$\hat{\mathbf{t}} \cdot \hat{\boldsymbol{\theta}}^{inc} = \cos\theta^{inc}\sin v(t)\cos(\phi - \phi^{inc}) - \sin\theta^{inc}\cos v(t), \tag{64a}$$

$$\hat{\boldsymbol{\phi}} \cdot \hat{\boldsymbol{\theta}}^{inc} = -\cos\theta^{inc}\sin(\phi - \phi^{inc}), \tag{64b}$$

$$\hat{\mathbf{t}} \cdot \hat{\boldsymbol{\phi}}^{inc} = \sin v(t)\sin(\phi - \phi^{inc}), \tag{64c}$$

and

$$\hat{\boldsymbol{\phi}} \cdot \hat{\boldsymbol{\phi}}^{inc} = \cos(\phi - \phi^{inc}). \tag{64d}$$

Also, using (10),

$$\mathbf{k}^{inc} \cdot \mathbf{r} = -k(\sin\theta^{inc}\hat{\mathbf{x}} + \cos\theta^{inc}\hat{\mathbf{z}}) \cdot (\rho\cos\phi\hat{\mathbf{x}} + \rho\sin\phi\hat{\mathbf{y}} + z\hat{\mathbf{z}})$$

$$= -k\rho\sin\theta^{inc}\cos\phi - kz\cos\theta^{inc}. \tag{65}$$

Hence, recalling that it has been assumed that $\phi^{inc} = 0$,

$$V_{ni}^{t\theta} = k\int dt\rho f_i(t)e^{jkz\cos\theta^{inc}}\left[\cos\theta^{inc}\sin v(t)\int_0^{2\pi}d\phi\cos\phi e^{j(k\rho\sin\theta^{inc}\cos\phi - n\phi)}\right.$$

$$\left. - \sin\theta^{inc}\cos v(t)\int_0^{2\pi}d\phi e^{j(k\rho\sin\theta^{inc}\cos\phi - n\phi)}\right], \tag{66a}$$

$$V_{ni}^{\phi\theta} = -\cos\theta^{inc}k\int dt\rho f_i(t)e^{jkz\cos\theta^{inc}}\int_0^{2\pi}d\phi\sin\phi e^{j(k\rho\sin\theta^{inc}\cos\phi - n\phi)}, \tag{66b}$$

$$V_{ni}^{t\phi} = k\int dt\rho f_i(t)e^{jkz\cos\theta^{inc}}\sin v(t)\int_0^{2\pi}d\phi\sin\phi e^{j(k\rho\sin\theta^{inc}\cos\phi - n\phi)}, \tag{66c}$$

and

$$V_{ni}^{\phi\phi} = k\int dt\rho f_i(t)e^{jkz\cos\theta^{inc}}\int_0^{2\pi}d\phi\cos\phi e^{j(k\rho\sin\theta^{inc}\cos\phi - n\phi)}. \tag{66d}$$

30

Using the integral representation for the Bessel function

$$J_n(x) = \frac{j^{-n}}{2\pi} \int_0^{2\pi} e^{j(x\cos\phi - n\phi)} d\phi \tag{67}$$

it is simple to obtain the integral representations

$$\int_0^{2\pi} \sin\phi \, e^{j(x\cos\phi - n\phi)} d\phi = -\pi j^n [J_{n+1}(x) + J_{n-1}(x)] \tag{68a}$$

and

$$\int_0^{2\pi} \cos\phi \, e^{j(x\cos\phi - n\phi)} d\phi = \pi j^{n+1} [J_{n+1}(x) - J_{n-1}(x)] \tag{68b}$$

so that

$$V_{ni}^{t\theta} = \pi j^{n+1} k \int dt\rho f_i(t) \left[\cos\theta^{inc} \sin v(t)(J_{n+1} - J_{n-1}) + 2j\sin\theta^{inc} \cos v(t) J_n\right] e^{jkz\cos\theta^{inc}},$$
$$\tag{69a}$$

$$V_{ni}^{\phi\theta} = \pi j^n k \int dt\rho f_i(t) \cos\theta^{inc} (J_{n+1} + J_{n-1}) e^{jkz\cos\theta^{inc}}, \tag{69b}$$

$$V_{ni}^{t\phi} = -\pi j^n k \int dt\rho f_i(t) \sin v(t)(J_{n+1} + J_{n-1}) e^{jkz\cos\theta^{inc}}, \tag{69c}$$

and

$$V_{ni}^{\phi\phi} = \pi j^{n+1} k \int dt\rho f_i(t)(J_{n+1} - J_{n-1}) e^{jkz\cos\theta^{inc}}, \tag{69d}$$

where we have let

$$J_n = J_n(k\rho \sin\theta^{inc}). \tag{69e}$$

Using the Bessel function relation

$$J_{-n} = (-1)^n J_n(z) \tag{70}$$

it is easy to show from (69) that

$$V_{-ni}^{t\theta} = V_{ni}^{t\theta}, \tag{71a}$$

31

$$V^{\phi\theta}_{-ni} = -V^{\phi\theta}_{ni}, \tag{71b}$$

$$V^{t\phi}_{-ni} = -V^{t\phi}_{ni}, \tag{71c}$$

and

$$V^{\phi\phi}_{-ni} = V^{\phi\phi}_{ni}. \tag{71d}$$

The expressions corresponding to (69) for V^{pq}_{ni} when $\mathbf{E}^{inc,q}$ in (63) is evaluated at $\mathbf{r}^d(\mathbf{r})$ on the dual surface, needed for calculating (29), are obtained from (69) simply by substituting ρ^d for ρ in (69e) only and z^d for z in (69a-d).

2.6 Calculation of the Current

To calculate the current on the BOR surface we refer to (24) and (25) and write

$$\mathbf{J}^q(t,\phi) = \sum_{n=-N}^{N} e^{jn\phi} \sum_i \left[I^{tq}_{ni} f_i(t)\hat{\mathbf{t}} + I^{\phi q}_{ni} f_i(t)\hat{\boldsymbol{\phi}} \right] \tag{72}$$

where $q = \theta \ (TM)$ or $\phi \ (TE)$ indicates the polarization of the incident electric field given by (11) or (12), and $I^{tq}_{ni}, I^{\phi q}_{ni}$ are the elements of the coefficient vectors $\mathbf{I}^{tq}_n, \mathbf{I}^{\phi q}_n$, obtained as the solution of the matrix equation (61)

$$\begin{bmatrix} [Z^{tt}_n] & [Z^{t\phi}_n] \\ \\ [Z^{\phi t}_n] & [Z^{\phi\phi}_n] \end{bmatrix} \begin{bmatrix} \mathbf{I}^{tq}_n \\ \\ \mathbf{I}^{\phi q}_n \end{bmatrix} = \begin{bmatrix} \mathbf{V}^{tq}_n \\ \\ \mathbf{V}^{\phi q}_n \end{bmatrix}, n = 0, \pm 1, \pm 2, \cdots, \pm N. \tag{73}$$

Letting $\tilde{f} = [f_1(t) f_2(t) \cdots f_N(t)]$ be the row vector of the expansion functions $f_i(t)$ (we use the tilde to indicate the transpose of a column vector), (72) can be written as

$$\mathbf{J}^q(t,\phi) = \sum_{n=-N}^{N} e^{jn\phi} \left[\tilde{f} \mathbf{I}^{tq}_n \hat{\mathbf{t}} + \tilde{f} \mathbf{I}^{\phi q}_n \hat{\boldsymbol{\phi}} \right]. \tag{74}$$

From (73), the relations (62) for the Z_{-n} matrices in terms of the Z_n matrices, and the relations (71) for the V_{-n} vectors in terms of the V_n vectors, it is simple to derive the

32

relations

$$I^{t\theta}_{-n} = I^{t\theta}_n, \tag{75a}$$

$$I^{\phi\theta}_{-n} = -I^{\phi\theta}_n, \tag{75b}$$

$$I^{t\phi}_{-n} = -I^{t\phi}_n, \tag{75c}$$

and

$$I^{\phi\theta}_{-n} = I^{\phi\theta}_n. \tag{75d}$$

(Note that (75b) and (75c) imply that $I^{\phi\theta}_0 = 0$ and $I^{t\phi}_0 = 0$.) Substituting (75) in (74) then yields the expressions for the currents induced on the surface of the BOR by a TM and TE linearly polarized incident plane wave, respectively:

$$\mathbf{J}^\theta(t,\phi) = \tilde{f}I^{t\theta}_0\hat{\mathbf{t}} + 2\sum_{n=1}^N \left[(\tilde{f}I^{t\theta}_n)\cos n\phi\hat{\mathbf{t}} + j(\tilde{f}I^{\phi\theta}_n)\sin n\phi\hat{\boldsymbol{\phi}} \right], \tag{76a}$$

and

$$\mathbf{J}^\phi(t,\phi) = \tilde{f}I^{\phi\phi}_0\hat{\boldsymbol{\phi}} + 2\sum_{n=1}^N \left[(\tilde{f}I^{t\phi}_n)\sin n\phi\hat{\mathbf{t}} + (\tilde{f}I^{\phi\phi}_n)\cos n\phi\hat{\boldsymbol{\phi}} \right]. \tag{76b}$$

2.7 Calculation of the Far Scattered Field

In the far-field region the θ and ϕ components of the scattered electric field can be obtained from the vector potential $\mathbf{A}$ given by (15) [24, p. 281]

$$\mathbf{E}^{sc}(\mathbf{r}) \stackrel{r\to\infty}{\sim} -j\omega\mathbf{A}(\mathbf{r},\mathbf{J}). \tag{77}$$

Then with (15) and (17),

$$E^{sc,pq}(\mathbf{r}) \stackrel{r\to\infty}{\sim} -jkZ_0 \int_S [\mathbf{J}^q(\mathbf{r}') \cdot \hat{\mathbf{p}}] \frac{e^{-jk|\mathbf{r}-\mathbf{r}'|}}{4\pi\,|\,\mathbf{r}-\mathbf{r}'\,|} dS' \tag{78}$$

33

where $p : \theta$ or ϕ, indicates the far scattered field component; $\hat{\mathbf{p}} : \hat{\boldsymbol{\theta}}^{far}$ or $\hat{\boldsymbol{\phi}}^{far}$, is the corresponding unit vector (see Fig. 3); $q : \theta$ or ϕ, indicates the polarization, θ (TM) or ϕ (TE) of the incident electric field; $\mathbf{J}^q$ is given by (74), $\mathbf{r} = (r, \theta^{far}, \phi^{far})$ is the far-field observation point, and $\mathbf{r}' = (\rho', \phi', z')$ is the source point on the BOR surface. In the far field, $|\,\mathbf{r} - \mathbf{r}'\,|$ in the phase of the Green's function can be approximated by

$$|\,\mathbf{r} - \mathbf{r}'\,| \overset{r \to \infty}{\sim} r - \rho' \sin\theta^{far} \cos(\phi' - \phi^{far}) - z' \cos\theta^{far} \tag{79}$$

so that

$$E^{sc,pq}(\mathbf{r}) \overset{r \to \infty}{\sim} -jkZ_0 \frac{e^{-jkr}}{4\pi r} \int_S [\mathbf{J}^q(\mathbf{r}') \cdot \hat{\mathbf{p}}] e^{jk\rho' \sin\theta^{far} \cos(\phi' - \phi^{far})} e^{jkz' \cos\theta^{far}} dS'. \tag{80}$$

The relations (64) can be used directly to obtain

$$\hat{\mathbf{t}}' \cdot \hat{\boldsymbol{\theta}}^{far} = \cos\theta^{far} \sin v(t') \cos(\phi' - \phi^{far}) - \sin\theta^{far} \cos v(t') \tag{81a}$$

$$\hat{\boldsymbol{\phi}}' \cdot \hat{\boldsymbol{\theta}}^{far} = -\cos\theta^{far} \sin(\phi' - \phi^{far}), \tag{81b}$$

$$\hat{\mathbf{t}}' \cdot \hat{\boldsymbol{\phi}}^{far} = \sin v(t') \sin(\phi' - \phi^{far}), \tag{81c}$$

and

$$\hat{\boldsymbol{\phi}}' \cdot \hat{\boldsymbol{\phi}}^{far} = \cos(\phi' - \phi^{far}). \tag{81d}$$

Letting the elements of the vectors $\mathbf{R}_n^{tp}$ and $\mathbf{R}_n^{\phi p}$ be defined by

$$R_{ni}^{tp} = k \int_S f_i(t')(\hat{\mathbf{t}}' \cdot \hat{\mathbf{p}}) e^{jk[\rho' \sin\theta^{far} \cos(\phi' - \phi^{far}) + z' \cos\theta^{far}]} e^{jn(\phi' - \phi^{far})} dS' \tag{82a}$$

and

$$R_{ni}^{\phi p} = k \int_S f_i(t')(\hat{\boldsymbol{\phi}}' \cdot \hat{\mathbf{p}}) e^{jk[\rho' \sin\theta^{far} \cos(\phi' - \phi^{far}) + z' \cos\theta^{far}]} e^{jn(\phi' - \phi^{far})} dS', \tag{82b}$$

34

with $p = \theta$ or ϕ, (80) together with (74) can be written as

$$E^{sc,pq}(\mathbf{r}) \overset{r \to \infty}{\sim} \frac{-jkZ_0 e^{-jkr}}{4\pi kr} \sum_{n=-N}^{N} e^{jn\phi^{far}} \left(\tilde{R}_n^{tp} I_n^{tq} + \tilde{R}_n^{\phi p} I_n^{\phi q} \right) \tag{83}$$

where, using (82) and the 2π periodicity of the ϕ' integration

$$R_{ni}^{t\theta} = k \int dt' \rho' f_i(t') e^{jkz' \cos \theta^{far}} \left[\cos \theta^{far} \sin v(t') \int_0^{2\pi} d\phi' \cos \phi' e^{j(k\rho' \sin \theta^{far} \cos \phi' + n\phi')} \right.$$

$$\left. - \sin \theta^{far} \cos v(t') \int_0^{2\pi} d\phi' e^{j(k\rho' \sin \theta^{far} \cos \phi' + n\phi')} \right], \tag{84a}$$

$$R_{ni}^{\phi\theta} = -\cos \theta^{far} k \int dt' \rho' f_i(t') e^{jkz' \cos \theta^{far}} \int_0^{2\pi} d\phi' \sin \phi' e^{j(k\rho' \sin \theta^{far} \cos \phi' + n\phi')}, \tag{84b}$$

$$R_{ni}^{t\phi} = k \int dt' \rho' f_i(t') e^{jkz' \cos \theta^{far}} \sin v(t') \int_0^{2\pi} d\phi' \sin \phi' e^{j(k\rho' \sin \theta^{far} \cos \phi' + n\phi')}, \tag{84c}$$

and

$$R_{ni}^{\phi\phi} = k \int dt' \rho' f_i(t') e^{jkz' \cos \theta^{far}} \int_0^{2\pi} d\phi' \cos \phi' e^{j(k\rho \sin \theta^{far} \cos \phi' + n\phi')}. \tag{84d}$$

Comparing (84a-d) with (66a-d) we observe that the corresponding expressions are the same if θ^{inc} of (66) is replaced by θ^{far} and $-n$ of (66) is replaced by n. Then (69) and the relations (71) can be used to yield

$$R_{ni}^{t\theta} = \pi j^{n+1} k \int dt' \rho' f_i(t') \left[\cos \theta^{far} \sin v(t')(J_{n+1} - J_{n-1}) + 2j \sin \theta^{far} \cos v(t') J_n \right] e^{jkz' \cos \theta^{far}}, \tag{85a}$$

$$R_{ni}^{\phi\theta} = -\pi j^n k \int dt' \rho' f_i(t') \cos \theta^{far} (J_{n+1} + J_{n-1}) e^{jkz' \cos \theta^{far}}, \tag{85b}$$

$$R_{ni}^{t\phi} = \pi j^n k \int dt' \rho' f_i(t') \sin v(t')(J_{n+1} + J_{n-1}) e^{jkz' \cos \theta^{far}}, \tag{85c}$$

and

$$R_{ni}^{\phi\phi} = \pi j^{n+1} k \int dt' \rho' f_i(t')(J_{n+1} - J_{n-1}) e^{jkz' \cos \theta^{far}}, \tag{85d}$$

where

$$J_n = J_n(k\rho' \sin\theta^{far}).$$

(85e)

The relations (71) apply to the R_{ni}^{pq} as well, so that

$$R_{-ni}^{t\theta} = R_{ni}^{t\theta},$$

(86a)

$$R_{-ni}^{\phi\theta} = -R_{ni}^{\phi\theta},$$

(86b)

$$R_{-ni}^{t\phi} = -R_{ni}^{t\phi},$$

(86c)

and

$$R_{-ni}^{\phi\phi} = R_{ni}^{\phi\phi}.$$

(86d)

Then, substituting (86) and (75) in (83) it is straightforward to obtain

$$E^{sc,\theta\theta}(\mathbf{r}) \overset{r\to\infty}{\sim} -\frac{jkZ_0 e^{-jkr}}{4\pi kr}\left[\tilde{\mathbf{R}}_0^{t\theta}\mathbf{I}_0^{t\theta} + 2\sum_{n=1}^{N}\left(\tilde{\mathbf{R}}_n^{t\theta}\mathbf{I}_n^{t\theta} + \tilde{\mathbf{R}}_n^{\phi\theta}\mathbf{I}_n^{\phi\theta}\right)\cos(n\phi^{far})\right],$$

(87a)

$$E^{sc,\phi\theta}(\mathbf{r}) \overset{r\to\infty}{\sim} \frac{kZ_0 e^{-jkr}}{4\pi kr}2\sum_{n=1}^{N}\left(\tilde{\mathbf{R}}_n^{t\phi}\mathbf{I}_n^{t\theta} + \tilde{\mathbf{R}}_n^{\phi\phi}\mathbf{I}_n^{\phi\theta}\right)\sin(n\phi^{far}),$$

(87b)

$$E^{sc,\theta\phi}(\mathbf{r}) \overset{r\to\infty}{\sim} \frac{kZ_0 e^{-jkr}}{4\pi kr}2\sum_{n=1}^{N}\left(\tilde{\mathbf{R}}_n^{t\theta}\mathbf{I}_n^{t\theta} + \tilde{\mathbf{R}}_n^{\phi\theta}\mathbf{I}_n^{\phi\phi}\right)\sin(n\phi^{far}),$$

(87c)

and

$$E^{sc,\phi\phi}(\mathbf{r}) \overset{r\to\infty}{\sim} -\frac{jkZ_0 e^{-jkr}}{4\pi kr}\left[\tilde{\mathbf{R}}_0^{\phi\phi}\mathbf{I}_0^{\phi\phi} + 2\sum_{n=1}^{N}\left(\tilde{\mathbf{R}}_n^{t\phi}\mathbf{I}_n^{t\phi} + \tilde{\mathbf{R}}_n^{\phi\phi}\mathbf{I}_n^{\phi\phi}\right)\cos(n\phi^{far})\right].$$

(87d)

The radar cross section σ is defined as

$$\sigma^{pq} = \lim_{r\to\infty} 4\pi r^2 \frac{\mid E^{sc,pq}\mid^2}{\mid \mathbf{E}^{inc,q}\mid^2}$$

(88)

where $p : \theta$ or ϕ, denotes the component of the far scattered field, and $q : \theta$ (TM) or ϕ (TE), indicates the polarization of the incident electric field.

36

2.8 Choice of the expansion and testing functions

The detailed expressions we have obtained for the elements of the Z matrices and the V and R vectors all involve the functions $f_i(t)$ that give the t dependence of the expansion and testing functions in (25) and (26). The choice of the $f_i(t)$ has been left open so far and must now be addressed. Following Mautz and Harrington [11] we use a four-impulse approximation to a triangle function developed as follows.

The generating curve of the BOR is parametrized in terms of t, the distance along the curve measured from the lower pole of the BOR. For each value of t, the corresponding point on the generating curve is given by $[\rho(t), z(t)]$. A set of P points $p_1^*, p_2^*, \cdots, p_P^*, P$ odd, $P \geq 5$, is chosen to discretize the generating curve with $p_1^* = (\rho_1^*, z_1^*)$ the lower pole of the generating curve corresponding to $t = 0$, $p_P^* = (\rho_P^*, z_P^*)$ the upper pole of the generating curve, and with $t_i^* > t_{i-1}^*$. The generating curve is approximated by straight line segments between adjacent points. The midpoints of the approximating straight line segments are given by

$$(\rho_i, z_i) = \left(\frac{\rho_i^* + \rho_{i+1}^*}{2}, \frac{z_i^* + z_{i+1}^*}{2} \right), i = 1, 2, \cdots, P - 1 \tag{89}$$

and the length of the ith straight line segment denoted by

$$d_i = \left[\left(\rho_{i+1}^* - \rho_i^* \right)^2 + \left(z_{i+1}^* - z_i^* \right)^2 \right]^{1/2}. \tag{90}$$

For calculation purposes the discretized generating curve then completely replaces the original generating curve and the parameter t now becomes the length along the discretized curve from the lower pole instead of the length along the original generating curve from the lower pole. Thus, for example, $t(p_1^*) = 0$, $t(p_2^*) = d_1$, $t(p_3^*) = d_1 + d_2$, etc. The trigonometric functions $\sin v(t)$ and $\cos v(t)$ appearing in (33), (40), (58), (69), etc., with v the angle mea-

37

sured positive clockwise from the positive z axis to the tangent to the generating curve in the direction of increasing t (see Fig. 5), are then replaced by the discretized values

$$\sin v_i = \frac{\rho_{i+1}^* - \rho_i^*}{d_i} \tag{91a}$$

and

$$\cos v_i = \frac{z_{i+1}^* - z_i^*}{d_i}. \tag{91b}$$

A triangle function $\tau_i(t)$ spanning four segments of the discretized generating curve can be defined as in Fig. 6 where

$$\tau_i(t) = \begin{cases} 0, & t \leq t_{2i-1}^*, t \geq t_{2i+3}^* \\[2mm] \dfrac{t - t_{2i-1}^*}{d_{2i-1} + d_{2i}}, & t_{2i-1}^* \leq t \leq t_{2i+1}^* \\[2mm] \dfrac{t_{2i+3}^* - t}{d_{2i+1} + d_{2i+2}}, & t_{2i+1}^* \leq t \leq t_{2i+3}^* \end{cases} \tag{92}$$

The first triangle function is $\tau_1(t)$ and the last triangle function is $\tau_{(P-3)/2}$. The triangle functions overlap as shown in Fig. 7.

We now let the functions $f_i(t)$ be defined by

$$k\rho f_i(t) = \tau_i(t). \tag{93}$$

Then $\frac{d}{dt}[\rho f_i(t)]$, also required for calculating the elements of the Z matrices and the V and R vectors, is given by

$$\frac{d}{dt}[\rho f_i(t)] = \frac{1}{k}\tau_i'(t) \tag{94}$$

where

$$\tau_i'(t) = \begin{cases} 0, & t \leq t_{2i-1}^*, t \geq t_{2i+3}^* \\[2mm] \dfrac{1}{d_{2i-1} + d_{2i}}, & t_{2i-1}^* \leq t \leq t_{2i+1}^* \\[2mm] -\dfrac{1}{d_{2i+1} + d_{2i+2}}, & t_{2i+1}^* \leq t \leq t_{2i+3}^* \end{cases} \tag{95}$$
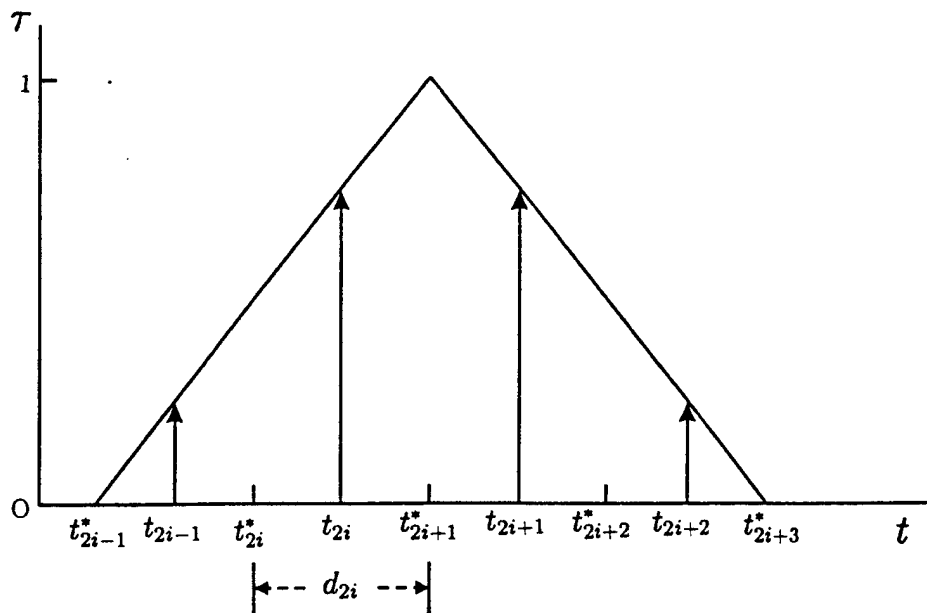
Figure 6. The triangle function $\tau_i(t)$ and the four impulse approximation (arrows).
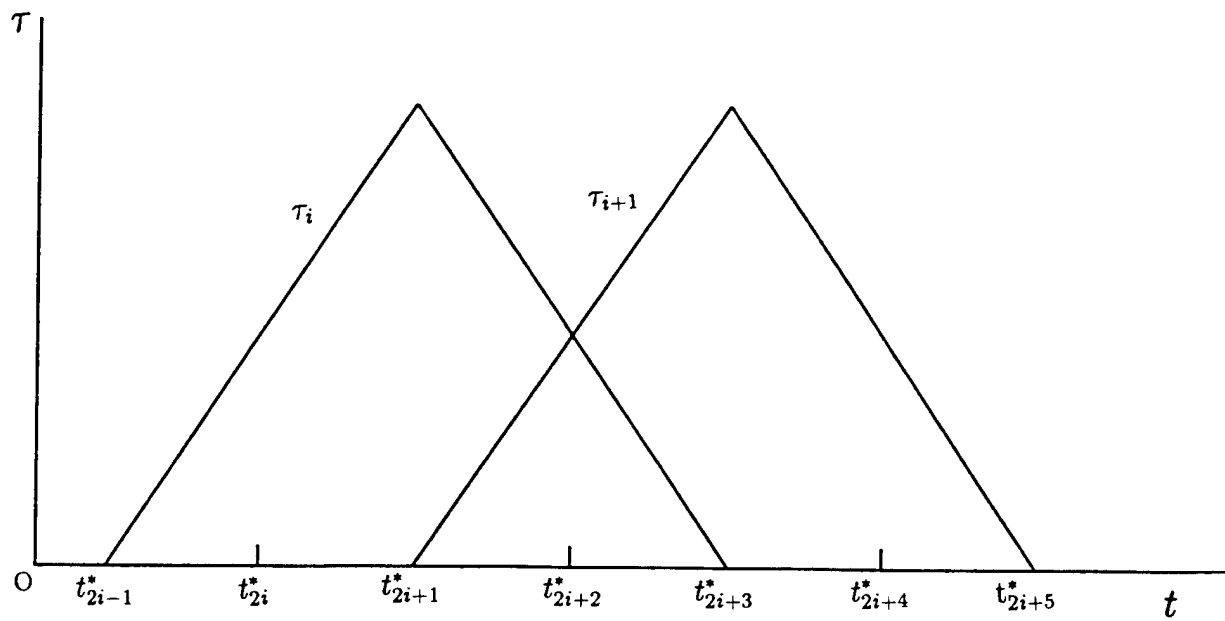
Figure 7. Overlapping of the triangle functions $\tau_i(t)$ and $\tau_{i+1}(t)$.

With the functions $f_i(t)$ chosen as above there still remains the problem of how the t and t' integrations in the expressions for the elements of the Z matrices and the V and R vectors are to be performed, since the use of direct numerical integration to evaluate these expressions is clearly not practical. To perform these integrations we therefore use a four-impulse approximation to $\tau_i(t)$ (see Fig. 6) letting

$$k\rho f_i(t) \approx \sum_{p=1}^{4} T_{p+4i-4}\delta(t - t_{p+2i-2}) \tag{96}$$

where the $T's$ are equal to the value of $\tau(t)$ at the segment midpoints multiplied by the width of the segments:

$$T_{4i-3} = \frac{d_{2i-1}^2}{2(d_{2i-1} + d_{2i})}, \tag{97a}$$

$$T_{4i-2} = \frac{(d_{2i-1} + \frac{1}{2}d_{2i})d_{2i}}{d_{2i-1} + d_{2i}}, \tag{97b}$$

$$T_{4i-1} = \frac{(d_{2i+2} + \frac{1}{2}d_{2i+1})d_{2i+1}}{d_{2i+1} + d_{2i+2}}, \tag{97c}$$

$$T_{4i} = \frac{d_{2i+2}^2}{2(d_{2i+1} + d_{2i+2})}, \tag{97d}$$

and $\delta(x)$ is the Dirac delta function. Similarly, a four-impulse approximation is also employed for the $\frac{d}{dt}[\rho f_i(t)]$ using the derivative of $\tau(t)$ at the segment midpoints multiplied by $1/k$ and the width of the segments. Thus

$$\frac{d}{dt}[\rho f_i(t)] \approx \frac{1}{k}\sum_{p=1}^{4} T'_{p+4i-4}\delta(t - t_{p+2i-2}) \tag{98}$$

where

$$T'_{4i-3} = \frac{d_{2i-1}}{d_{2i-1} + d_{2i}}, \tag{99a}$$

$$T'_{4i-2} = \frac{d_{2i}}{d_{2i-1} + d_{2i}}, \tag{99b}$$

$$T'_{4i-1} = -\frac{d_{2i+1}}{d_{2i+1} + d_{2i+2}}, \tag{99c}$$

41

and

$$T'_{4i} = -\frac{d_{2i+2}}{d_{2i+1} + d_{2i+2}}. \tag{99d}$$

As an example of the implementation of the four-impulse triangle function approximation, let us take (40d)

$$[Z_n^{\phi\phi}]_{ij}^{\mathbf{A}} = jk^2 \int dt \rho f_i(t) \int dt' \rho' f_j(t') G_{2,n}(\rho, \rho', z - z') \tag{100}$$

with $G_{2,n}(\rho, \rho', z - z)$ given by (41b). Substitution of (96) in (100) then gives

$$[Z_n^{\phi\phi}]_{ij}^{\mathbf{A}} = j \sum_{p=1}^{4} \sum_{q=1}^{4} T_{p'} T_{q'} G_{2,n}(\rho_{i'}, \rho_{j'}, z_{i'} - z_{j'}) \tag{101}$$

where

$$p' = p + 4i - 4, \tag{102a}$$

$$q' = q + 4j - 4, \tag{102b}$$

$$i' = p + 2i - 2, \tag{102c}$$

and

$$j' = q + 2j - 2. \tag{102d}$$

In the integral (41b) that defines $G_{2,n}$, R is given by

$$R = \left[(\rho_{i'} - \rho_{j'})^2 + (z_{i'} - z_{j'})^2 + 4\rho_{i'}\rho_{j'} \sin^2\left(\frac{\phi'}{2}\right) \right]^{1/2}. \tag{103}$$

In (103), $(\rho_{i'}, z_{i'})$ and $(\rho_{j'}, z_{j'})$ are the respective midpoints of the i'^{th} and j'^{th} segments of the discretized generating curve.

Once the integrations over t and t' have been replaced by summations as in (101), we introduce the following changes in the summation indexing in preparation for the increase

42

in efficiency of the resulting calculations discussed in Section 2.9. First, let the summations be represented schematically in general as

$$Q_{ij} = \sum_{p=1}^{4} \sum_{q=1}^{4} T_{p'} T_{q'} F(i', j') \tag{104}$$

where Q_{ij} is the quantity to be evaluated, $F(i', j')$ is the summand apart from the triangle functions, and p', q', i', j' are given by (102). (Although we have used T given by (97) in (104), either or both of $T_{p'}$ and $T_{q'}$ can be replaced by a derivative $T'_{p'}$ or $T'_{q'}$ given by (99) without in any way affecting the argument.) Next, we change the indices so that the summations are over the indices of F by letting

$$r = i' = p + 2i - 2 \tag{105a}$$

$$s = j' = q + 2j - 2 \tag{105b}$$

so that

$$p = r - 2i + 2 \tag{106a}$$

$$q = s - 2j + 2 \tag{106b}$$

and

$$p' = r + 2i - 2 \tag{107a}$$

$$q' = s + 2j - 2. \tag{107b}$$

Then successive values of p from 1 to 4 correspond to successive values of r from $2i - 1$ to $2i + 2$, and successive values of q from 1 to 4 correspond to successive values of s from $2j - 1$ to $2j + 2$, and

$$Q_{ij} = \sum_{r=2i-1}^{2i+2} \sum_{s=2j-1}^{2j+2} T_{r'} T_{s'} F(r, s) \tag{108}$$

43

where

$$r' = r + 2i - 2 \tag{109a}$$

and

$$s' = s + 2j - 2. \tag{109b}$$

Finally, we change i, j to p, q; r, s to i, j; and r', s' to i', j' so that (108) becomes

$$Q_{pq} = \sum_{i=2p-1}^{2p+2} \sum_{j=2q-1}^{2q+2} T_{i'} T_{j'} F(i, j) \tag{110}$$

where

$$i' = i + 2p - 2 \tag{111a}$$

and

$$j' = j + 2q - 2. \tag{111b}$$

Substituting the expressions (96) and (98) for the expansion functions and their derivatives in (40),(43),(51), and (58), and performing the change in summation indexing of (104)-(111), the elements of the Z matrices now become the following:

$$[Z_n^{tt}]_{pq}^{\mathbf{A}} = j \sum_{i=2p-1}^{2p+2} \sum_{j=2q-1}^{2q+2} T_{i'} T_{j'} \left[\sin v_i \sin v_j G_{2,n}(\rho_i, \rho_j, z_i - z_j) + \cos v_i \cos v_j G_{1,n}(\rho_i, \rho_j, z_i - z_j) \right],$$
$$\tag{112a}$$

$$[Z_n^{\phi t}]_{pq}^{\mathbf{A}} = - \sum_{i=2p-1}^{2p+2} \sum_{j=2q-1}^{2q+2} T_{i'} T_{j'} \sin v_j G_{3,n}(\rho_i, \rho_j, z_i - z_j), \tag{112b}$$

$$[Z_n^{t\phi}]_{ij}^{\mathbf{A}} = \sum_{i=2p-1}^{2p+2} \sum_{j=2q-1}^{2q+2} T_{i'} T_{j'} \sin v_i G_{3,n}(\rho_i, \rho_j, z_i - z_j), \tag{112c}$$

and

$$[Z_n^{\phi\phi}]_{pq}^{\mathbf{A}} = j \sum_{i=2p-1}^{2p+2} \sum_{j=2q-1}^{2q+2} T_{i'} T_{j'} G_{2,n}(\rho_i, \rho_j, z_i - z_j); \tag{112d}$$

44

$$[Z_n^{tt}]_{pq}^{\mathbf{A}^d} = j \sum_{i=2p-1}^{2p+2} \sum_{j=2q-1}^{2q+2} T_{i'} T_{j'} \left[\sin v_i \sin v_j G_{2,n}(\rho_i^d, \rho_j, z_i^d - z_j) + \cos v_i \cos v_j G_{1,n}(\rho_i^d, \rho_j, z_i^d - z_j) \right],$$

$$(113a)$$

$$[Z_n^{\phi t}]_{pq}^{\mathbf{A}^d} = - \sum_{i=2p-1}^{2p+2} \sum_{j=2q-1}^{2q+2} T_{i'} T_{j'} \sin v_j G_{3,n}(\rho_i^d, \rho_j, z_i^d - z_j), \qquad (113b)$$

$$[Z_n^{t\phi}]_{ij}^{\mathbf{A}^d} = \sum_{i=2p-1}^{2p+2} \sum_{j=2q-1}^{2q+2} T_{i'} T_{j'} \sin v_i G_{3,n}(\rho_i^d, \rho_j, z_i^d - z_j), \qquad (113c)$$

and

$$[Z_n^{\phi\phi}]_{pq}^{\mathbf{A}^d} = j \sum_{i=2p-1}^{2p+2} \sum_{j=2q-1}^{2q+2} T_{i'} T_{j'} G_{2,n}(\rho_i^d, \rho_j, z_i^d - z_j); \qquad (113d)$$

$$[Z_n^{tt}]_{pq}^{\Phi} = -\frac{j}{k^2} \sum_{i=2p-1}^{2p+2} \sum_{j=2q-1}^{2q+2} T_{i'}' T_{j'}' G_{1,n}(\rho_i, \rho_j, z_i - z_j), \qquad (114a)$$

$$[Z_n^{\phi t}]_{pq}^{\Phi} = -\frac{n}{k^2} \sum_{i=2p-1}^{2p+2} \sum_{j=2q-1}^{2q+2} \frac{T_{i'} T_{j'}'}{\rho_i} G_{1,n}(\rho_i, \rho_j, z_i - z_j), \qquad (114b)$$

$$[Z_n^{t\phi}]_{pq}^{\Phi} = \frac{n}{k^2} \sum_{i=2p-1}^{2p+2} \sum_{j=2q-1}^{2q+2} \frac{T_{i'}' T_{j'}}{\rho_j} G_{1,n}(\rho_i, \rho_j, z_i - z_j), \qquad (114c)$$

and

$$[Z_n^{\phi\phi}]_{pq}^{\Phi} = -j\frac{n^2}{k^2} \sum_{i=2p-1}^{2p+2} \sum_{j=2q-1}^{2q+2} \frac{T_{i'} T_{j'}}{\rho_i \rho_j} G_{1,n}(\rho_i, \rho_j, z_i - z_j); \qquad (114d)$$

$$[Z_n^{tt}]_{pq}^{\Phi^d} = -j \sum_{i=2p-1}^{2p+2} \sum_{j=2q-1}^{2q+2} T_{i'} T_{j'}'$$
$$\cdot \left\{ \left[\rho_i^d \sin v_i + (z_i^d - z_j) \cos v_i \right] H_{1,n}(\rho_i^d, \rho_j, z_i^d - z_j) - \rho_j \sin v_i H_{2,n}(\rho_i^d, \rho_j, z_i^d - z_j) \right\}$$

$$(115a)$$

$$[Z_n^{\phi t}]_{pq}^{\Phi^d} = - \sum_{i=2p-1}^{2p+2} \sum_{j=2q-1}^{2q+2} T_{i'} T_{j'}' \rho_j H_{3,n}(\rho_i^d, \rho_j, z_i^d - z_j), \qquad (115b)$$

$$[Z_n^{t\phi}]_{pq}^{\Phi^d} = n \sum_{i=2p-1}^{2p+2} \sum_{j=2q-1}^{2q+2} \frac{T_{i'} T_{j'}}{\rho_j}$$
$$\cdot \left\{ \left[\rho_i^d \sin v_i + (z_i^d - z_j) \cos v_i \right] H_{1,n}(\rho_i^d, \rho_j, z_i^d - z_j) - \rho_j \sin v_i H_{2,n}(\rho_i^d, \rho_j, z_i^d - z_j) \right\},$$

$$(115c)$$

45

and

$$[Z_n^{\phi\phi}]_{pq}^{\Phi d} = -jn \sum_{i=2p-1}^{2p+2} \sum_{j=2q-1}^{2q+2} T_{i'}T_{j'}H_{3,n}(\rho_i^d, \rho_j, z_i^d - z_j). \tag{115d}$$

In the integrals (41a-c) and (59a-c) that define the $G_{k,n}$ and $H_{k,n}, k = 1, 2, 3$ in (112) to 115),

from (38) and (42)

$$R_{ij} = \left[(\rho_i - \rho_j)^2 + (z_i - z_j)^2 + 4\rho_i\rho_j \sin^2(\frac{\phi'}{2})\right]^{1/2}. \tag{116}$$

and

$$R_{ij}^d = \left[(\rho_i^d - \rho_j)^2 + (z_i^d - z_j)^2 + 4\rho_i^d\rho_j \sin^2(\frac{\phi'}{2})\right]^{1/2}. \tag{117}$$

The two superscripts of the $Z's$, t or ϕ, indicate the unit vectors of the testing functions

and expansion functions, respectively (see (26) and (25)). When $i = j$, we see from (116)

that $R_{ij} = 0$ when $\phi' = 0$ so that the integrals defining the $G_{k,n}$ become singular. Hence, for

$i = j$, R_{ij} is approximated by an equivalent distance [11]

$$R_{ij} = \left[(d_i/4)^2 + 4\rho_i^2 \sin^2(\frac{\phi'}{2})\right]^{1/2}, i = j. \tag{118}$$

Since R_{ij}^d never equals zero no special treatment using an equivalent distance is needed.

Next, substituting the four-impulse triangle function representation (96) of the expansion

functions in (69) followed by the change in indices, we obtain the following expressions for

the elements of the V vectors:

$$V_{np}^{t\theta} = \pi j^{n+1} \sum_{i=2p-1}^{2p+2} T_{i'} \left[\cos\theta^{inc}\sin v_i(J_{n+1} - J_{n-1}) + 2j\sin\theta^{inc}\cos v_i J_n\right] e^{jkz_i \cos\theta^{inc}}, \tag{119a}$$

$$V_{np}^{\phi\theta} = \pi j^n \sum_{i=2p-1}^{2p+2} T_{i'} \cos\theta^{inc}(J_{n+1} + J_{n-1})e^{jkz_i \cos\theta^{inc}}, \tag{119b}$$

$$V_{np}^{t\phi} = -\pi j^n \sum_{i=2p-1}^{2p+2} T_{i'} \sin v_i(J_{n+1} + J_{n-1})e^{jkz_i \cos\theta^{inc}}, \tag{119c}$$

46

and

$$V_{np}^{\phi\phi} = \pi j^{n+1} \sum_{i=2p-1}^{2p+2} T_{i'}(J_{n+1} - J_{n-1})e^{jkz_i \cos\theta^{inc}}, \qquad (119d)$$

where

$$J_n \equiv J_n(k\rho_i \sin\theta^{inc}). \qquad (119e)$$

In (119a-d) the two superscripts of the $V's$ indicate respectively the unit vectors of the testing functions given by (26) and the polarization of the incident electric field given by (11) and (12).

Similarly, substituting (96) in (85) followed by the change in indices, we obtain

$$R_{np}^{t\theta} = \pi j^{n+1} \sum_{i=2p-1}^{2p+2} T_{i'} \left[\cos\theta^{far} \sin v_i (J_{n+1} - J_{n-1}) + 2j \sin\theta^{far} \cos v_i J_n\right] e^{jkz_i \cos\theta^{far}}, \quad (120a)$$

$$R_{np}^{\phi\theta} = -\pi j^n \sum_{i=2p-1}^{2p+2} T_{i'} \cos\theta^{far}(J_{n+1} + J_{n-1})e^{jkz_i \cos\theta^{far}}, \qquad (120b)$$

$$R_{np}^{t\phi} = \pi j^n \sum_{i=2p-1}^{2p+2} T_{i'} \sin v_i (J_{n+1} + J_{n-1})e^{jkz_i \cos\theta^{far}}, \qquad (120c)$$

and

$$R_{np}^{\phi\phi} = \pi j^{n+1} \sum_{i=2p-1}^{2p+2} T_{i'}(J_{n+1} - J_{n-1})e^{jkz_i \cos\theta^{far}}, \qquad (120d)$$

where

$$J_n \equiv J_n(k\rho_i \sin\theta^{far}). \qquad (120e)$$

In (120a-d) the two superscripts of the $R's$ indicate the far scattered electric field component and the polarization of the incident electric field, respectively.

An alternative choice of the expansion and testing functions, closely related to that of Mautz and Harrington which we have used, is to let the functions $f_i(t)$ be given by

$$f_i(t) = \tau_i(t) \qquad (121)$$

47

instead of by (93), with $\tau_i(t)$ given by (92) as before. Then

$$\frac{d}{dt}[\rho(t)f_i(t))] = \rho(t)\tau_i'(t) + \rho'(t)\tau(t) \tag{122}$$

where $\tau_i'(t)$ is given as before by (95). Again, using the four-impulse approximation to perform the t and t' integrations, (96) is replaced by

$$k\rho f_i(t) \approx \sum_{p=1}^{4} \mathcal{T}_{p+4i-4}\delta(t - t_{p+2i-2}) \tag{123}$$

and (98) is replaced by

$$\frac{d}{dt}[\rho f_i(t)] \approx \frac{1}{k}\sum_{p=1}^{4} \mathcal{T}'_{p+4i-4}\delta(t - t_{p+2i-2}) \tag{124}$$

with

$$\mathcal{T}_{p+4i-4} = k\rho_{p+2i-2}T_{p+4i-4}, \quad p = 1,\cdots,4 \tag{125}$$

and

$$\mathcal{T}'_{p+4i-4} = k\rho_{p+2i-2}T'_{p+4i-4} + k\sin v_{p+2i-2}T_{p+4i-4}, \quad p = 1,\cdots,4. \tag{126}$$

In (125) and (126) T_{p+4i-4} and T'_{p+4i-4} are given by (97) and (99) respectively. The expressions (112)-(120) for the elements of the Z matrices and the V and R vectors can then be used exactly as they are simply by substituting $\mathcal{T}$ for T and $\mathcal{T}'$ for T'.[6] It is shown in Section 3.6 that the alternative choice of the $f_i(t)$, (121), must be used instead of (93) if half-triangle functions are to be used at the beginning and end of the discretized generating curve of the BOR.

---

[6]This efficient method of implementing the alternative choice of the functions $f_i(t)$ is due to John Putnam [25].

2.9 Increasing the Efficiency of the Computations

Referring back to the general form of the computations, (110), we observe that the $T's$ are trivial to calculate and store, once and for all, at the outset of a calculation of the far scattered field pattern for a BOR, whereas in contrast the $F's$ are time consuming to calculate. Furthermore we observe that in (110) the same $F(i,j)$ will contribute to the calculation of several Q_{pq}. Hence, rather than using (110) to calculate Q_{pq}, it is desirable to have the limits of the summations go from one to the number of segments in the discretized generating curve of the BOR so that there is no repetition of the calculation of $F(i,j)$. The basic question to be answered, then, is given i and j what are the values of p and q for which $F(i,j)$ contributes to Q_{pq}? An example will help to clarify this question. Suppose $i = 5$ and $j = 6$. Then we can make the following tabulation

p	$2p-1$	$2p$	$2p+1$	$2p+2$	q	$2q-1$	$2q$	$2q+1$	$2q+2$
1	1	2	3	4	1	1	2	3	4
2	3	4	5	6	2	3	4	5	6
3	5	6	7	8	3	5	6	7	8
4	7	8	9	10	4	7	8	9	10

and observe that $F(5,6)$ contributes to Q_{pq} when p is either 2 or 3 and q is either 2 or 3, so that $F(5,6)$ contributes to four different Q_{pq}. In general it is clear from the limits of the summations in (110) that if i is odd then $p = (i-1)/2$ and $p = (i+1)/2$ whereas if i is even then $p = (i-2)/2$ and $i/2$, and similarly for j and q. Of course, when i or j equals 1 then only one of the two values of p or q is a valid index for Q_{pq} and similarly when i or j is equal to the number of segments in the discretized generating curve.

2.10 Choice of the Number of Fourier Modes for Expansion and Testing Functions.

The ϕ dependence of the current given by (24) is expressed as a summation from $-N$ to N of the Fourier modes $e^{jn\phi}$. The value of N can be set equal to the number of Fourier modes sufficient to represent, to the desired accuracy, the ϕ variation of the tangential component of the incident electric field on the surface of the BOR. Let a be the largest value of ρ of a point (ρ, z) on the generating curve of the BOR. Then from (10), (11), and (12) it can be seen that the ϕ variation of the incident field along the circle on the BOR corresponding to the point (a, z) is given by

$$f(\phi) = \cos \phi e^{jka \sin \theta^{inc} \cos \phi} \ \text{ or } \ f(\phi) = \sin \phi e^{jka \sin \theta^{inc} \cos \phi}. \tag{127}$$

For axial incidence $\theta^{inc} = 0$ and $f(\phi)$ equals $\cos \phi$ or $\sin \phi$ so that only the $e^{\pm j\phi}$ modes are needed. For oblique incidence, we can express $f(\phi)$ as the Fourier series

$$f(\phi) = \sum_{-N}^{N} c_n e^{jn\phi} \tag{128a}$$

with

$$c_n = \frac{1}{2\pi} \int_0^{2\pi} f(\phi) e^{-jn\phi} d\phi \tag{128b}$$

from which, with (127) and (68a,b),

$$\mid c_n \mid = \frac{1}{2} \left[J_{n+1}(ka \sin \theta^{inc}) \pm J_{n-1}(ka \sin \theta^{inc}) \right]. \tag{129}$$

As n increases beyond $ka \sin \theta^{inc}$, $\mid J_n(ka \sin \theta^{inc}) \mid$ decreases rapidly and it suffices to choose

$$N = I + M \tag{130}$$

50

where

$$I = \text{Int}[ka \sin \theta^{inc}] \tag{131}$$

and M is the smallest integer for which

$$\frac{J_N(ka \sin \theta^{inc})}{J_I(ka \sin \theta^{inc})} \leq \epsilon \tag{132}$$

with ϵ a small number depending on the desired accuracy. If the value of N given by (130) is plotted as a function of $\text{Int}[ka \sin \theta^{inc}]$ the plot is found to be almost linear. For $\epsilon = 0.005$, for example,

$$N \approx \text{Int}[1.04 ka \sin \theta^{inc}] + 7. \tag{133}$$

A similar expression

$$N \approx \text{Int}[k^+(a \sin \theta) + \lambda] \tag{134}$$

with k^+ denoting a value a few percent larger than k was obtained by Yaghjian [26] for the reciprocal problem of estimating the number of angular modes needed to represent the far field of a radiator in the θ direction.

3 RESULTS

The analysis presented in Section 2 was implemented in a FORTRAN computer program which was then used to obtain numerical results for several different BOR's. These results will now be described and discussed.

3.1 Spurious Resonances for a PEC Sphere

As noted in the Introduction, the ordinary EFIE does not have a unique solution to the exterior scattering problem at frequencies equal to the resonant frequencies of the corresponding interior cavity. Consequently, numerical results obtained by solving the EFIE can have significant errors called spurious resonances when the electrical dimensions of the scattering object are such as to make the interior cavity resonant. The DSEFIE by contrast has a unique solution to the exterior scattering problem at all frequencies. For a sphere, the cavity problem has been treated by Harrington [27] who shows that the condition for resonance is $ka = u_{np}$ for TE modes and $ka = u'_{np}$ for TM modes where u_{np} is the pth zero of the Bessel function $J_{n+1/2}(x)$ and u'_{np} is the pth zero of $[x^{1/2}J_{n+1/2}]'(x)$.

As an example of how the DSEFIE eliminates spurious resonances that may occur in solving the EFIE, in Fig. 8 we show the backscatter RCS of a PEC sphere as a function of ka in the vicinity of the resonant value of $ka = 6.062$, the first zero of $[x^{1/2}J_{9/2}]'(x)$. It is clearly seen that the spurious resonance displayed by the EFIE curve at 6.08 is eliminated by the DSEFIE curve which agrees closely with the exact Mie solution curve.

3.2 Spurious Resonance for a PEC Prolate Spheroid

As a second example of the DSEFIE removal of a spurious resonance obtained using the EFIE, in Fig. 9 we show the E_θ bistatic RCS pattern in the $\phi = 90°$ plane of a prolate spheroid illuminated by a TM plane wave. The geometry of the spheroid is shown in Fig. 10. The propagation vector of the incident plane wave lies in the xz plane making an angle of $\theta^{inc} = 45°$ with the z axis, and the semi-major and semi-minor axes of the spheroid are
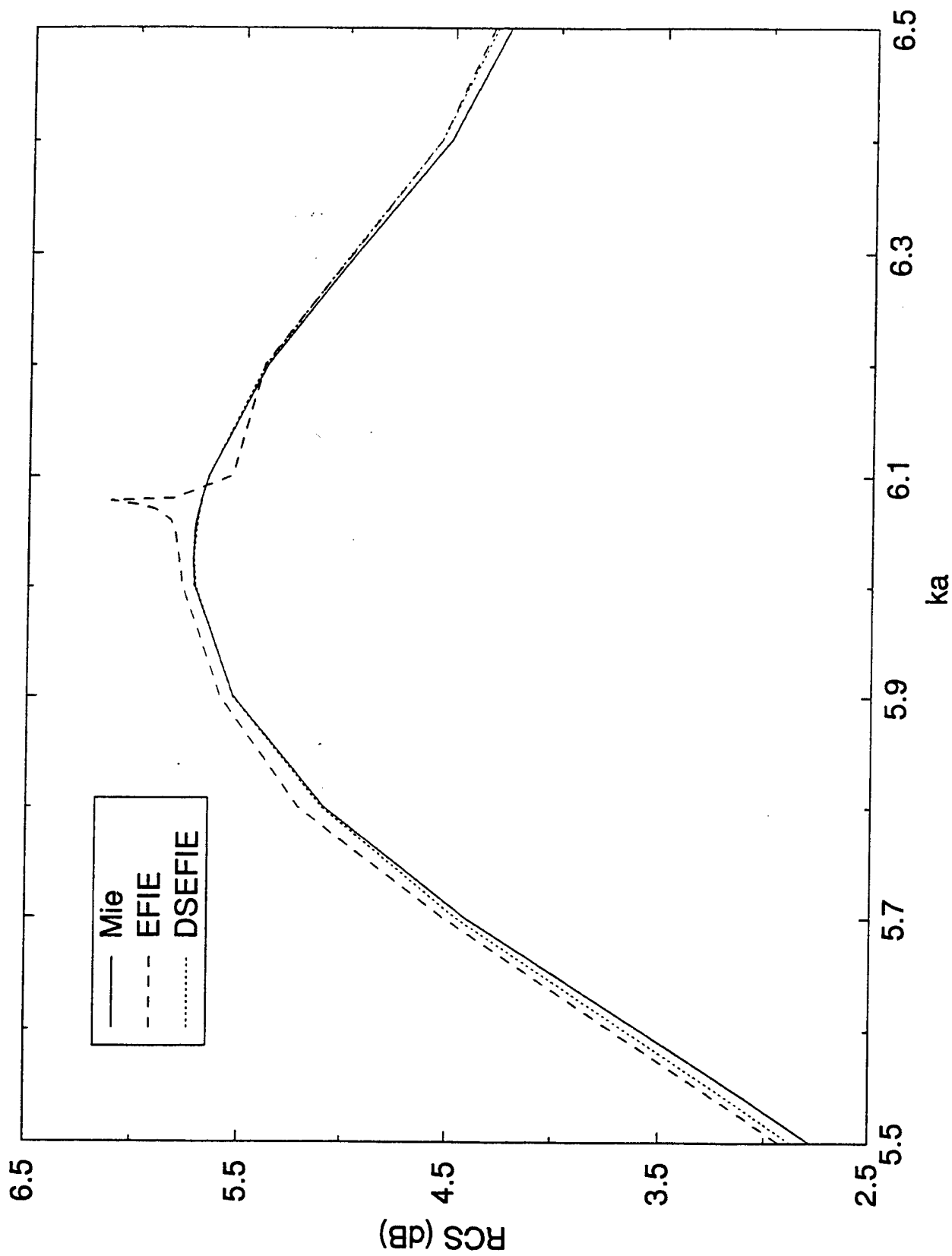
Figure 8. Back scatter RCS of a perfectly conducting sphere as a function of ka calculated by the exact Mie series, the conventional EFIE, and the DSEFIE. The spurious resonance in the EFIE curve at $ka = 6.08$ is eliminated by the DSEFIE.
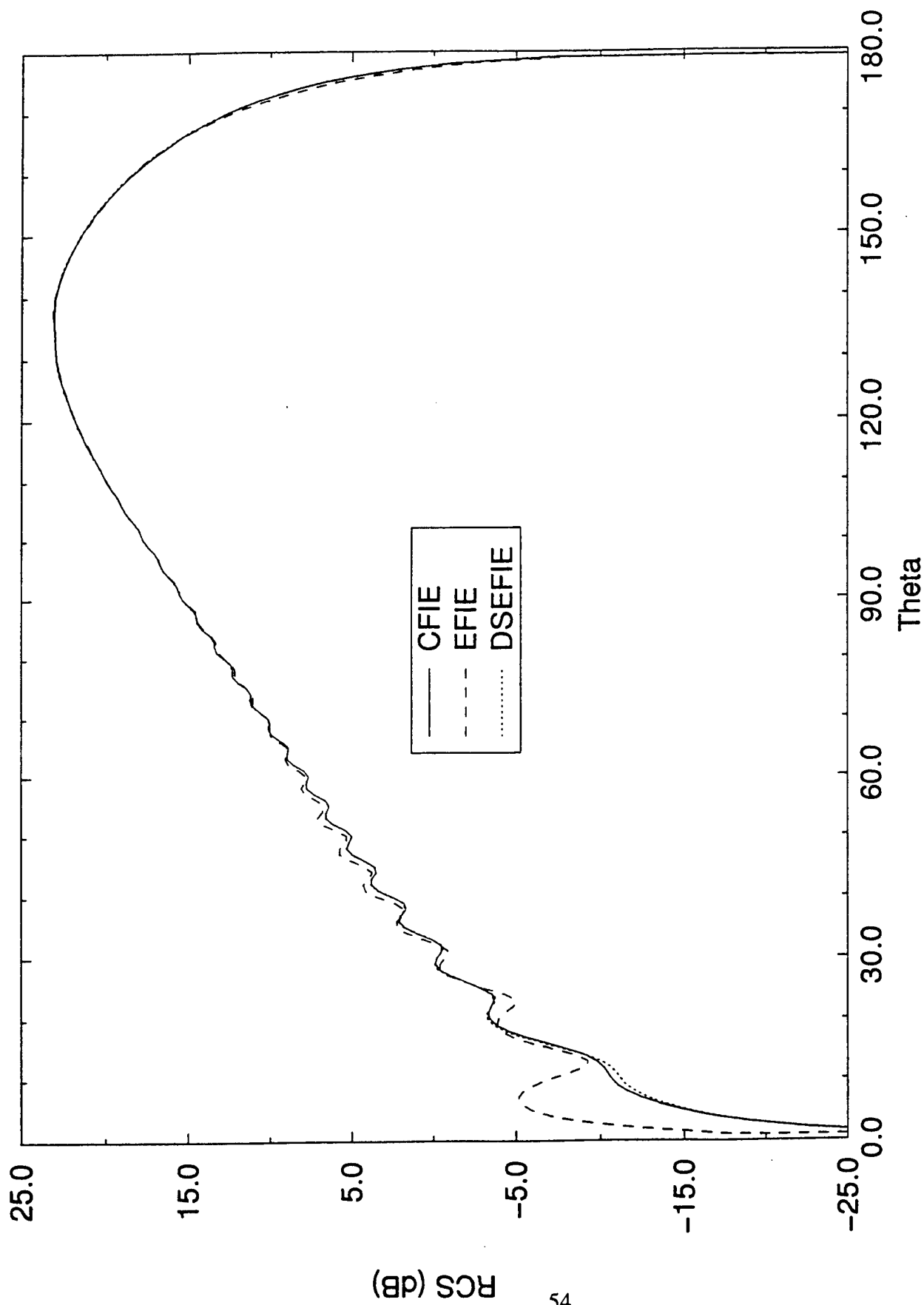
Figure 9. Prolate spheroid E_θ bistatic RCS in the $\phi = 90°$ plane for TM oblique incidence at $45°$; $ka = 50$, $kb = 25$. The spurious resonance in the EFIE curve for $\theta < 10°$ is eliminated by the DSEFIE and CFIE.
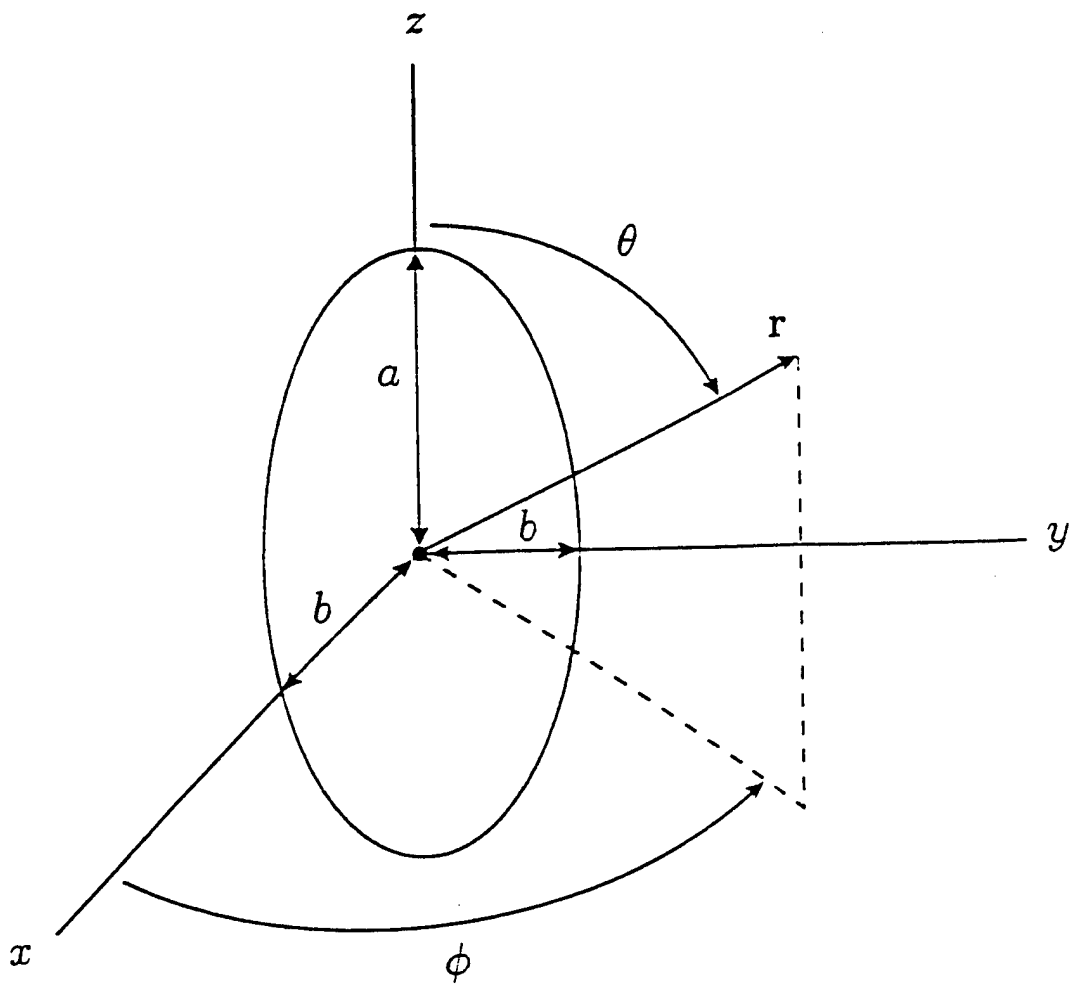
Figure 10. Geometry of the prolate spheroid.

given by $ka = 50$ and $kb = 25$, respectively. The large error displayed by the EFIE pattern

for $\theta < 10°$ is eliminated in the pattern obtained using the DSEFIE computer program and in

the pattern obtained with the combined-field BOR integral equation program CICERO [21]

shown for reference. The discrete nature of the spurious resonance can be seen by comparing

Fig. 9 with Fig. 11 which shows the corresponding bistatic RCS patterns for a spheroid

with $ka = 49.8$ and $kb = 24.9$. In Fig. 11 the EFIE pattern has no spurious resonance.

3.3 Spurious Resonances for a PEC Finite Cylinder

Calculations of scattering from a finite cylinder provide another example of the elimination of

spurious resonances by the DSEFIE. Expressions for the resonant frequencies of a cylindrical

cavity are derived in [28]. In particular, the resonant frequency for the dominant TE mode,

TE_{111}, is given by

$$\omega_{111} = \frac{1.841}{\sqrt{\mu_0 \epsilon_0} R} \left(1 + 2.912 \frac{R^2}{d^2} \right)^{1/2} \tag{135}$$

where R and d are the radius and height, respectively, of the cylinder. Since $\omega\sqrt{\mu_0\epsilon_0} = k =$

$2\pi/\lambda$, for $R = d$ and $\lambda = 1$ the radius and height of the cylinder that supports the TE_{111}

mode is $R = d = 1.841(3.912)^{1/2}/(2\pi) = 0.580$. Figure 12 shows the monostatic E-plane

RCS pattern for R = d = .587 as obtained by the EFIE, the CFIE, and the DSEFIE, with a

discretization of the generating curve for the finite cylinder using 20 points/λ. The striking

spurious resonance displayed by the EFIE pattern is removed by both the CFIE and DSEFIE

which are in close agreement with each other. In contrast, the EFIE, CFIE, and DSEFIE

monostatic patterns for the non-resonant cylinder $R = d = .52$ are shown in Fig. 13. For

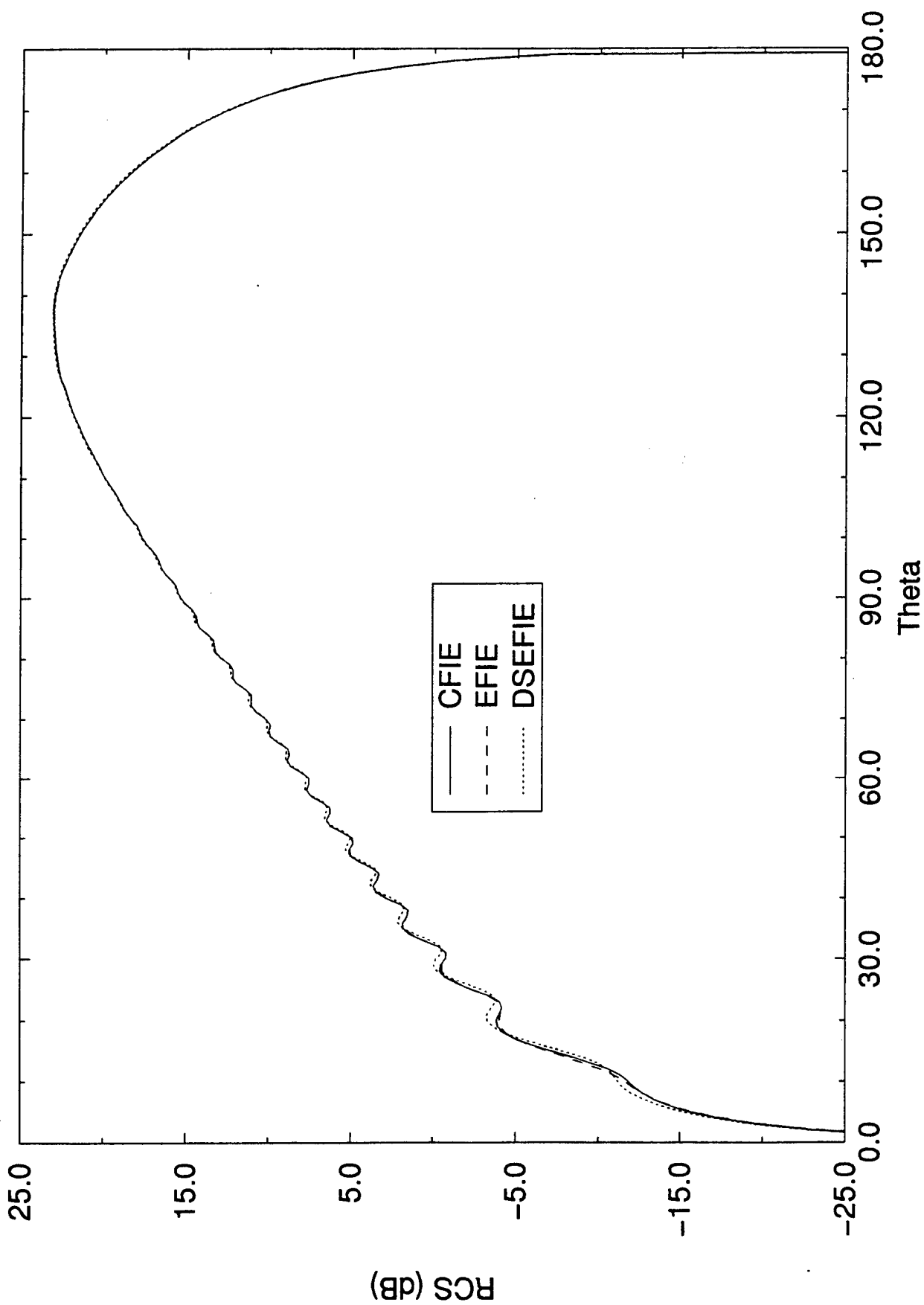this cylinder there is no spurious resonance in the EFIE pattern. Figure 14 shows the EFIE,

Figure 11. Prolate spheroid E_θ bistatic RCS in the $\phi = 90°$ plane for TM oblique incidence at 45°; $ka = 49.8, kb = 24.9$.
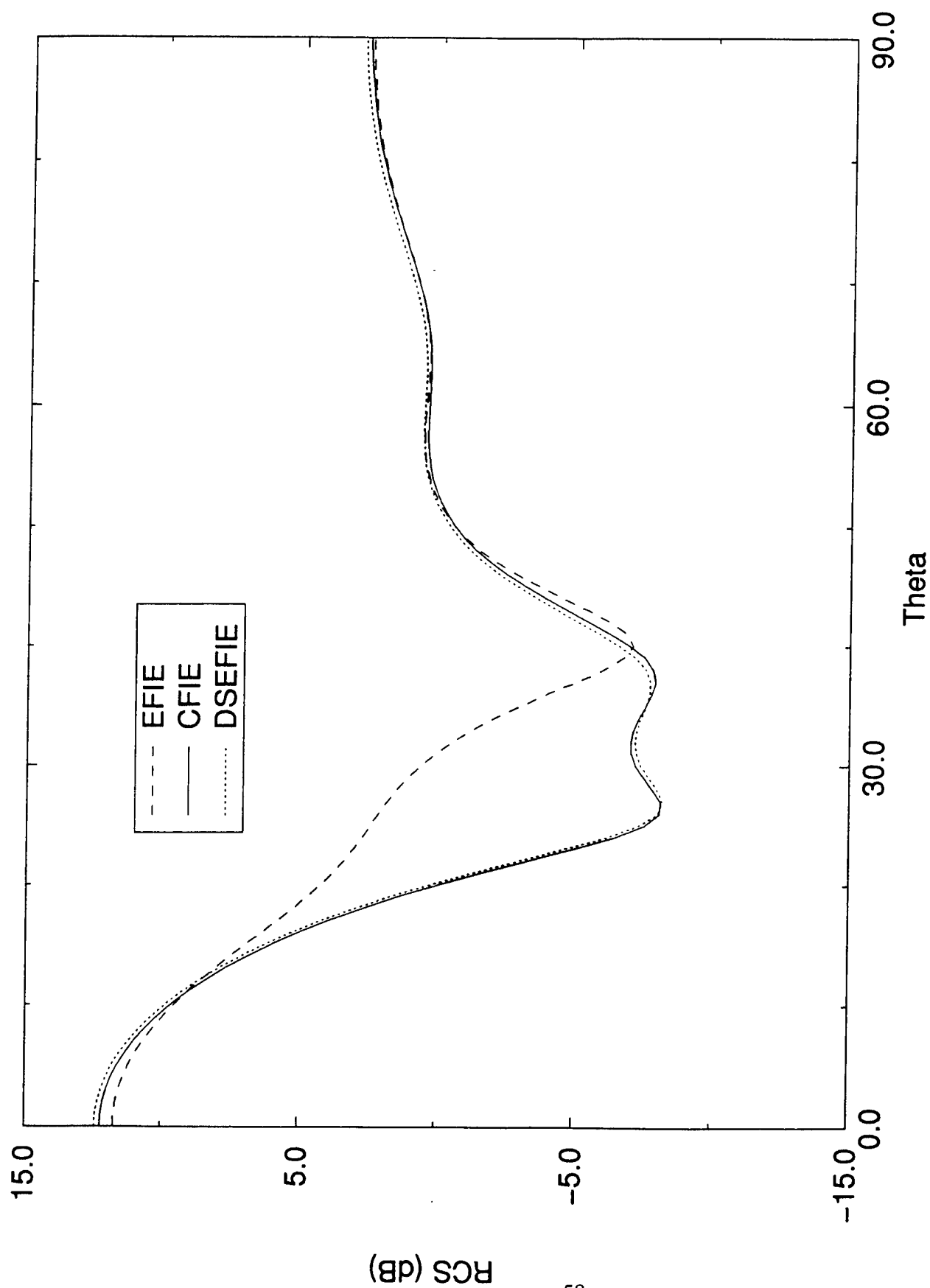
Figure 12. Monostatic E-plane RCS patterns for the resonant finite cylinder $R = d = .587$. The spurious resonance in the EFIE pattern is removed by the DSEFIE and CFIE.
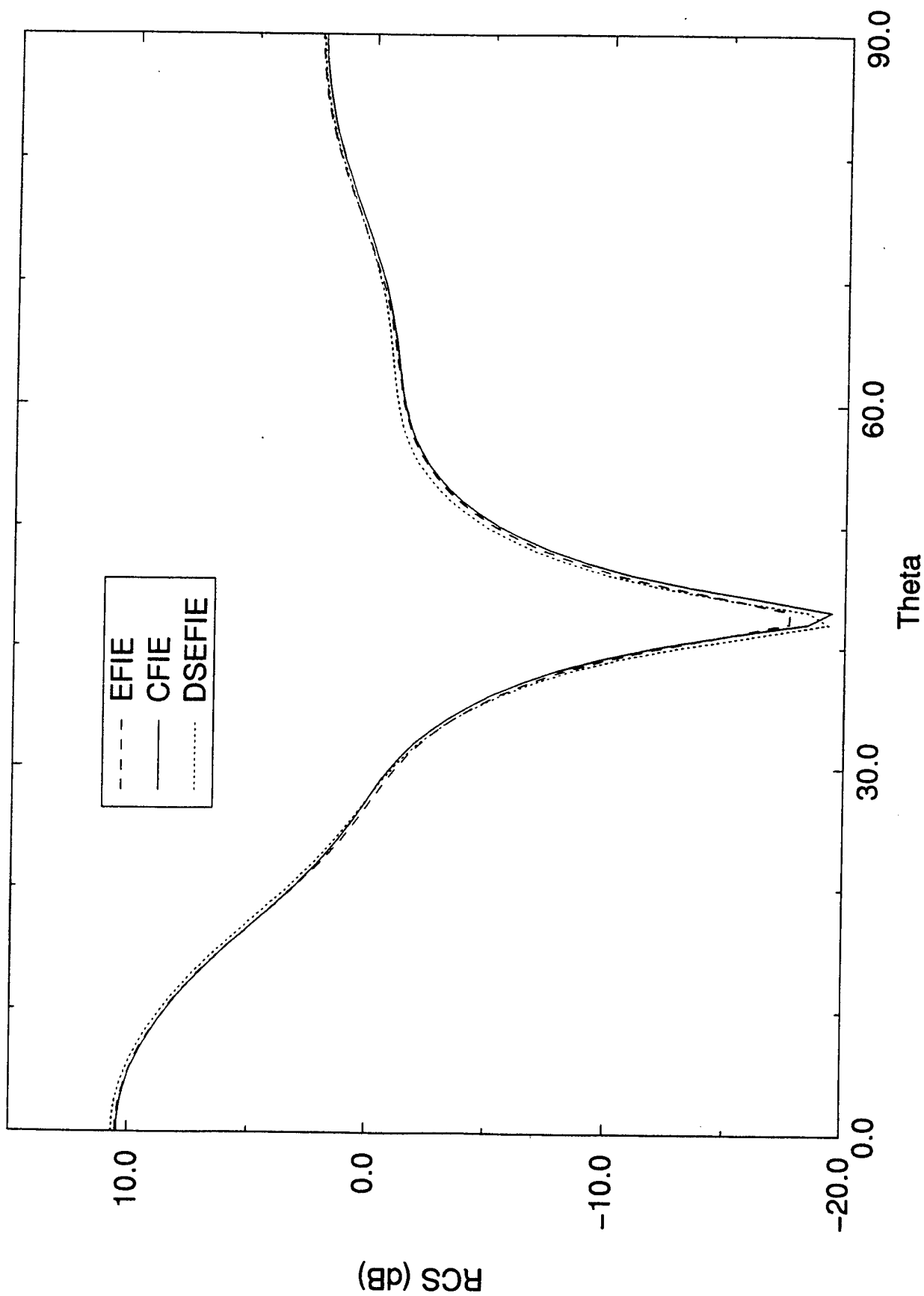
Figure 13. Monostatic E-plane RCS patterns for the non-resonant finite cylinder $R = d = .52$.
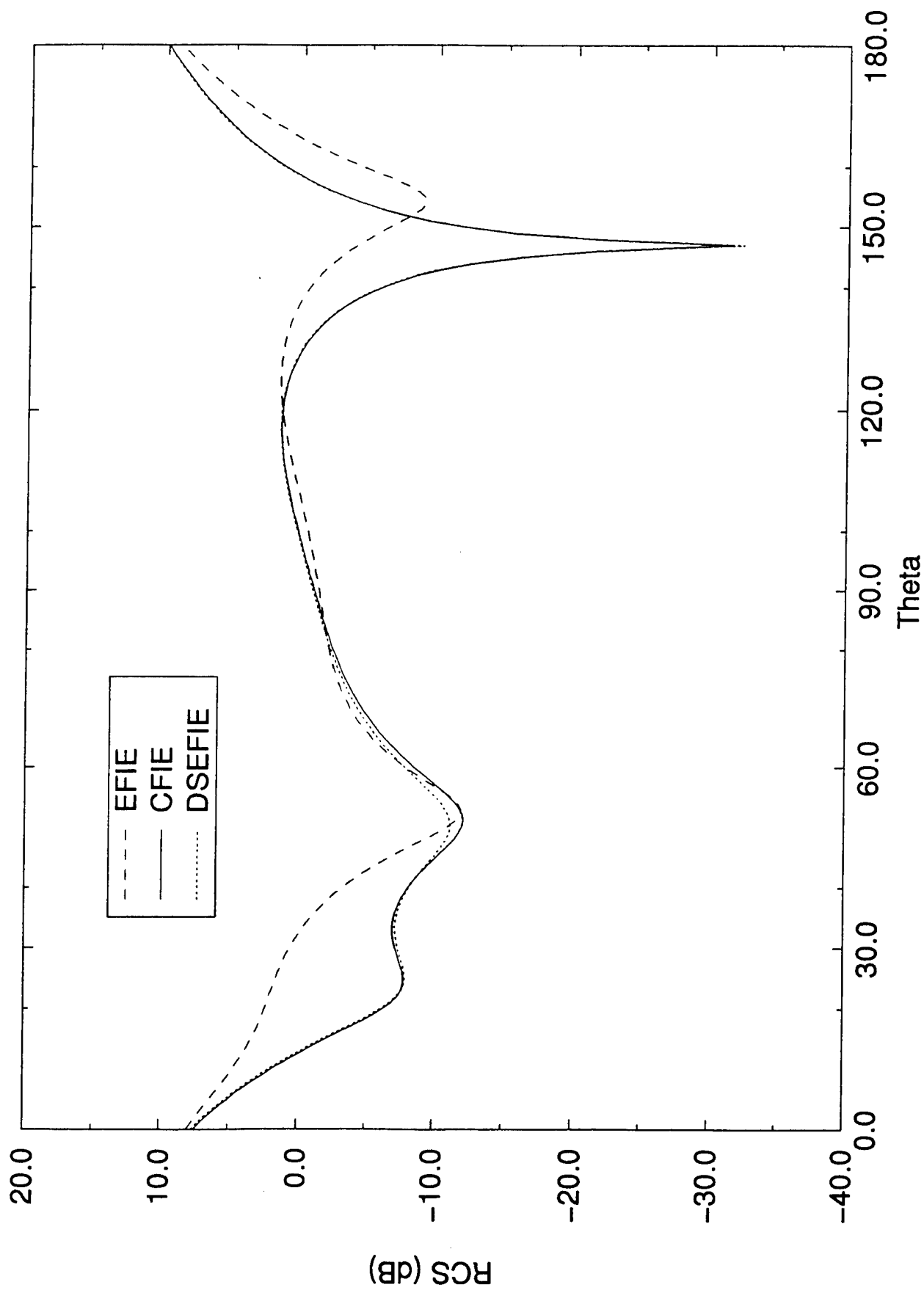
Figure 14. Bistatic scattering in the E-plane for oblique incidence at 30° on the resonant finite cylinder $R = d = .587$. The spurious resonance in the EFIE pattern is removed by the DSEFIE and CFIE.

CFIE, and DSEFIE curves for bistatic scattering in the E-plane for oblique incidence at 30° on the resonant finite cylinder, $R = d = .587$. As in Fig. 12, the spurious resonance behavior of the EFIE curve is removed by both the CFIE and DSEFIE.

3.4 Bistatic Scattering From the Cone-Sphere with Axial Illumination

The cone-sphere is the BOR whose generating curve is shown in Fig. 15. It is determined by two parameters: 1) the semi-vertex angle ζ of the cone, and 2) the radius a of the spherical cap. The length b of the straight-line segment of the generating curve is given by $b = a/\tan\zeta$ and the length of the circular portion of the generating curve is $a(\pi/2 + \zeta)$. Also shown in Fig. 15 is the generating curve for the cone-sphere dual surface separated by δ from the original surface.

The use of the DSEFIE to calculate scattering from the cone-sphere introduces a problem, not encountered in calculating scattering from the sphere or spheroid, that will be discussed here. In Fig. 16 we have plotted bistatic scattering in the E-plane from a cone-sphere with $\zeta = 5°$ and $ka = 5.9$ for axial incidence in the $-z$ direction, as calculated by the CFIE and DSEFIE. The separation δ of the dual surface from the original surface is $\delta = \lambda/4$. It is seen that there are small oscillations in the central portion of the DSEFIE curve that are not present in the combined-field integral equation pattern obtained using the computer code CICERO. To investigate the source of these oscillations, in Fig. 17 we have plotted the CFIE RCS pattern of Fig. 16 along with the two "components" of the DSEFIE pattern: the EFIE pattern obtained with the original cone-sphere surface alone, and the DSEFIE pattern

61
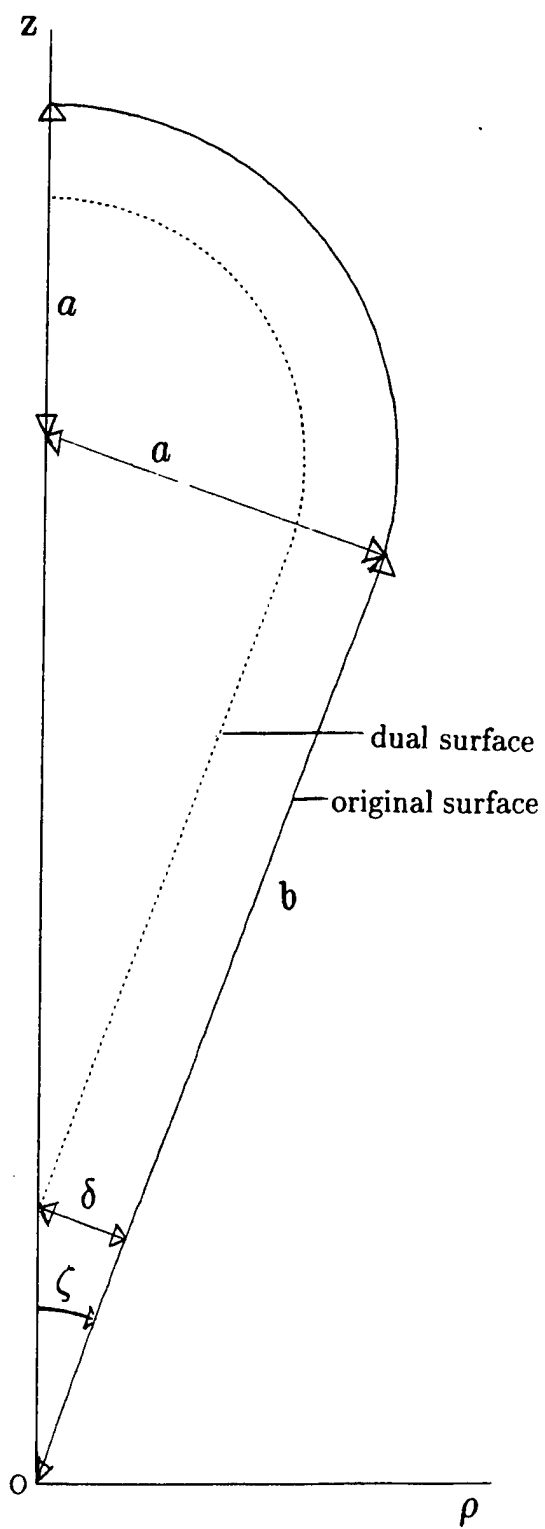
Figure 15. Generating curves for the cone-sphere and the dual surface.

Figure 16. E-plane bistatic RCS patterns for axial incidence in the $-z$ direction on the cone-sphere, $\zeta = 5°$, $ka = 5.9$; $\delta = \lambda/4$ for the DSEFIE curve. Note the small oscillations in the central portion of the DSEFIE curve.
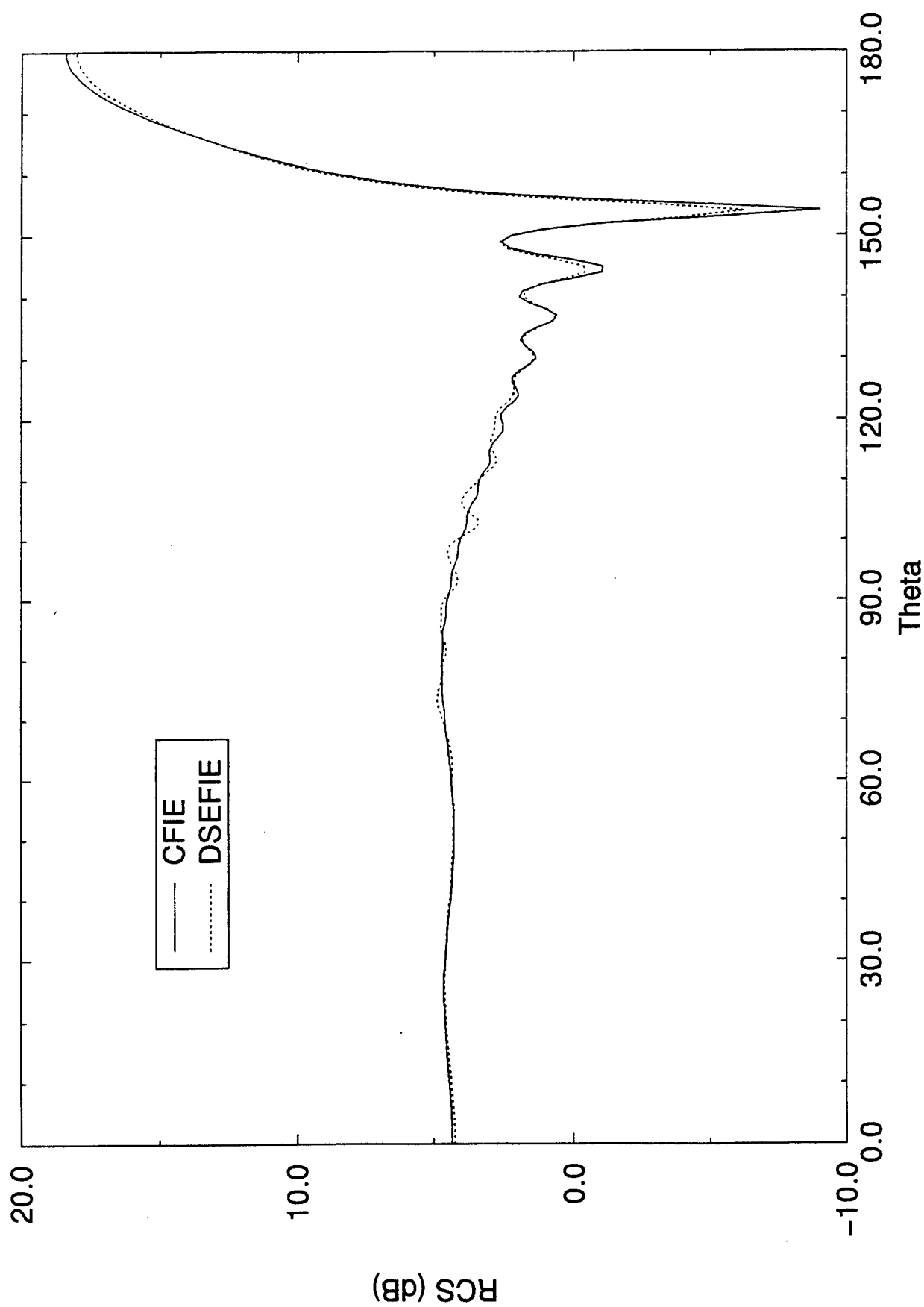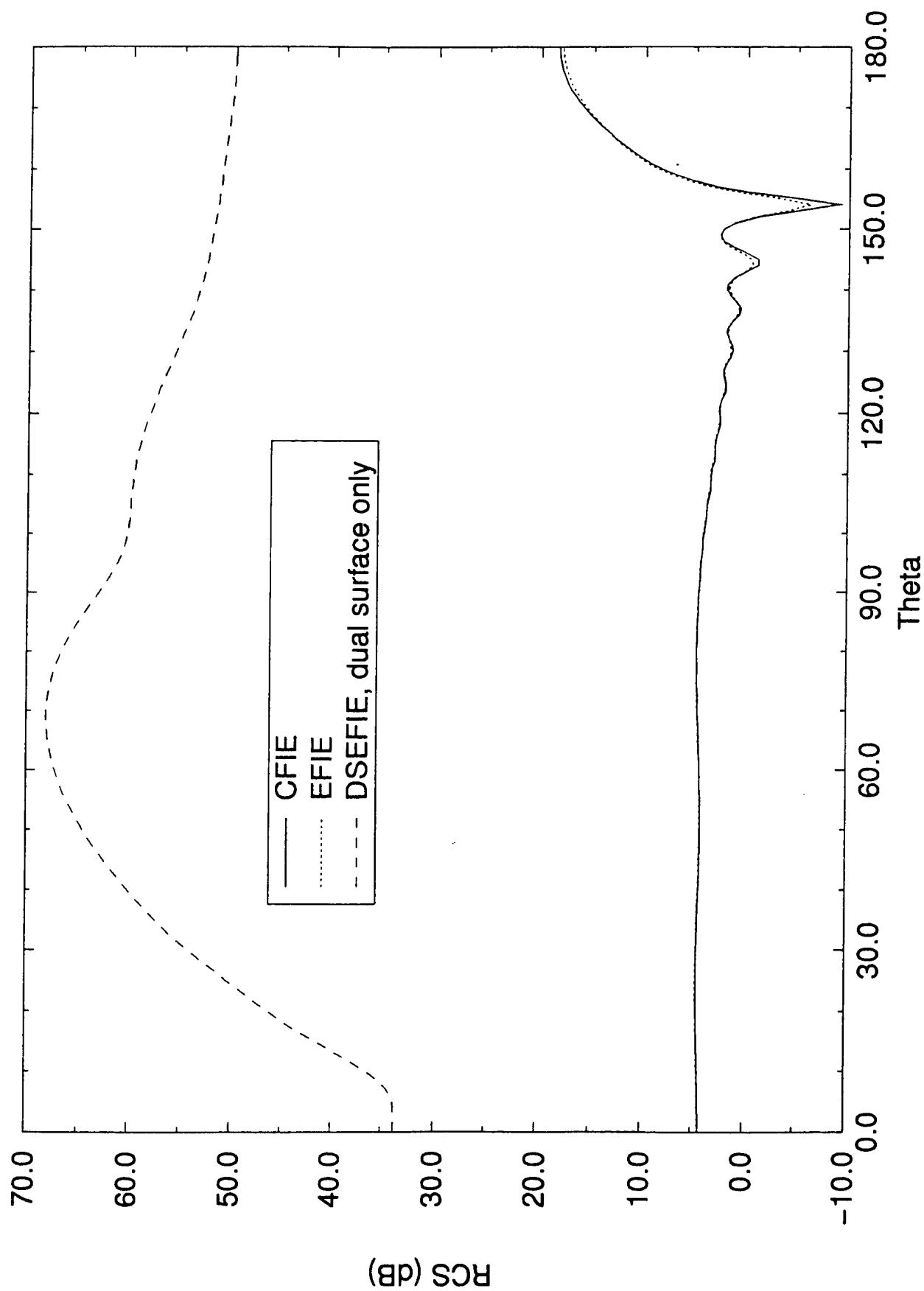
63

Figure 17. E-plane bistatic RCS patterns for axial incidence in the $-z$ direction on the cone-sphere, $\zeta = 5°$, $ka = 5.9$. The CFIE pattern of Fig. 16 is plotted with the two "components" of the DSEFIE pattern of Fig. 16.

obtained with the dual surface alone.[7] It is seen that while the RCS curve obtained with the EFIE and the original cone-sphere surface is very close to that obtained with the CFIE, the RCS curve obtained using the DSEFIE with the boundary condition enforced on the dual surface alone differs greatly from the other two curves. With the dual-surface-only pattern so much in error, the DSEFIE cannot be expected to give accurate results, since the DSEFIE calculations will be very sensitive to the value of the combination parameter, α. For further understanding, the currents on the cone-sphere surface were printed out and it was found that when the zero-tangential electric field boundary condition was enforced on the dual surface alone, the currents close to the vertex of the cone were several orders of magnitude larger than the currents close to the vertex when the zero-tangential electric field boundary condition was enforced on the original cone-sphere surface alone. The discrepancy between the DSEFIE and CFIE RCS patterns in Fig. 16 is therefore due to a problem in calculating scattering from the cone-sphere when a zero-tangential electric field is enforced on the dual surface alone.

A partial explanation for why this problem occurs appears to be the following. Unlike for the sphere or spheroid where corresponding points on the original and dual surfaces are a specified distance δ apart, for the cone-sphere points close to the vertex can be considerably further apart than δ from their corresponding points on the dual cone-sphere surface. For

---

[7]When we refer to the "components" of the DSEFIE pattern, we do not mean to imply that the total DSEFIE pattern is a linear combination of the EFIE solution and the DSEFIE solution obtained with the zero-tangential electric field boundary condition enforced on the dual surface alone. This is not the case. Loosely speaking, however, there is no harm in referring to these two limiting forms of the DSEFIE solution as "components", especially as considerable insight into the DSEFIE solution can be obtained by so doing.

example, the vertex point on the dual cone-sphere surface is a distance $\delta/\sin\zeta$ from the vertex of the original cone-sphere. For $\zeta = 5°$ and $\delta = \lambda/4$ this distance is almost 3λ. The boundary condition of zero-tangential electric field on the dual surface is then apparently insufficient to guarantee that the currents close to the tip of the cone-sphere will be correct. It should be noted, however, that this problem is specifically associated with the tip of the cone and is not simply a result of corresponding points on the original and dual surface varying in distance from one another. For the finite cylinder generating curves shown in Fig. 4, for example, the distance between the corresponding points on the corners of the original and dual surface generators is greater by a factor of $\sqrt{2}$ than the distance between the corresponding points on the midpoints of the horizontal or vertical line segments, but there is no problem in calculating the RCS pattern when the zero-tangential electric field boundary condition is enforced on the dual surface alone.

The problem we have described cannot be solved simply by placing the dual surface considerably closer than $\lambda/4$ to the original surface. Even a separation of $\lambda/64$ does not satisfactorily resolve the difficulty. What can be done, however, in addition to placing the dual surface closer to the original surface is to insert an auxiliary dual surface close to the vertex of the cone-sphere as shown in Fig. 18 in which the line segment that generates this auxiliary dual surface is obtained by drawing a line from the origin to, say, the midpoint of the line from the vertex of the dual cone-sphere normal to the original cone-sphere generator. The point on this generating line segment of the auxiliary dual surface that corresponds to the vertex of the original cone-sphere is taken a small distance, say $\lambda/64$, along this line. In Fig. 19 we show the bistatic RCS patterns for the same cone-sphere as in Fig. 16 obtained using the DSEFIE with an enhanced dual surface with $\delta = \lambda/32$ for the main dual surface.
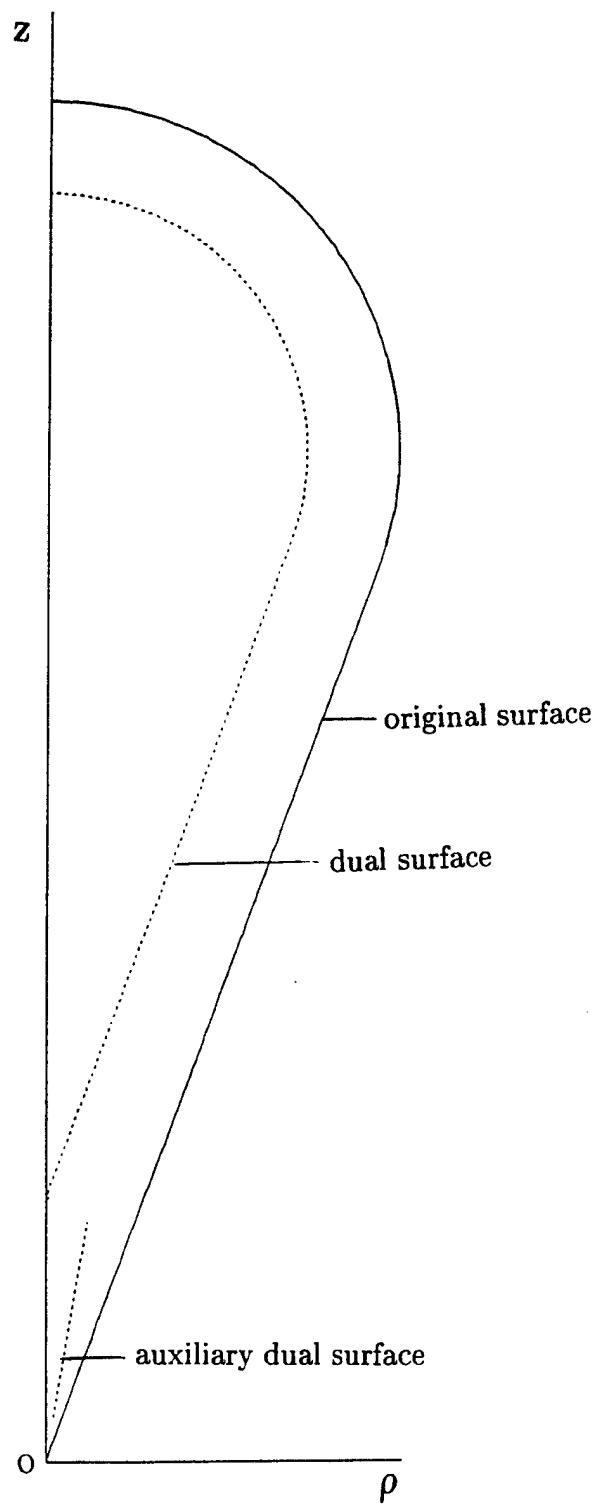
Figure 18. Generating curves for the cone-sphere and the dual surface with auxiliary dual surface inserted close to the tip.
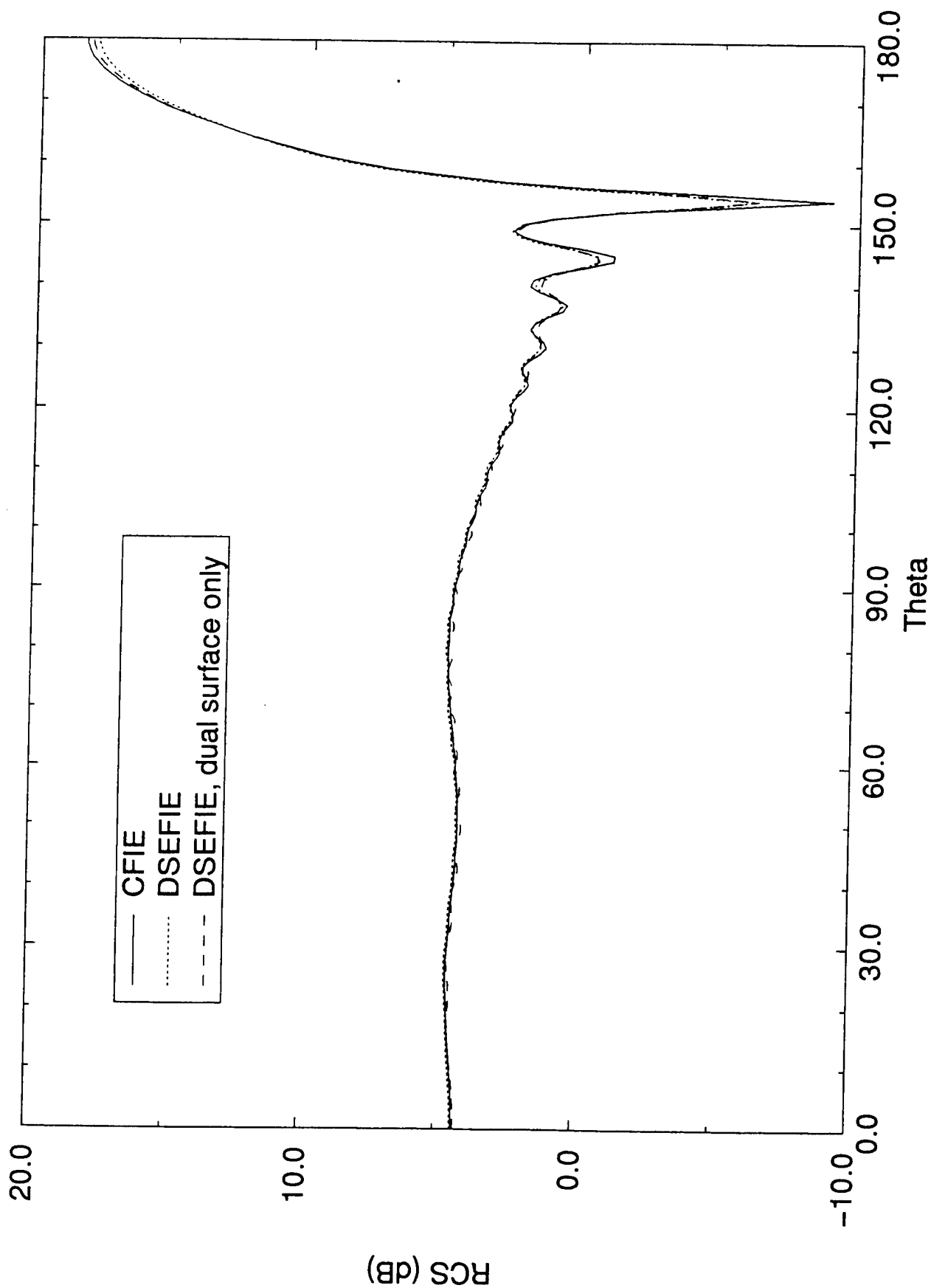
Figure 19. E-plane bistatic RCS patterns for axial incidence in the $-z$ direction on the cone-sphere, $\zeta = 5°$, $ka = 5.9$ with an enhanced dual surface employed and $\delta = \lambda/32$ for the main dual surface.

The small oscillations present in the DSEFIE pattern of Fig. 16 are completely removed.
Also shown in Fig. 19 is the pattern obtained with the DSEFIE when only the enhanced dual surface is employed. In striking contrast to the DSEFIE pattern of Fig. 17 the dual-surface-only pattern of Fig. 19 is now very close to the CFIE pattern. To demonstrate that the great improvement obtained with the enhanced dual surface is the result of both employing the auxiliary dual surface in the vicinity of the cone-sphere vertex and moving the main dual surface closer to the original surface, in Fig. 20 we have plotted two additional patterns along with the CFIE pattern. One pattern corresponds to employing the same auxiliary dual surface but with the main dual surface separated by $\lambda/4$ from the original surface, and the other pattern corresponds to simply moving the main dual surface close to the original cone-sphere surface by taking $\delta = \lambda/32$ but not employing the auxiliary dual surface. It is seen that employing the auxiliary dual surface while keeping the main dual surface separated by $\lambda/4$ from the original surface results in considerable improvement compared to the dual-surface-only pattern of Fig. 17 though not as much as that obtained when the main dual surface is moved closer and the auxiliary dual surface employed. Merely moving the main dual surface close to the original surface without employing the auxiliary dual surface still results in a very poor RCS pattern, however. For larger semi-vertex angles ζ the problem we have described in this section is less severe but is still present. For $\zeta = 45°$, for example, a separation of $\delta = \lambda/32$ suffices to resolve the problem without the necessity of inserting an auxiliary dual surface close to the cone tip.

69
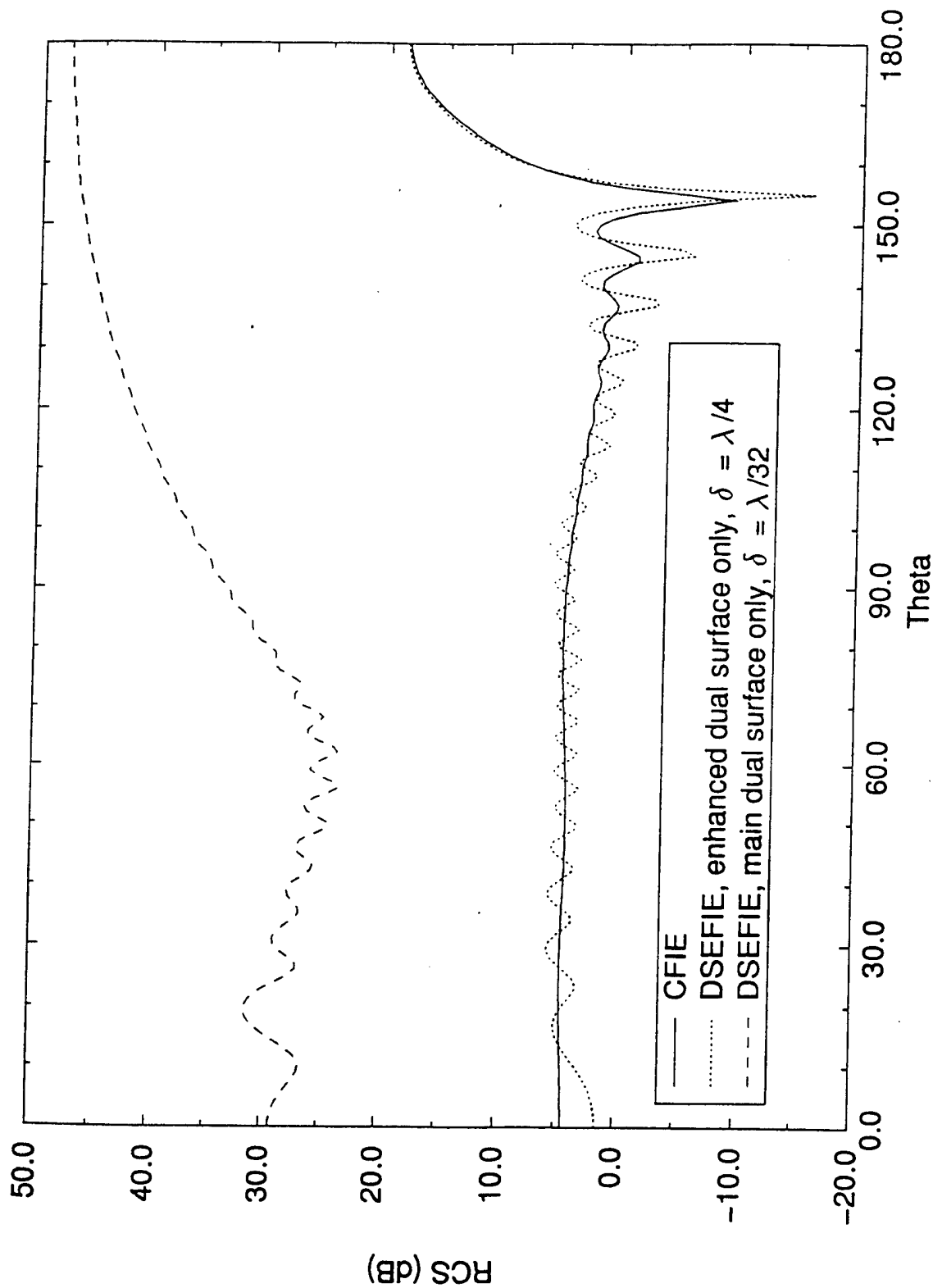
Figure 20. E-plane bistatic RCS patterns for axial incidence in the $-z$ direction on the cone-sphere, $\zeta = 5°$, $ka = 5.9$. The $\cdots\cdots$ DSEFIE pattern corresponds to using the same auxiliary dual surface as in Fig. 17 but with the main dual surface separated by $\lambda/4$ from the original cone-sphere surface. The ——— DSEFIE pattern is obtained with a separation of $\delta = \lambda/32$ between the original cone-sphere surface and the main dual surface, and with no auxiliary dual surface employed.

70

3.5 Cone-Sphere Monostatic Scattering

In this section we discuss scattering for oblique incidence on the cone-sphere in contrast to the previous section where axial incidence was considered. For axial incidence, only the first order Fourier mode is required to describe azimuthal variation. For oblique incidence, however, the zeroth order Fourier mode as well as higher order modes are required in addition to the first order mode. It will be seen that the presence of the zeroth order mode in particular introduces complications not encountered for axial incidence.

Figure 21 shows the monostatic pattern in the E-plane for the narrow tip-angle cone-sphere, $\zeta = 5°, ka = 5.9$, treated in Section 3.4 as calculated by the CFIE[8], EFIE, and DSEFIE, using Fourier modes 0 through 6. The DSEFIE calculation is performed with the enhanced dual surface described in Section 3.4, with a separation of $\delta = \lambda/32$ between the original cone-sphere surace and the main dual surface. Figure 22 shows the corresponding curves in the H-plane. It is seen that there is a significant difference between the values of the E-plane RCS's for θ in the vicinity of 15°, while the H-plane patterns exhibit only small differences in a low dB region of the patterns. In Fig. 23 we show the E-plane monostatic patterns when modes 1 through 6 are used, and observe that there is virtually no difference between the CFIE, EFIE, and DSEFIE patterns. In contrast, the CFIE, EFIE, and DSEFIE patterns for the zeroth order mode only, shown in Fig. 24, display significant differences in the vicinity of $\theta = 15°$. The results shown so far thus demonstrate that the differences in the E-plane monostatic patterns plotted in Fig. 21 are attributable to differences in the zeroth order mode patterns. Furthermore, since the E-plane and H-plane zeroth order mode pat-

---

[8]Unless otherwise noted, when we refer to the CFIE it is assumed that the combination parameter α_0 (see (3)) is set equal to 0.5, thereby giving equal weight to the EFIE and MFIE components of the CFIE.

Figure 21. E-plane monostatic RCS patterns for the cone-sphere, $\zeta = 5°$, $ka = 5.9$; Fourier modes 0 through 6. Enhanced dual surface used for the DSEFIE calculation with $\delta = \lambda/32$.

Figure 22. H-plane monostatic RCS patterns for the cone-sphere, $\zeta = 5°$, $ka = 5.9$; Fourier modes 0 through 6. Enhanced dual surface used for the DSEFIE calculation with $\delta = \lambda/32$.
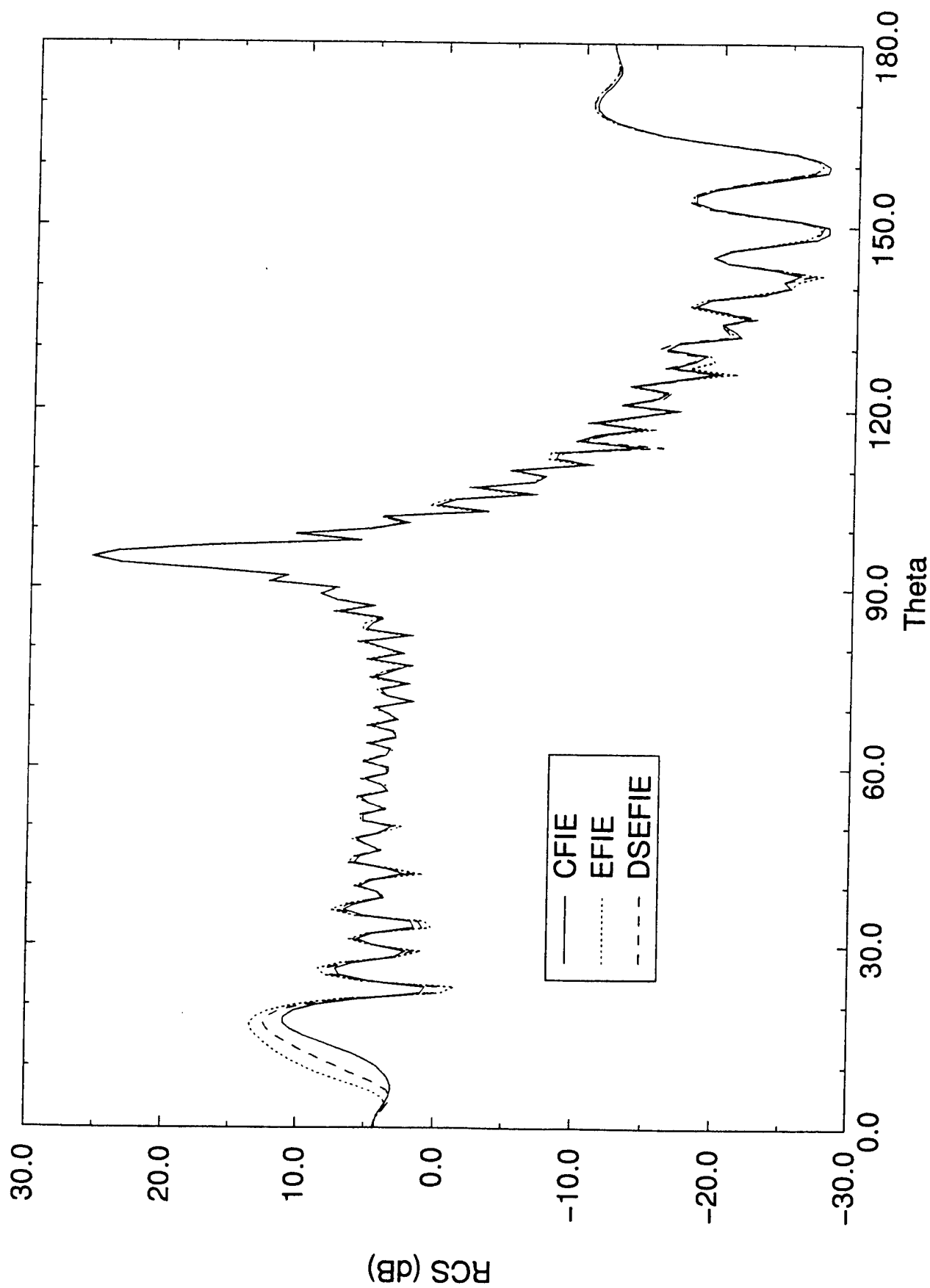
Figure 23. E-plane monostatic RCS patterns for the cone-sphere, $\zeta = 5°$, $ka = 5.9$; Fourier modes 1 through 6. Enhanced dual surface used for the DSEFIE calculation with $\delta = \lambda/32$.

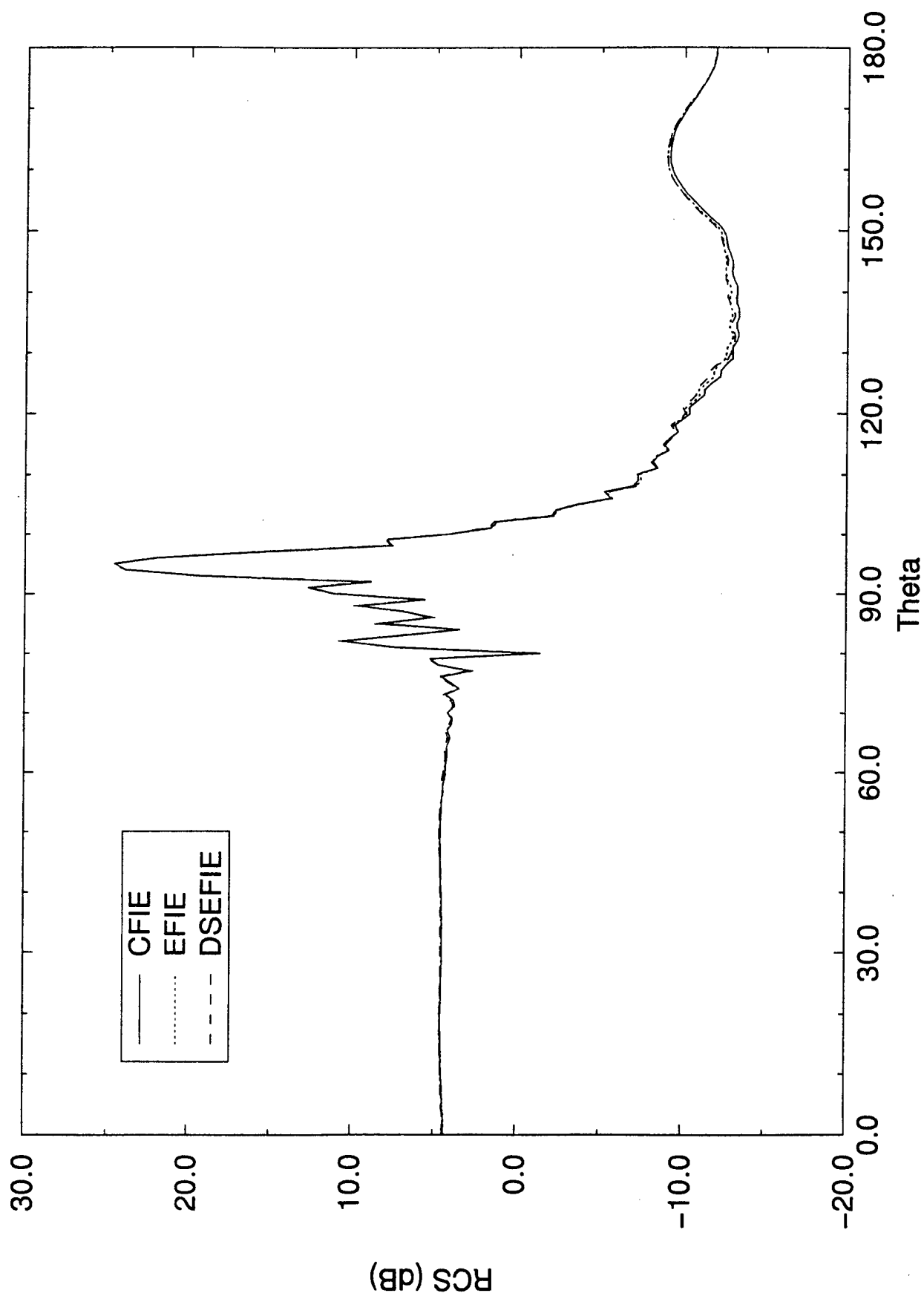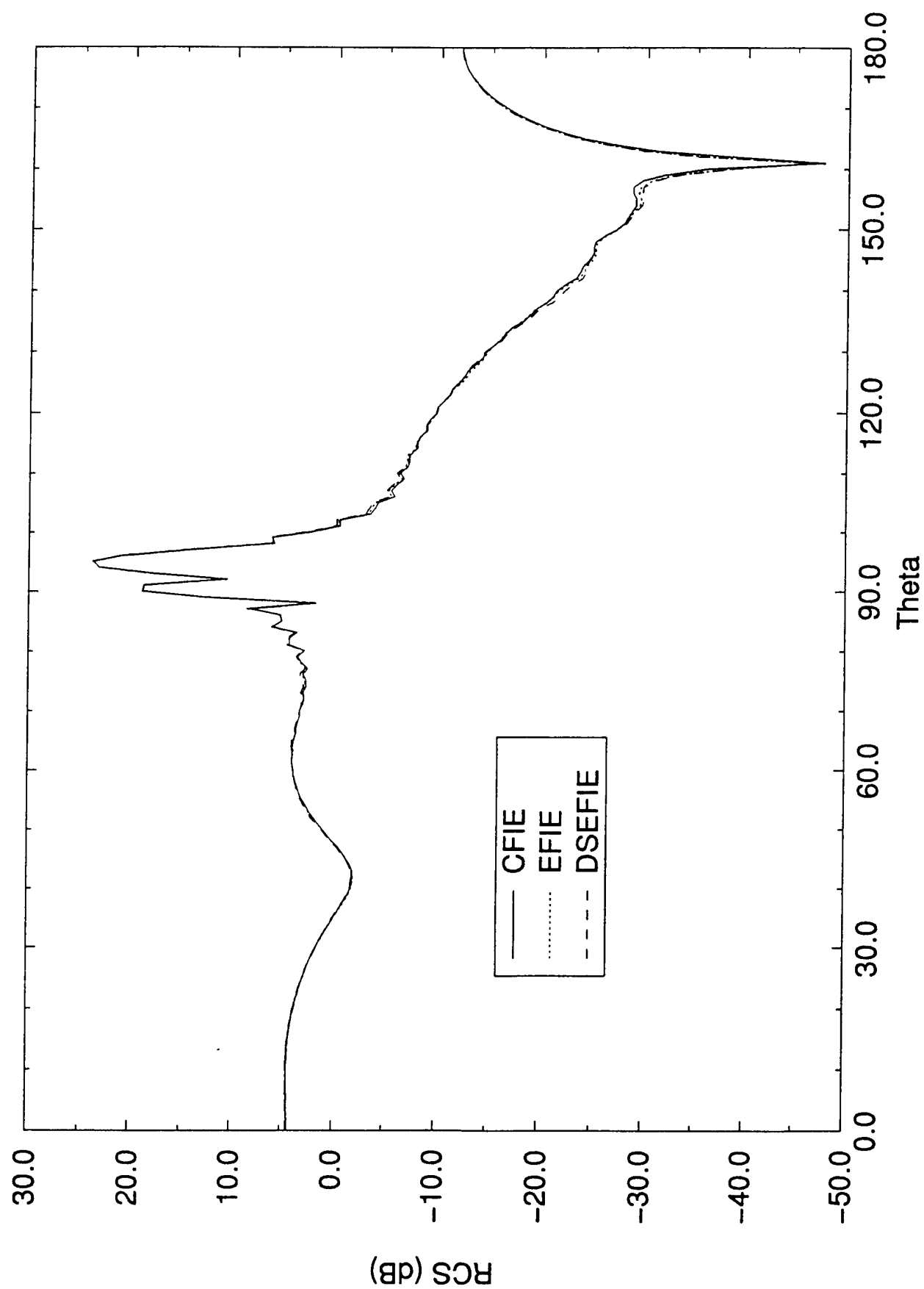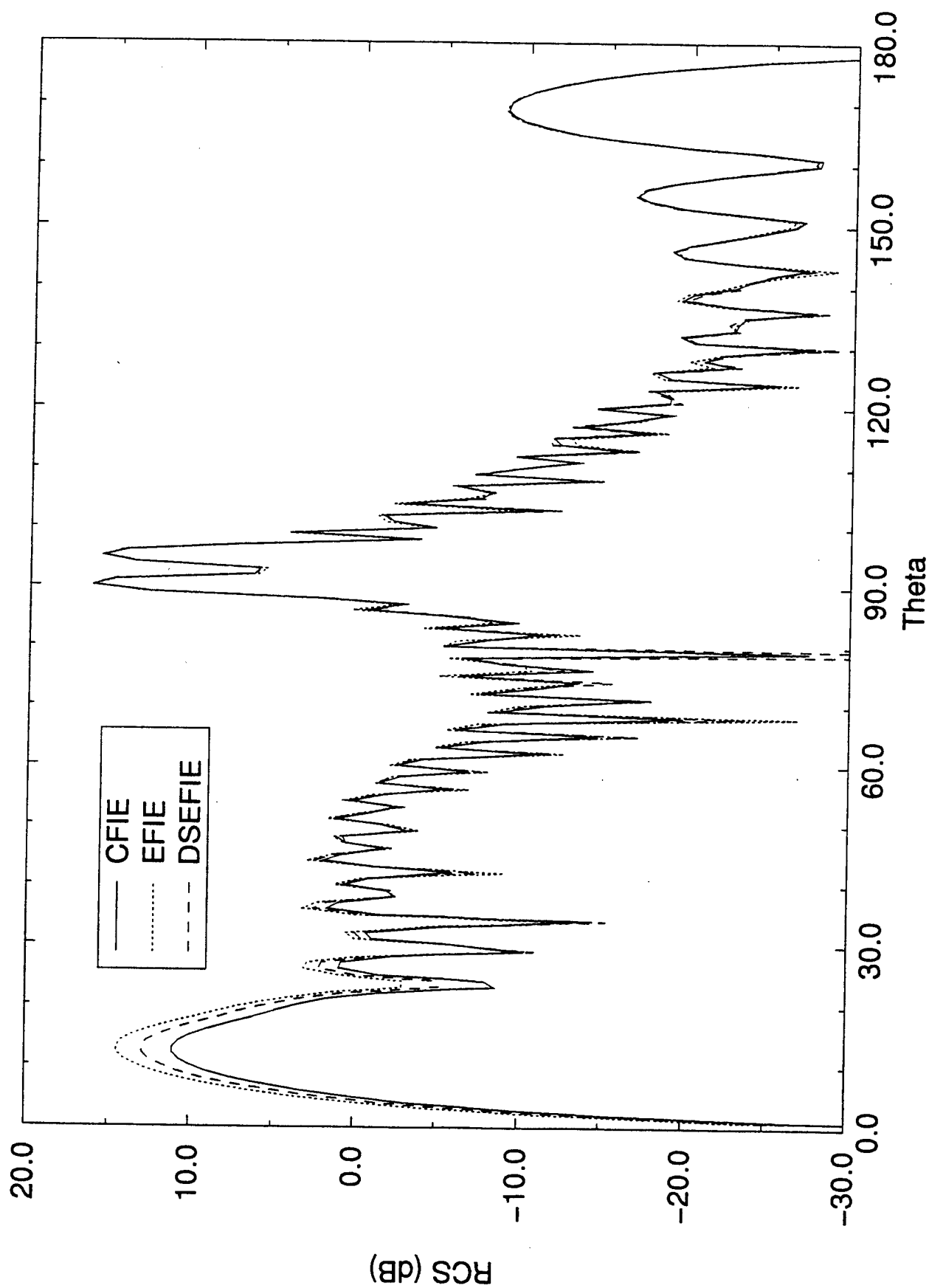Figure 24. E-plane monostatic RCS patterns for the cone-sphere, $\zeta = 5°$, $ka = 5.9$; Fourier mode 0 only. Enhanced dual surface used for the DSEFIE calculation with $\delta = \lambda/32$.

terms are due solely to the t-directed and ϕ-directed currents, respectively, it is the difference in accuracy with which the fields radiated by the zeroth order mode t-directed currents are calculated by the CFIE, EFIE, and DSEFIE, that accounts for the differences we have observed.

To establish which one of the CFIE, EFIE, and DSEFIE patterns of Fig. 24 can be regarded as correct, we begin by considering the discrepancy between the CFIE and EFIE patterns. Since it is known that the MFIE is ill suited to calculations involving scatterers with surfaces separated by much less than a wavelength, as is the case with narrow tip-angle cones, it can be conjectured that the discrepancy between the CFIE and EFIE patterns is due to the MFIE "component" that enters into the CFIE in combination with the EFIE, thereby degrading the accuracy of the EFIE solution.[9] In Fig. 25 we have plotted the EFIE and MFIE zeroth order mode E-plane monostatic patterns. We observe that the MFIE is considerably at variance with the EFIE not only in the vicinity of $\theta = 15°$ but for almost the entire range of θ from $0°$ to $90°$. To verify that it is indeed the MFIE pattern that is incorrect, in Fig. 26 we have plotted the EFIE pattern of Fig. 23 along with the MFIE pattern as recalculated with a density of 400 points/λ for the first wavelength from the tip of the cone where the t-currents vary most rapidly, and a density of 40 points/λ elsewhere. The MFIE pattern is now closer to the EFIE pattern, though it still displays a discrepancy of almost 2 dB in the near vicinity of $\theta = 15°$. Also shown in Fig. 26 is the EFIE pattern

---

[9]When we refer to the MFIE and EFIE "components" of the CFIE, we do not mean to imply that the CFIE solution is a linear combination of the MFIE and EFIE solutions. There is no harm, however, in thinking of these two limiting forms of the the CFIE solution as "components" since considerable insight into the CFIE solution can be obtained by so doing.

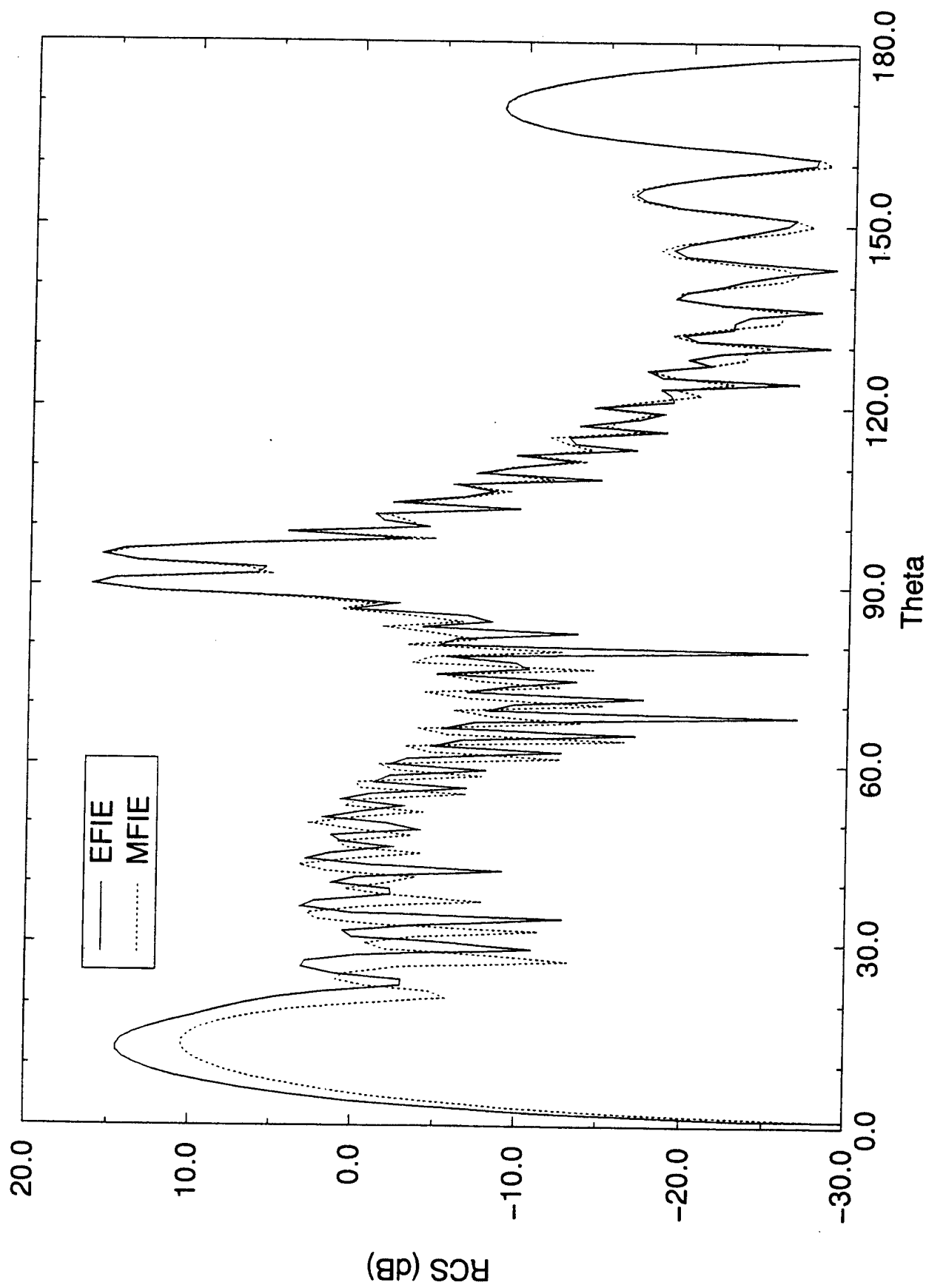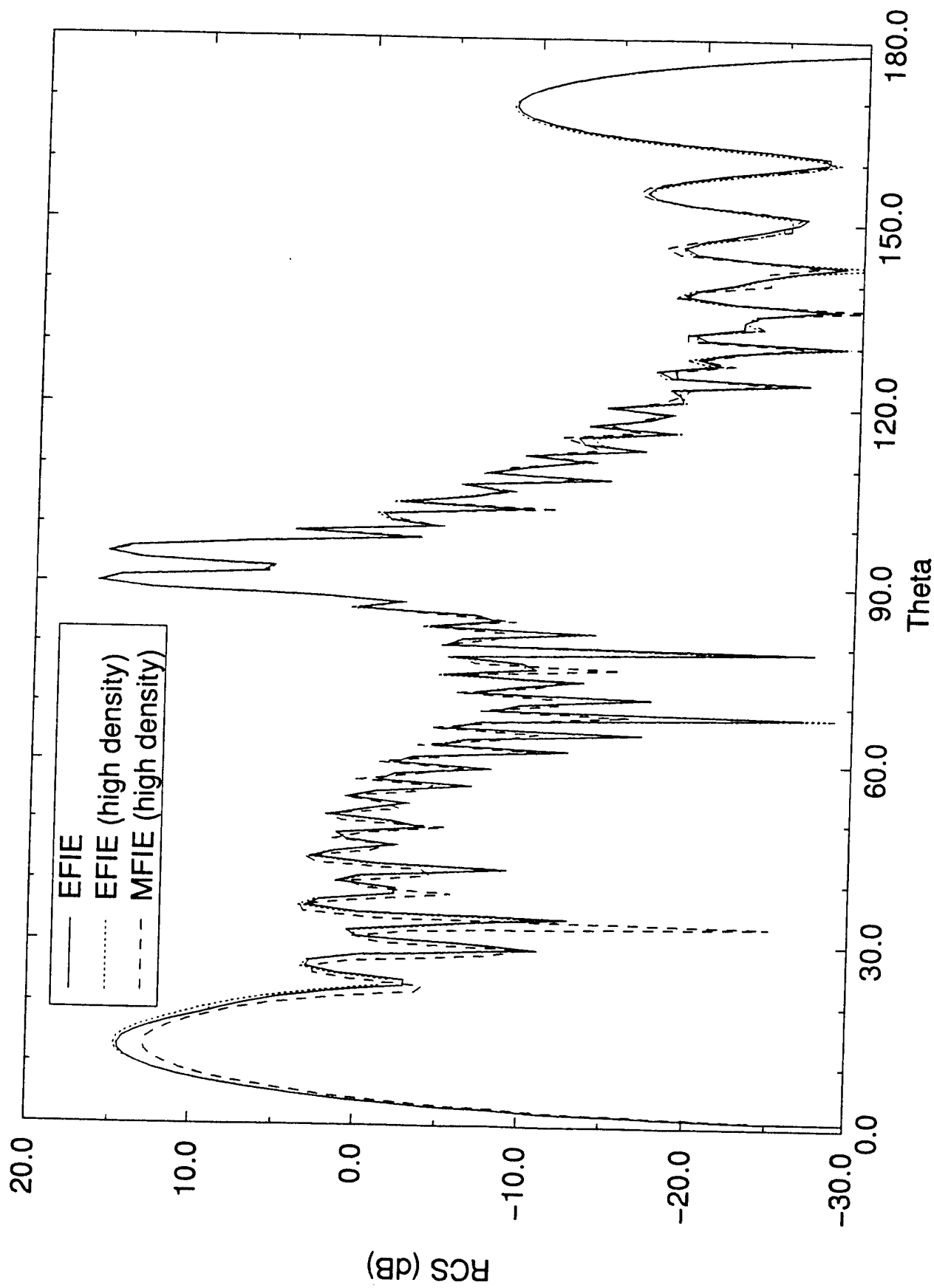Figure 25. E-plane monostatic EFIE and MFIE RCS patterns for the cone-sphere, $\zeta = 5°$, $ka = 5.9$; Fourier mode 0 only.

Figure 26. E-plane monostatic EFIE and MFIE RCS patterns for the cone-sphere, $\zeta = 5°$, $ka = 5.9$; Fourier mode 0 only. High-density patterns are obtained using a 400 point/λ grid in the t direction for a wavelength from the cone-tip and a density of 40 points/λ elsewhere.

78

as calculated with a 400 point/λ density close to the tip. It is seen that there is almost no change in the EFIE pattern. We therefore feel justified in regarding the EFIE pattern as correct.

Now the CFIE was developed to remove spurious resonances resulting from non-uniqueness of the MFIE and EFIE at internal cavity resonant frequencies. For non-resonant scatterers, such as the particular cone-sphere we are concerned with, the CFIE gives correct results provided that the MFIE and EFIE solutions, separately, are correct. Here, however, as we have seen, the MFIE solution of Fig. 25 that enters into the CFIE solution shown in Fig. 24 is highly inaccurate. Combining an inaccurate MFIE solution with an accurate EFIE solution can only degrade the accuracy of the EFIE solution, as witness the discrepancy between the CFIE and EFIE patterns of Fig. 24. If the CFIE pattern is recalculated using a density of 400 points/λ close to the cone tip, then the CFIE pattern is much closer to the EFIE pattern, as shown in Fig. 27. This is as expected since, as we have seen, the accuracy of the MFIE component of the CFIE is thereby considerably increased. The problem we have encountered here with the CFIE corroborates the finding of Wood and Hill [23] that the value of the combination parameter used in the CFIE can strongly influence the rate of convergence of the solution as the density of points/λ is increased. An accurate EFIE ($\alpha_0 = 1.0$) solution can be obtained here with a 40 points/λ density, but a value of $\alpha_0 = 0.5$ (equal weighting of the EFIE and MFIE) requires a density of approximately 400 points/λ to yield acceptable results.

Having established the accuracy of the EFIE zeroth order mode E-plane monostatic pattern, how is the discrepancy shown in Fig. 24 between the DSEFIE and EFIE solutions to be explained? As with the CFIE, employing a density of 400 points/λ for the first wave-
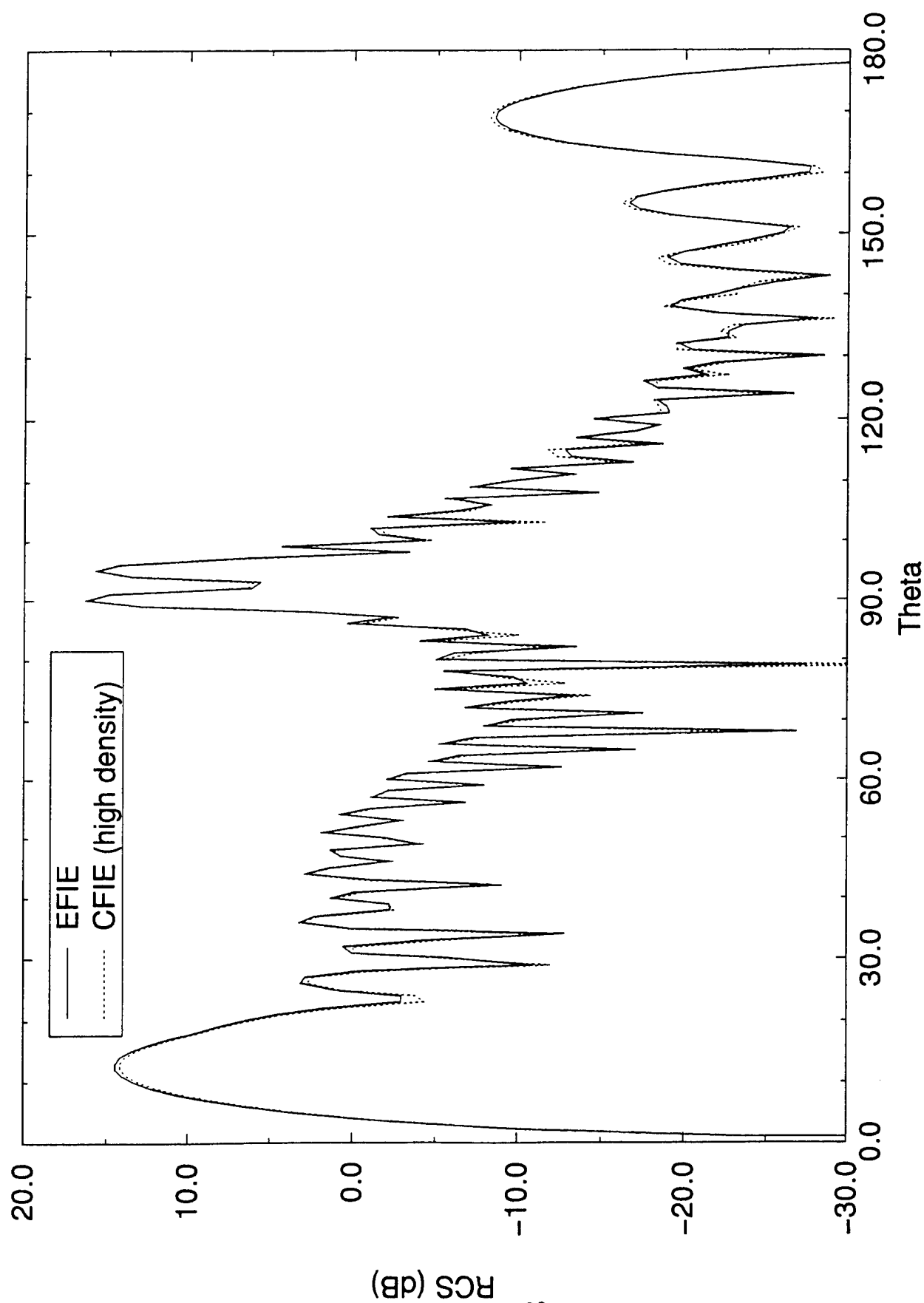
79

Figure 27. E-plane monostatic EFIE and CFIE RCS patterns for the cone-sphere, $\zeta = 5°$, $ka = 5.9$; Fourier mode 0 only. The CFIE pattern is obtained using a 400 point/λ grid in the t direction for a wavelength from the cone-tip and a density of 40 points/λ elsewhere.

80

length from the cone vertex and a density of 40 points/λ elsewhere gives a DSEFIE pattern very close to the EFIE pattern as shown in Fig. 28. It is difficult to be sure without extensive further investigation why this high density of points close to the cone tip is needed to obtain a highly accurate solution with the DSEFIE. Since the EFIE by itself gives an acceptable pattern for a density of 40 points/λ, it is clearly the calculation of the dual surface component of the DSEFIE that requires a high density of points. Furthermore, since a density of 80 points/λ gave acceptable DSEFIE results for the axial incidence bistatic scattering discussed in Section 3.4, it appears that the rapid variation of the zeroth order mode t-directed currents in combination with some aspect of the dual surface integration procedure, possibly the treatment of the self-term, is responsible for the difficulty with the dual surface calculation. The essential thing to stress, however, as we did in connection with the CFIE, is the importance of numerical experimentation before accepting the validity of surface integral scattering calculations, especially if high accuracy is desired.

Since, as stated in the Introduction, the rationale for developing the DSEFIE has been the importance of having two independent BOR surface integral equation scattering formulations and computer codes, and since, as we have also noted in the Introduction, a DSMFIE formulation already exists, it is of interest to see how well the DSMFIE calculates the zeroth order mode monostatic E-plane pattern for the narrow tip-angle cone considered here. In Fig. 29 we show the DSMFIE pattern calculated with a density of 400 points/λ close to the cone tip and 40 points/λ elsewhere, along with the EFIE pattern of Fig. 24, and the DSEFIE pattern of Fig. 28. A separation of $\delta = \lambda/4$ between the dual surface and the original cone-sphere surface is used for the DSMFIE calculation (the auxiliary dual surface used for the DSEFIE cone-sphere calculations is not useful for the DSMFIE calculations).

81

Figure 28. E-plane monostatic EFIE and DSEFIE RCS patterns for the cone-sphere, $\zeta = 5°$, $ka = 5.9$; Fourier mode 0 only. The DSEFIE pattern is obtained using a 400 point/λ grid in the t direction for a wavelength from the cone-tip and a density of 40 points/λ elsewhere.
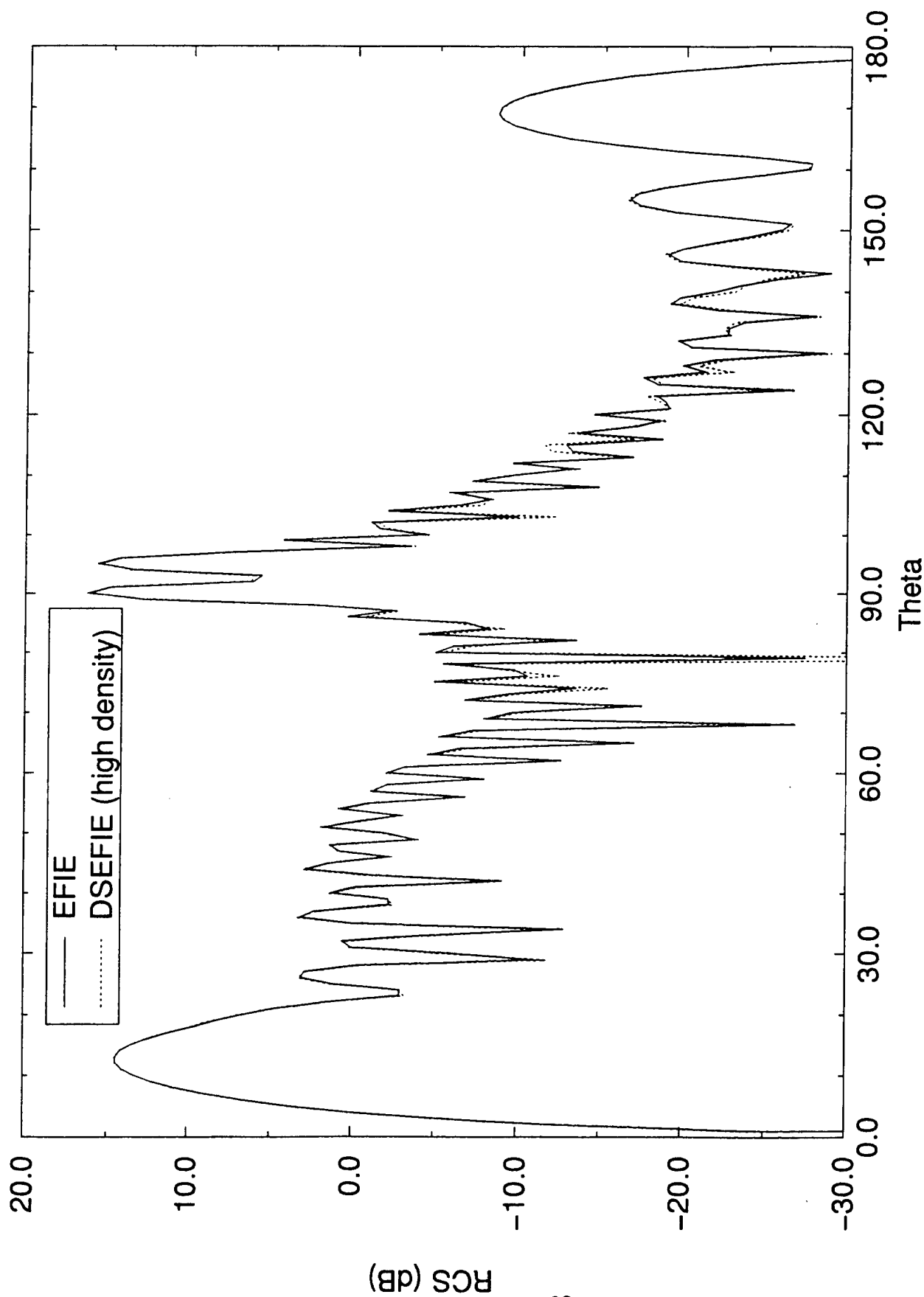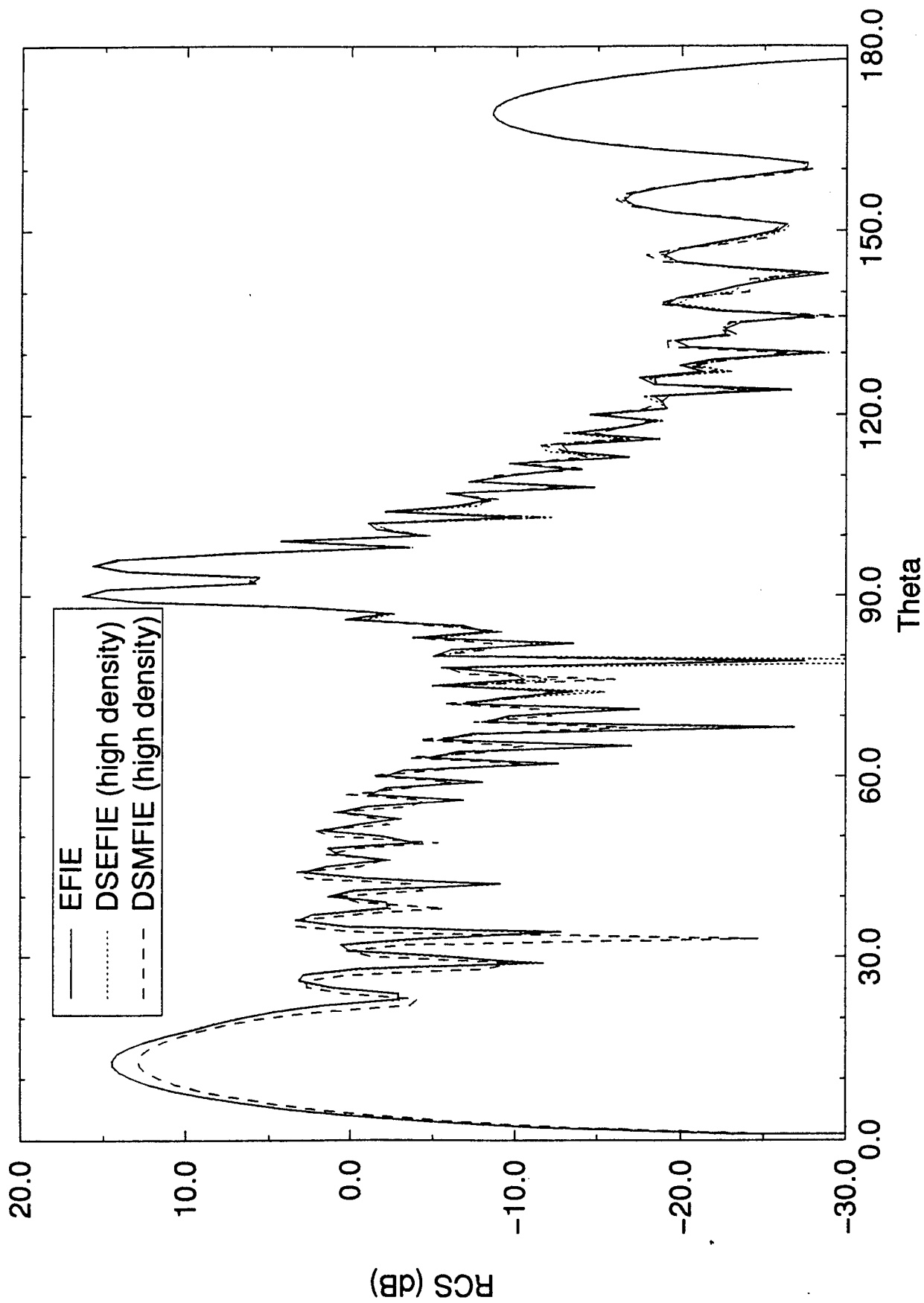
Figure 29. E-plane monstatic EFIE, DSMFIE, and DSEFIE RCS patterns for the cone-sphere, $\zeta = 5°$, $ka = 5.9$. The DSEFIE pattern is significantly more accurate than the DSMFIE solution.

83

The DSMFIE pattern is in error by 1.6 dB at $\theta = 13°$ and there are additional discrepancies in the location of peaks and nulls. We conclude that for calculations involving scatterers with narrow tips, the DSEFIE is significantly more reliable than the DSMFIE (see, however, Footnote 3).

3.6 Half-Triangle Functions

In Section 2.8 the expansion and testing functions were defined in terms of triangle functions $\tau_i(t)$ shown in Fig. 6. The $\tau_i(t)$ overlap as shown in Fig. 7 so that, for example, $\tau_{i-1}(t) = 1$ at t_{2i-1}^* where $\tau_i(t) = 0$, and $\tau_{i-1}(t) = 1$ at t_{2i+1}^* where $\tau_i(t) = 0$, etc. At the lower and upper poles of the discretized generating curve there is no overlap, however, since the first triangle function is $\tau_1(t)$ which is 0 at the lower pole, and the last triangle function is $\tau_{(P-3)/2}(t)$ which is 0 at the upper pole. In certain applications it may be desirable to have overlapping at the lower and upper poles of the generating curve. This can be achieved by employing the upper half of the triangle function $\tau_0(t)$ at the lower pole where, from (92),

$$\tau_0(t) = \begin{cases} 0, & t < 0, t \geq t_3^* \\ \dfrac{t_3^* - t}{d_1 + d_2}, & 0 = t_1^* \leq t \leq t_3^* \end{cases} \tag{136}$$

and adding the lower half of the triangle function $\tau_{(P-3)/2+1}(t)$ at the upper pole where

$$\tau_{(P-3)/2+1}(t) = \begin{cases} 0, & t \leq t_{P-2}, t > t_P^* \\ \dfrac{t - t_{P-2}^*}{d_{P-2} + d_{P-1}}, & t_{P-1}^* \leq t \leq t_P^* \end{cases} \tag{137}$$

If half-triangle functions are employed at the beginning and end of the generating curve, however, it is important to define the expansion and testing functions $f_i(t)$ by (121) rather than by (93) if $\rho \to 0$ at the lower or upper pole of the BOR generating curve. If, for example,

84

(93) is used to define $f_0(t)$ in conjunction with (136) and $\rho \to 0$ as $t \to 0$, $f_0(t)$ becomes singular at $\rho = 0$. Even if the actual value of $t = 0$ is not used because of the four-impulse approximation (96), calculations based on (93) and employing half-triangle functions can yield erroneous results.

As an example of the problems that can result by employing half-triangle functions along with the expansion and testing functions of (93), in Fig. 30 we show the E-plane RCS pattern of a sphere with $ka = 5.5$ obliquely illuminated by a TM plane wave at an angle of incidence of 45°. Along with the Mie series pattern shown for reference we show the DSEFIE patterns obtained with the basis functions of (93) with and without half-triangle functions, and the pattern obtained with the basis functions of (121) using half-triangle functions. It is seen that the pattern obtained using half-triangle functions and the basis functions of (93) differs greatly from the other three patterns. This discrepancy does not occur with the H-plane. Further calculations demonstrate that the discrepancy that occurs using half-triangle functions along with the basis functions of (93) is due to the zeroth order Fourier mode as shown in Fig. 31. No discrepancy occurs with the higher-order Fourier modes. Although not an explanation it is noted that for the zeroth order mode the E-plane pattern is due solely to the t-directed currents and not to the ϕ-directed currents while the H-plane patten is due solely to the ϕ-directed currents on the sphere.

4 SUMMARY

The purpose of this report is to provide for the first time a detailed analysis and solution of the problem of determining scattering from a PEC BOR using the DSEFIE, and to show

Figure 30. E-plane bistatic RCS patterns for TM oblique incidence at 45° on the sphere, $ka = 5.5$, demonstrating the use of half-triangles with the standard and alternate choice of the $f_i(t)$, (93) and (121), respectively: Fourier modes 0 through 6 employed.
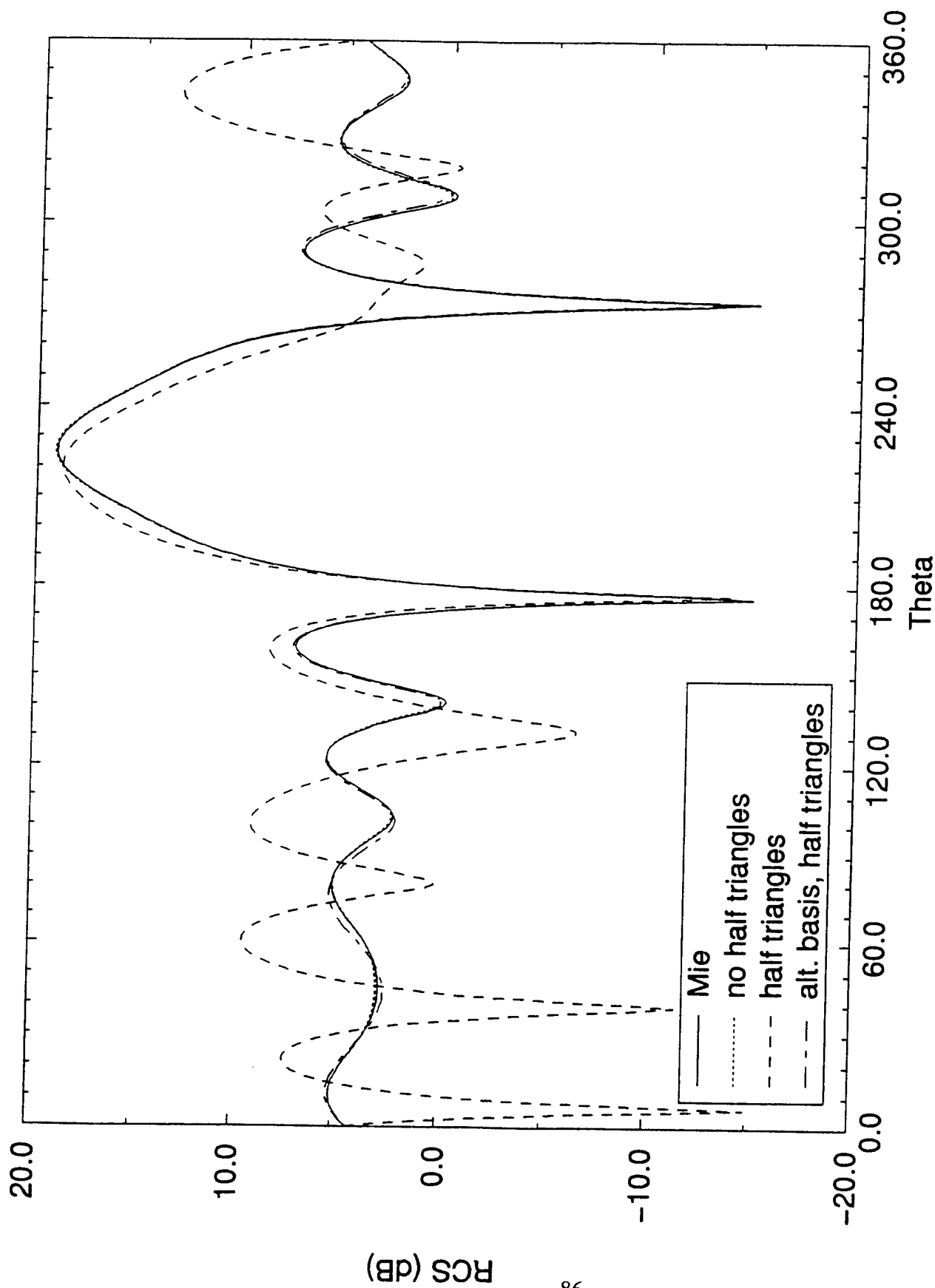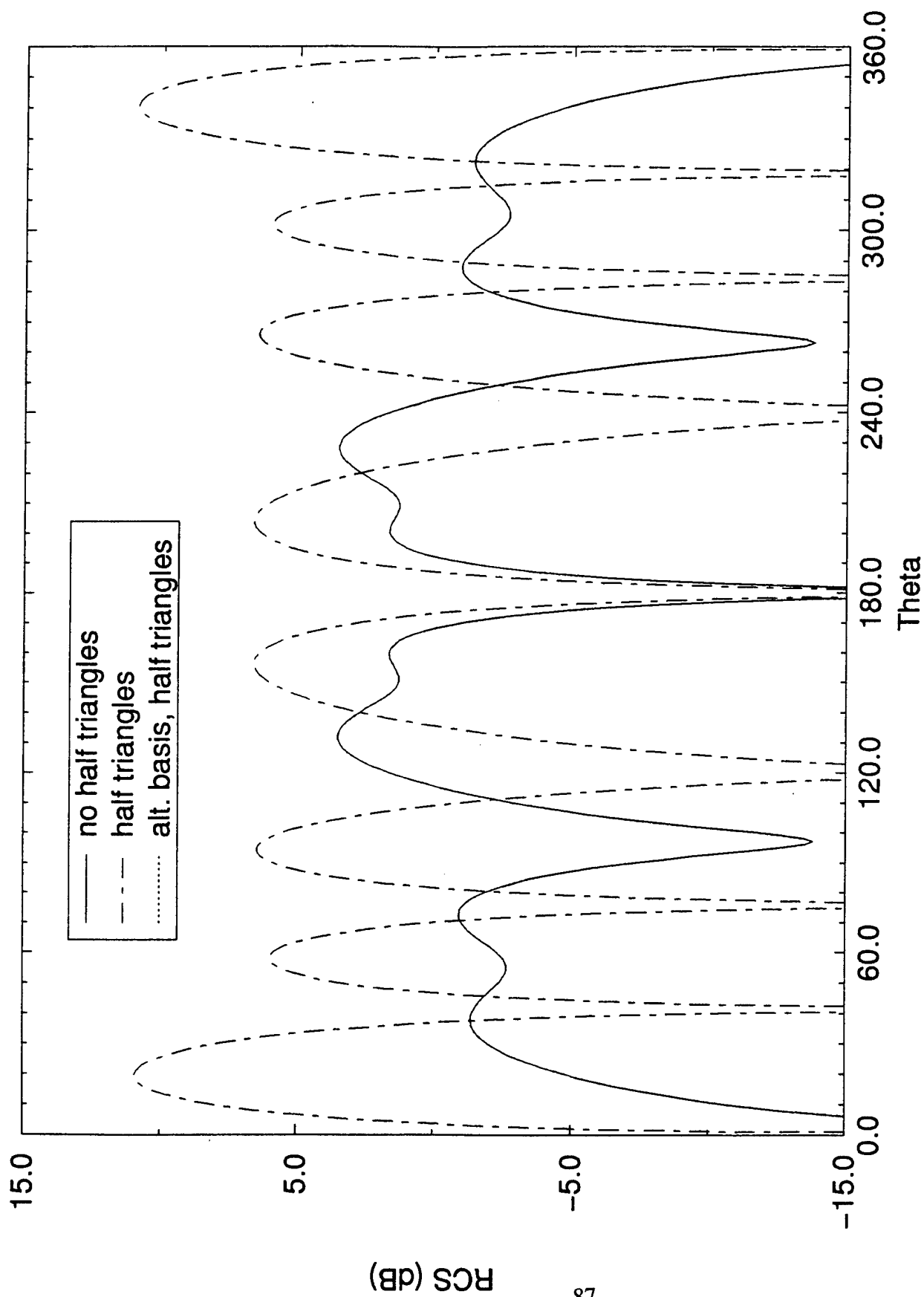
Figure 31. E-plane bistatic RCS patterns for TM oblique incidence at 45° on the sphere, $ka = 5.5$, demonstrating the use of half-triangles with the standard and alternate choice of the $f_i(t)$, (93) and (121), respectively; Fourier mode 0 only.

results obtained with a computer code based on this analysis. The DSEFIE is an extension of the EFIE in which the boundary condition that the tangential electric field vanish on the surface of a PEC object is satisfied not only on the actual surface but also on a fictitious surface lying inside the actual surface and separated by a small distance from it. Scattering solutions obtained using the DSEFIE are free from the spurious resonances that can seriously degrade the accuracy of solutions obtained using the conventional EFIE or MFIE for 3-D scatterers whose linear dimensions exceed a wavelength. These spurious resonances are a consequence of the fact that the EFIE and MFIE fail to produce a unique solution for the current on a PEC scatterer at frequencies equal to the resonant frequencies of the interior cavity formed by the surface of the scatterer. Although the widely used CFIE also eliminates spurious resonances, it is important to have available two independent surface integral formulations that can be applied and solved efficiently. Another surface integral equation solution free from spurious resonance that has been successfully programmed and tested, the DSMFIE, is also independent of the CFIE, but it does not yield accurate results for conductors containing narrow-angle wedges or tips.

In this report the DSEFIE is formulated in terms of the vector and scalar potentials, A and Φ, and then solved by the Galerkin form of the method of moments. It is noteworthy that the device of Mautz and Harrington used to transfer the differential operator on Φ to the testing functions and so maintain the singularity of the kernel equal to that of the free-space Green's function, cannot be used when the observation point lies on the dual surface rather than on the original surface. As a result the elements of the Z matrices for the DSEFIE have a more singular kernel than that of the free-space Green's function. This, however, does not appear to create numerical difficulties since the distance between points

on the original surface and points on the dual surface never goes to zero. The basis and testing functions are given as products of the Fourier modes used to express the azimuthal dependence of the currents, and triangle functions are used to express the dependence of the currents on the BOR generating curve parameter t. A four-impulse approximation to the triangle functions is used which enables the integrations with respect to t to be performed in closed form. Detailed expressions for the elements of the Z matrices and the V column vectors that appear in the Galerkin matrix formulation of the DSEFIE are then given as summations that can be readily evaluated by computer. The efficiency of evaluating these expressions can be greatly increased by using a change of indexing described in the report. Calculations performed with a computer program of the DSEFIE solution demonstrate the removal of spurious resonances that appear in calculations of the RCS's of spheres, spheroids, and finite cylinders made with the conventional EFIE. Cone-sphere calculations show that application of the DSEFIE to objects containing narrow tips requires careful placement of the dual surface in the vicinity of the tips and sometimes an increased density of grid points in the t direction a wavelength or so from the tip. When these precautions are taken, the DSEFIE yields significantly more accurate solutions than the DSMFIE for scatterers with narrow tips.

References

[1] J. Song, C. Lu, and W.C. Chew, "Multilevel fast multipole algorithm for electromagnetic scattering by large complex objects." *IEEE Trans. Antennas Propagat.*, vol. 45, pp. 1488–1493, October 1997.

[2] A.F Peterson, S.L. Ray, and R. Mittra, *Computational Methods for Electromagnetics*, New York: IEEE Press, 1998.

[3] B. Shanker, A.A. Ergin, K. Aygün, and E. Michielssen, "Analysis of transient electromagnetic scattering from closed surfaces using a combined field integral equation," *IEEE Trans. Antennas Propagat.*, vol.48, pp. 1064–1074, July 2000.

[4] F.H. Murray, "Conductors in an electromagnetic field," *Am. J. Math.*, vol. 53, pp. 275–288, 1931.

[5] A.W. Maue, "On the formulation of a general scattering problem by means of an integral equation," *Z. Phys.*, vol. 126, pp. 601–618, 1949.

[6] A.D. Yaghjian, "Augmented electric- and magnetic-field integral equations," *Radio Science*, vol. 16, 987–1001, November–December 1981.

[7] M.B. Woodworth and A.D. Yaghjian, "Multiwavelength three-dimensional scattering with dual-surface integral equations," *J. Opt. Soc. Am. A*, vol. 11, pp. 1399–1413, April 1994.

[8] L.M. Correia, "A comparison of integral equations with unique solution in the resonance region for scattering by conducting bodies," *IEEE Trans. Antennas Propagat.*, vol 41, pp. 52–58, 1993.

[9] A.J. Poggio and E.K. Miller, "Integral equation solutions of three-dimensional scattering problems," in *Computer Techniques for Electromagnetics*, R. Mittra, ed., New York: Pergamon, 1973, ch. 4.

[10] J.R. Mautz and R.F. Harrington, "H-field, E-field, and combined-field solutions for conducting bodies of revolution'" *Arch. Math. Ubertragungtech.*, vol. 32, pp. 157–164, 1978.

[11] J.R. Mautz and R.F. Harrington, *H-Field, E-Field, and Combined Field Solutions for Bodies of Revolution*, Rome Air Development Center Report No. RADC-TR-77-109, March 1977.

[12] J.M. Putnam, L.N. Medgyesi-Mitschang, and M.B. Gedera, "CARLOS three-dimensional method of moments code," *IEEE Trans Antennas Propagat. Mag.*, vol. 35, pp. 69–71, April 1993.

[13] A.D. Yaghjian and M.B. Woodworth, "Derivation, application and conjugate gradient solution of the dual-surface integral equations for three-dimensional, multiwavelength perfect conductors," in *PIER 5, Progress in Electromagnetics Research: Applications of the Conjugate Gradient Method to Electromagnetics and Signal Analysis*, T. Sarkar, ed., New York: Elsevier, 1991, 103–130.

[14] J.L. Schmitz, "Efficient solution for electromagnetic scattering using the dual surface magnetic-field integral equation for bodies of revolution," *Digest of the IEEE AP-S Int'l. Symp.*, Seattle, WA, pp. 2318–2321, June 1994.

[15] F.K. Oshiro, K.M. Mitzner, S.S. Locus, J.R. Coleman, and H.C. Heath, "Calculation of radar cross section," *Air Force Tech. Reps. AFAL-TR-69-52 and AFAL-TR-70-21*, Wright Patterson Air Force Base, Ohio, 1970.

[16] J. Van Bladel, *Electromagnetic Fields*, McGraw-Hill, New York, 1964.

[17] J.M. Song and W.C. Chew, "Multilevel fast-multipole algorithm for solving combined field integral equations of electromagnetic scattering," *Microwave and Optical Technology Letters*, vol. 10, pp. 14–19, September 1995.

[18] A.R. Tobin, A.D. Yaghjian, and M.M. Bell, "Surface integral equations for multi-wavelength, arbitrarily shaped, perfectly conducting bodies," *Digest of the National Radio Science Meeting (URSI)*, Boulder, CO, p. 9, January 1987.

[19] R.A. Shore and A.D. Yaghjian, "Shadow boundary incremental length diffraction coefficients applied to scattering from 3-D bodies," *IEEE Trans. Antennas and Propagat.*, vol. 49, January 2001.

[20] J.S. Schmitz, "Dual-surface magnetic- and electric-field integral equations for bodies of revolution in electromagnetic scattering," Ph.D. Thesis, University of Massachusetts Lowell, 1996.

[21] J.M. Putnam and L.N. Medgyesi-Mitschang, *Combined Field Integral Equation Formulation for Axially Inhomogeneous Bodies of Revolution*, McDonnell Douglas Research Laboratories MDC Report No. QA003, December 1987.

[22] A.C. Woo, H.T.G. Wang, M.J. Schuh, and M.L. Sanders, "Benchmark radar targets for the validation of computational electromagnetics programs," *Antennas and Propagation Magazine*, vol. 35, pp. 84–89, February 1993.

[23] W.D. Wood, Jr., K.C. Hill, et al., "Convergence properties of the CFIE for several conducting scatterers," 16th Annual Review of Progress in Applied Computational Electromagnetics, Naval Postgraduate School, Monterey, CA, March 2000, Conference Proceedings, pp.677-682.

[24] C.A. Balanis, *Advanced Engineering Electromagnetics*, New York: John Wiley, 1989.

[25] J.M. Putnam, personal communication, June 27, 2000.

[26] A.D. Yaghjian, *Near Field Antenna Measurements on a Cylindrical Surface: A Source Scattering Matrix Formulation*, NBS Technical Note 696, 1977.

[27] R.F. Harrington, *Time-Harmonic Electromagnetic Fields*, New York: McGraw-Hill, 1961.

[28] J.D. Jackson, *Classical Electrodynamics*, 3rd Edition, New York: John Wiley, 1999.